



ScuDo
Scuola di Dottorato - Doctoral School
WHAT YOU ARE, TAKES YOU FAR



Doctoral Dissertation
Doctoral Program in Physics (32.nd cycle)

Influence of disorder on the fundamental properties of Iron Based Superconductors

Daniele Torsello

* * * * *

Supervisor

Prof. Gianluca Ghigo

Doctoral Examination Committee:

Dr. S. Sanna, Referee, Università di Bologna

Dr. A. Sosso, Referee, Istituto Nazionale di Ricerca Metrologica

Prof. D. Daghero, Politecnico di Torino

Dr. G. Durin, Istituto Nazionale di Ricerca Metrologica

Prof. E. Silva, Università Roma Tre

Politecnico di Torino

March 2, 2020

This thesis is licensed under a Creative Commons License, Attribution - Noncommercial-NoDerivative Works 4.0 International: see www.creativecommons.org. The text may be reproduced for non-commercial purposes, provided that credit is given to the original author.

I hereby declare that, the contents and organisation of this dissertation constitute my own original work and does not compromise in any way the rights of third parties, including those relating to the security of personal data.

.....
Daniele Torsello
Turin, March 2, 2020

Summary

In this thesis I will report on the effects of disorder on the superconducting properties of Iron Based Superconductors (IBSs) and on their order parameter symmetry.

The research work involved measurement of critical temperature, London penetration depth, quasiparticle conductivity and surface impedance of IBS single crystals performed with a microwave resonator technique, that has been optimized for this task during this PhD project. Measurements were performed on samples of the Ni doped CaK-1144 family ($\text{CaKFe}_4\text{As}_4$ grown at Ames Laboratories) and of the Ba-122 family (BaFe_2As_2) with different kinds of doping (Co, K, and P grown at the the University of Tokyo and Rh at Ames Laboratories) covering all the possible typologies: electron doping, hole doping and isovalent substitution.

The same samples were characterized both in the pristine state and after successive doses of ion irradiation, in order to study the modification of their properties with increasing disorder. Ion irradiation was performed at the Laboratori Nazionali di Legnaro of the Istituto Nazionale di Fisica Nucleare (INFN): 3.5 MeV proton irradiation at the CN accelerator, 250-MeV Au ion irradiation at the Tandem accelerator and 1.2 GeV Pb ion irradiation at the Piave-Alpi accelerator. The details of the irradiation experiments are determined on the basis of Monte Carlo simulations performed with precompiled codes.

The measured critical temperature, London penetration depth and quasiparticle conductivity are then compared to theoretical predictions obtained solving the multiband Eliashberg equations in order to validate the pairing models and extract additional information. This comparison allows to investigate the behaviour of the superconducting gaps as a function of temperature and for increasing disorder.

With this approach it has been possible first to discuss the behavior of pristine single crystals of BaFe_2As_2 with different substitutional species (K, Co and P) covering hole

and electron doping and isovalent substitution. Then the effects of disorder introduced by 250 MeV Au ions in K doped BaFe_2As_2 samples were analyzed showing that T_c degradation and London penetration depth behavior due to the presence of disorder can be fully explained by the s_{\pm} order parameter symmetry promoted by antiferromagnetic spin fluctuations. Finally it has been possible to experimentally identify, in Rh-doped BaFe_2As_2 irradiated with high doses of 3.5 MeV protons, the transition from s_{\pm} to s_{++} order parameter symmetry (previously theoretically predicted) and propose additional signatures of the transition itself.

Moreover, the experimental investigation of the London penetration depth anisotropy in $\text{CaKFe}_4\text{As}_4$ and its dependence on Ni doping and pointlike disorder was carried out, as well as a comparison of how the morphology of irradiation induced defects impacts the critical temperature degradation with increasing disorder.

Acknowledgements

Firstly, I would like to sincerely thank my supervisor, Prof. Gianluca Ghigo, for his support and guidance both scientific and about my future career. My gratitude extends to the whole research group: Prof.s Francesco Laviano, Roberto Gerbaldo and especially Laura Gozzelino and Giovanni Ummarino for their help and advices during these three years, and to Andrea and Samuele for their company and encouragement.

I would like to acknowledge Prof. R. Prozorov and the group at Ames Laboratory for giving me the opportunity to work with them for one month and for showing me in details the experimental techniques they routinely employ.

My thanks go to Prof. T. Tamegai and his group at Tokyo University and to Prof. P Canfield and his group at Iowa State University for providing me with high quality samples of the most recently discovered materials without which this work would not have been possible.

I am sincerely grateful to the INFN-LNL staff, especially L. Maran, for their great technical help for the irradiation experiments.

Moreover I would like to thank all the participants to the HIBiSCUS project lead by Prof. M. Putti for the fruitful collaboration on the study of Fe(Se,Te) and the group of Dr. M. Truccato at the Università degli studi di Torino for the interesting work done on X-Rays damaging of oxide materials.

This work was partially supported by INFN projects TERA and ASIDI, and PRIN project HIBiSCUS.

Contents

1	Iron Based Superconductors	1
1.1	Context and motivation	1
1.2	Materials	3
1.3	Doping	5
1.4	Band structure	7
1.5	Pairing mechanism and order parameter symmetry	8
2	Experimental technique	11
2.1	Experimental setup	11
2.2	Cavity perturbation method	15
2.3	Calibration procedure	17
2.4	Measured quantities	19
2.4.1	Anisotropy of λ_L	23
2.4.2	Uncertainty analysis	25
3	Ion irradiation and disorder	31
3.1	Radiation damage	33
3.2	Particles accelerators	35
3.3	Monte Carlo simulations	37
3.4	Defects as scattering centers	39
4	Theoretical model	43
4.1	The Eliashberg approach	43
4.2	Eliashberg equations and input parameters	46
4.3	Calculated quantities	50
4.4	Fitting procedure	53

5	Results	57
5.1	Pristine samples	57
5.1.1	Ba-122 family	58
5.1.2	Anisotropy in CaK-1144	66
5.2	Extended defects	68
5.2.1	Comparison between irradiation typologies	69
5.2.2	250 MeV Au irradiation of $\text{Ba}_{1-x}\text{K}_x\text{Fe}_2\text{As}_2$	72
5.3	Pointlike defects	77
5.3.1	Anisotropy	77
5.3.2	Elevate disorder	78
6	Conclusions	89
A	Thin films	95
	Nomenclature	99
	Bibliography	101

Chapter 1

Iron Based Superconductors

1.1 Context and motivation

Superconductivity is a very appealing phenomenon that can be exploited for many applications: from dissipationless transport of electricity to the possibility of producing intense magnetic fields, therefore technology strongly drives the search for materials with optimal characteristics. This interesting phenomenon was at first discovered in metallic materials that were later called conventional superconductors: their critical temperatures (T_c) are in the range of few K and the fundamental mechanism with which electron can couple up (pairing mechanism) to form carriers that propagate without dissipation is well explained by BCS theory [1] with phonon mediated interaction. This model was successful for every material discovered since 1911 (Hg) to the late 1970s, when some intermetallic compounds containing rare earth atoms were found to show superconductivity combined with a high quasiparticle effective mass that was incompatible with the picture of electron-phonon coupling [2]. In 1986, the first high temperature superconductor, belonging to the cuprates class, was discovered [3]. The BCS theory could not explain the high T_c of these materials, that also present strong electronic correlations and spin fluctuations [4, 5]. In 2001 superconductivity was reported for MgB_2 , an intermetallic compound with T_c as high as 39 K [6]. The peculiarity of this material is the presence of two bands contributing to superconductivity [7, 8]. The most recently discovered category of superconductors is that of the so called iron-based superconductors (IBSs) [9, 10]. Although their critical temperatures are much lower than those of the cuprates, their smaller anisotropy and high critical fields have

attracted a lot of interest with respect to possible applications, in particular in the area of high-field magnets [11].

From a fundamental point of view, their discovery added a piece to the puzzle of unconventional superconductivity: these systems are characterized by multiple bands contributing to superconductivity [12, 13] (as MgB_2) and the pairing mechanism is non-phononic (as for the cuprates) [14]. In addition, the interplay between magnetism and superconductivity in these systems is particularly strong and intricate: the undoped, non superconductive, parent compounds are antiferromagnetic (AFM), spin fluctuations are believed to be the bosons responsible for electron pairing [15], and even the coexistence of ferromagnetism and superconductivity was observed in IBSs containing Eu [16].

Within this context, one of the main open questions regards the symmetry of the order parameter (*i.e.* the complex number representing the superconducting gap) that results from the combination of the multi-band nature of these materials and the coupling provided by spin fluctuations. The gap opens on different bands and, in principle, could have different characteristics on each one [17]. For example, conventional superconductors are characterized by an s-symmetric gap, whereas the cuprates are d-wave symmetric [4] and MgB_2 has two gaps, both s-wave symmetric [8]. In the case of the majority of IBSs, most indications point toward the presence of up to 5 gaps [18, 19] that are s-wave symmetric but with sign changing (*i.e.* a π phase shift) from band to band: the so called s_{\pm} symmetry [15, 20]. Unfortunately, it is very difficult to investigate the sign of the gaps experimentally, and therefore rule out the possibility of the similar, but sign preserving, s_{++} symmetry [21, 22].

A very effective approach in this regard focuses on the analyses of the effects of disorder on the superconducting properties that are expected to be affected in different ways depending on the symmetry of the order parameter of the material under study [23, 24]. This is the type of study addressed in this thesis: disorder is introduced in single crystals of IBSs by ion irradiation (see Chapter 3), the superconductive properties of the samples are investigated by means of a microwave coplanar waveguide resonator (CPWR) technique (described in Chapter 2) prior and after irradiation, and the experimental data are analyzed in the context of multi-band superconductivity by means of the Eliashberg-equations approach (explained in Chapter 4).

1.2 Materials

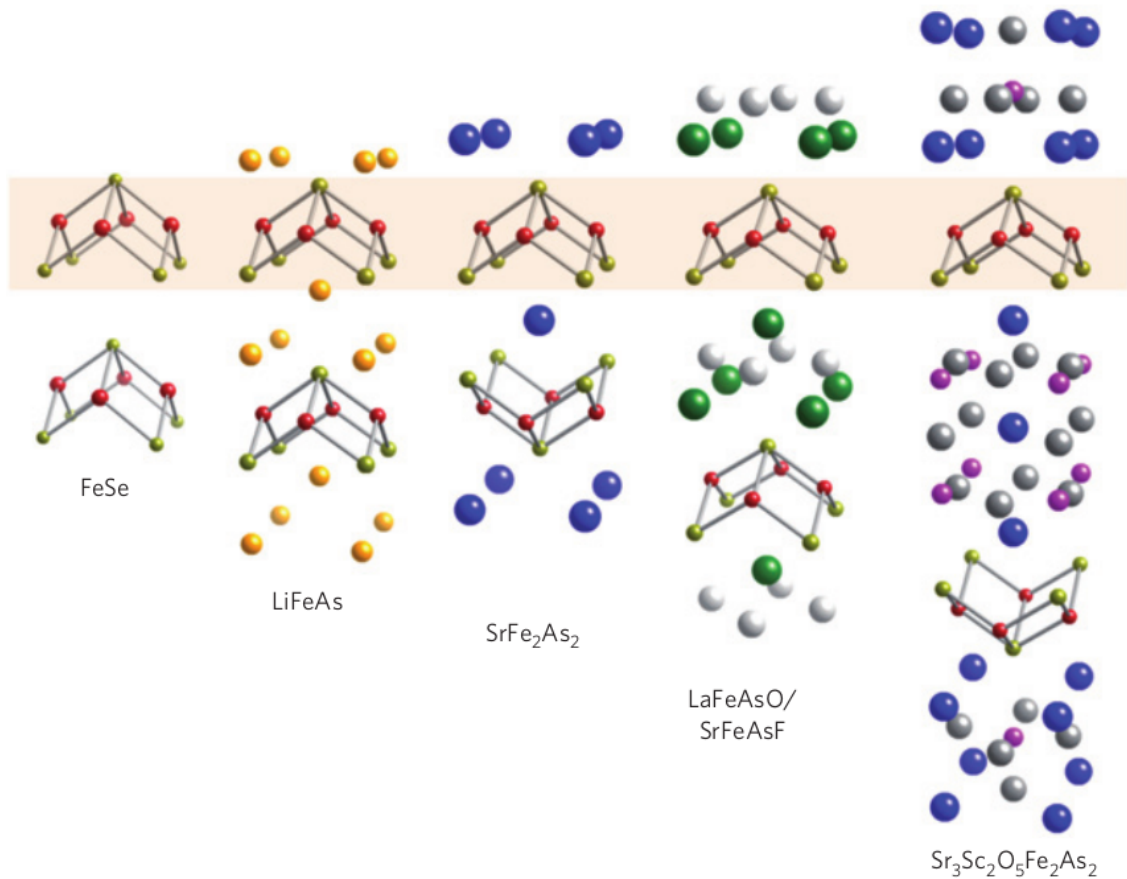


Figure 1.1: The crystallographic structure of IBSs showing some of the families with different blocking layers. From left to right are shown the 11, 111, 122, 1111 and 32522 families. The active FeX (red and yellow spheres) planes are marked. Adapted from [25]. ©2010, Springer Nature.

Iron based superconductors (IBSs) were discovered in 2006 by the group of Hosono: the first compound was LaFePO with a T_c of only 4 K [10], but a breakthrough happened only two years later with the discovery of LaFeAs(O,F) with a T_c of 26 K for the optimally doped compound [9]. Since then, a large variety of systems with different structures, but based on the same building blocks, were discovered. The fundamental unit of these materials are the superconducting Fe_2X_2 planes, where X is either a pnictide (As, P) or a chalcogenide (Se, S, Te) [26]. These layers are then divided by "spacer" or "blocking" layers that, in the end, allow to construct the overall structures and define

the different "families" of IBs [25, 27]. Examples of such families are the 11 (such as FeSe) in which there is no spacer layer, the 111 (e. g. LiFeAs) and 122 (BaFe_2As_2) where spacers are composed of single atomic species, and more complex structures, such as the 1111 (LaFeAsO), in which also the blocking layers are composed of combinations of different atoms. Some examples are given in Fig. 1.1.

For the work discussed in this thesis I have focused on the Barium containing Ba-122 and the Calcium/Potassium based CaK-1144 systems. Superconductivity in Ba-122 was discovered in 2008 [28] and the fact that good quality single crystals could be quite easily produced with intermetallic growth techniques brought them to be one of the most widely studied systems. Recently, the new 1144 family was discovered as a hybrid ordered phase between two systems of the 122 family (the Ca-122 and K-122), following the idea of considering these families also as building blocks for new ones [29]. The resulting structure is presented in Fig. 1.2: it is an alternate stack of two different 122 structures. The presence of alternate Ca and K blocking layers produces two inequivalent As sites and a breaking of the typical symmetry of the 122 family, resulting in peculiar properties of this system [30, 31].

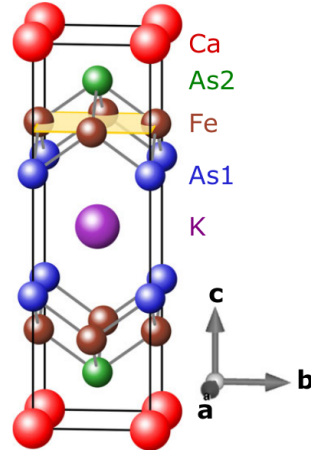


Figure 1.2: Crystallographic structure of CaK-1144 showing the inequivalent As sites. Adapted from [32]. ©2018, Springer Nature.

1.3 Doping

In most of these families, the parent compounds (such as BaFe_2As_2 or SrFe_2As_2 for the 122 system) are not superconducting, but superconductivity can be induced by chemical substitution or by applying pressure, giving rise to rich and complex phase diagrams. To better explain how this can be done, let me consider the Ba-122 family as an example. BaFe_2As_2 is an antiferromagnetic (AFM) metal down to low temperature, and superconductivity can be induced by substituting any of the atomic species in its composition [33].

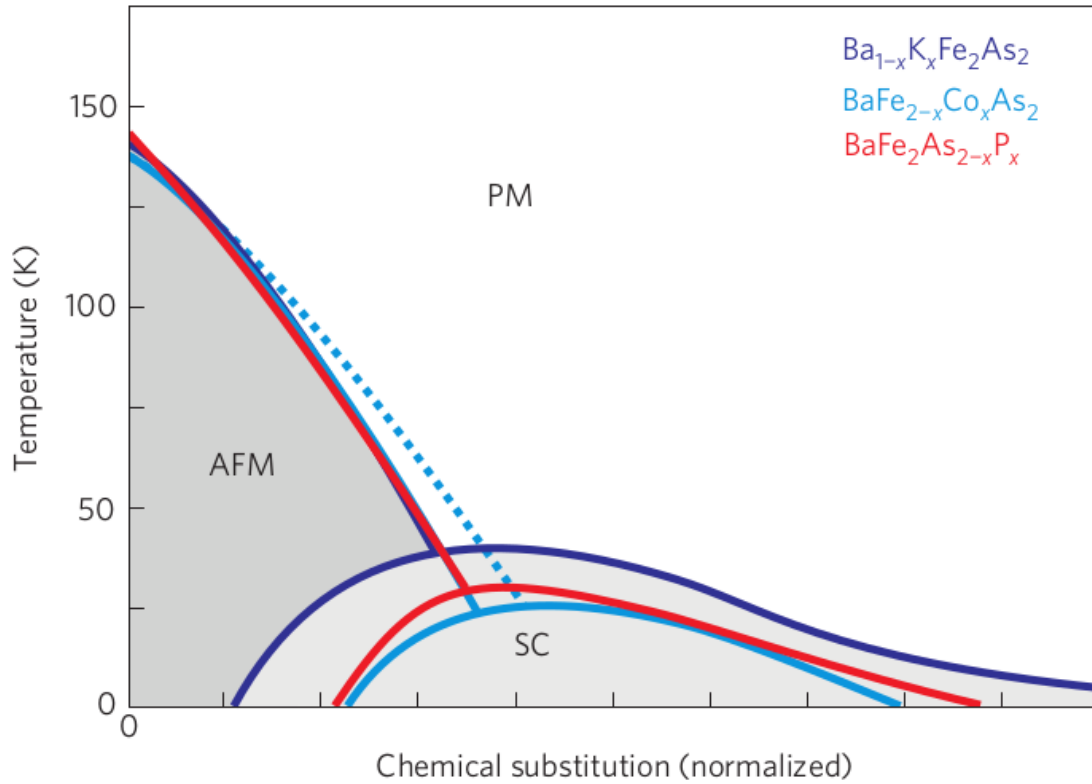


Figure 1.3: Phase diagrams of K-, Co- and P-substituted BaFe_2As_2 . The phase diagrams are in all cases qualitatively equivalent: the AFM and PM normal states are always present, as is the superconducting dome. Adapted from [25]. ©2010, Springer Nature.

Upon doping of different species, a superconducting dome develops with a maximum of T_c at the optimal doping level. In the normal state above the superconducting dome, the system is in a paramagnetic (PM) metallic state instead of an AFM one. Ba

can be substituted by K, resulting in an increase of the hole carriers and in superconductivity up to almost 40 K for the optimally doped system ($\text{Ba}_{1-x}\text{K}_x\text{Fe}_2\text{As}_2$ with $x \simeq 0.4$) [29]. Exchanging Fe with a transition metal (such as Co, Ni or Rh) yields an electron doped superconductor with critical temperature of about 24 K [34]. Also As can be substituted to obtain a superconductor with $T_c \simeq 29$ K [35]. In this case, it is introduced an isovalent species, such as P, that does not change the carrier doping level but exerts chemical pressure. Furthermore, a superconducting state can be found also applying external pressure [36]. As clear from Fig. 1.3, the phase diagrams achieved are in all cases qualitatively equivalent, suggesting that the basic underlying physics could be the same independently on how superconductivity is obtained [27].

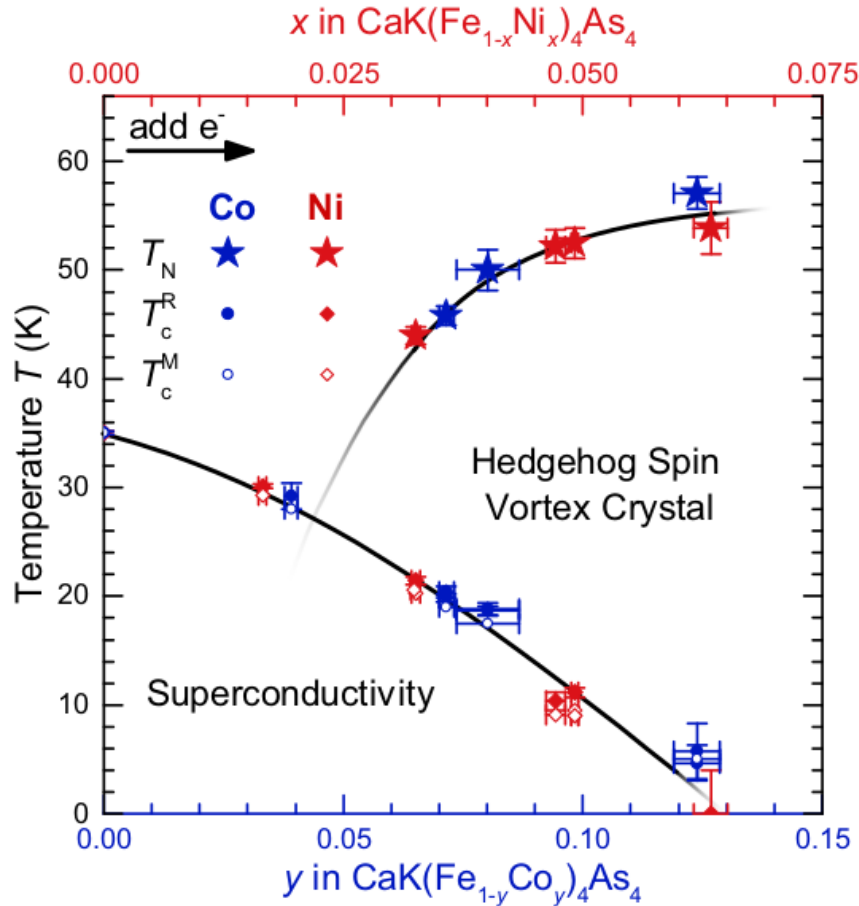


Figure 1.4: Phase diagrams of Ni and Co-substituted $\text{CaKFe}_4\text{As}_4$. Adapted from [32]. ©2018, Springer Nature.

In the case of the 1144 family (as well as others, *e. g.* the 1111 [37] and 111[38]) the undoped parent compound is by itself superconducting, and chemical doping results in a reduction of T_c [30]. This is clearly seen in the phase diagram of Ni- or Co-doped $\text{CaKFe}_4\text{As}_4$ shown in Fig. 1.4 [32]. However, the study of doped samples is also in this case extremely interesting because it induces a peculiar magnetic structure called Hedgehog spin vortex state [30, 32] and because Quantum Critical Points in the phase diagram can be revealed [30, 39].

1.4 Band structure

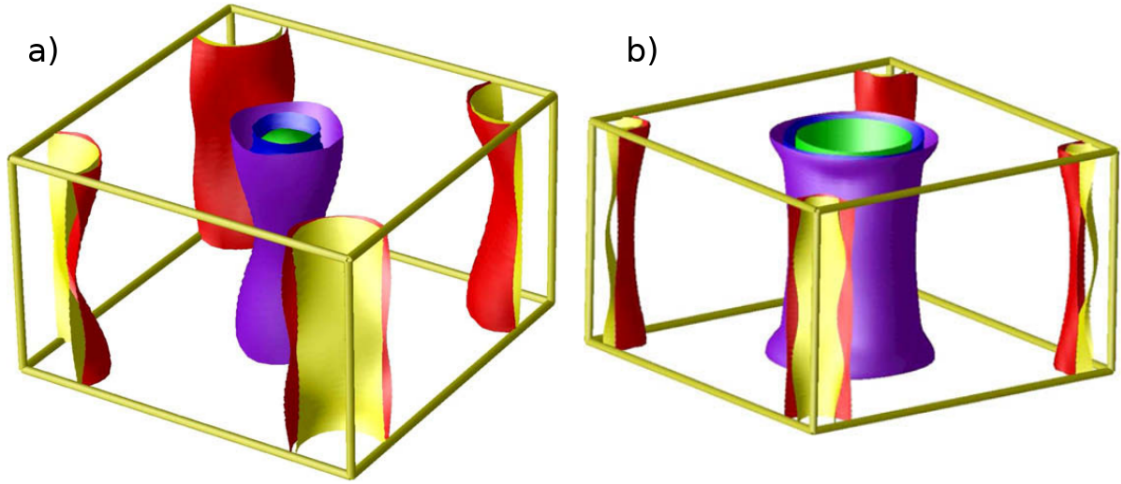


Figure 1.5: DFT calculated Fermi surfaces of BaFe_2As_2 for, a), 10% electron doping (approximately corresponding to optimal Co doping) and, b), 40% hole doping (optimal K doping). Blu, purple and green sheets are hole pockets whereas red and yellow ones are electron pockets. Adapted from [26]. ©2009, Elsevier.

IBSs, and in particular the 122 and 1144 families possess complex band structures and Fermi surfaces that have been investigated experimentally (mainly via Angle Resolved Photo-Emission Spectroscopy, ARPES) [40–43] and theoretically with Density Functional Theory, DFT, [44–46] with a good agreement between the two [47–49]. In these systems multiple bands (both electron and hole like) cross the Fermi Energy, E_F , with a dominant contribution of the d-orbitals of iron that bond metallicly in the active layers. This fact results in Fermi Surfaces (FSs) composed of several sheets with mostly cylindrical shapes [50]. Calculated FSs for the Ba-122 family, electron and hole doped,

are shown in Fig. 1.5 in the folded Brillouin zone representation with two iron atoms per unit cell. On the Γ point at $\mathbf{k}=(0,0)$ are centered the hole pockets (blue, purple and green), whereas the two electron like FSs (red and yellow) are at the M point at $\mathbf{k}=(\pi,\pi)$ [26].

The fact that the main contribution to the bands crossing E_F comes from the active planes makes the general shape of the FSs qualitatively similar in most compounds. The blocking layers in turn influence the height of the As sites relative to the Fe ones, changing therefore smaller details of the FSs, such as size of the pockets, their corrugation and their crossing [51]. These features therefore strongly change from one system to another, resulting in different superconducting properties. In particular, the nodal structure of the order parameter and the anisotropy of the effective mass, supercurrent and penetration depth are strongly influenced by small changes in the shape of FSs [42, 50].

1.5 Pairing mechanism and order parameter symmetry

In IBSs, the possibility of phonons-alone mediated Cooper pairing was quickly ruled out on the basis of their relatively high critical temperature, first principle calculations of electron-phonon coupling [12, 52] and, by isotope-effect experiments [53, 54]. However, it should be noted that electron-phonon coupling can be enhanced by an interplay with magnetism, making it a possible co-contributor to pairing in some specific cases [55, 56].

Electronic correlations are, in principle, another possible pairing mechanism: the features that IBSs share with the cuprates (in particular the presence of an AFM parent compound and of Spin Density Waves, SDW, in the phase diagram [57]) could indicate their primary role in pairing also in this newer class of materials. However, strong differences exist with the cuprates, the most evident of which is the absence of a Mott insulating state in the phase diagram of IBSs: a strong indication that electronic correlations in such systems are at most moderate [58].

The pairing mechanism that is most widely believed to be responsible for superconductivity in these systems is that of spin fluctuations, SF [12, 59]. The way they work can

be intuitively understood in a picture similar to that of phonon mediated superconductivity suggested by Fröhlich [60]. In that case an electron passing through the lattice generates a distortion (phonon) that attracts a second electron that pairs with the first forming a Cooper pair. In the case of SF, the picture is complicated by the presence of spin of the electrons and by the possible interactions (ferromagnetic or antiferromagnetic). If the first electron has spin up and the interaction is AFM, then it will polarize the surrounding spins to the down state. In order to have a spin singlet Cooper pair, the second electron needs to be in the spin down state, but it will see an unfavorable environment of other electrons with spin down. For this reason the interaction is repulsive and the Cooper pair can be formed only if the order parameter at the k-points of the two electrons have opposite sign. The importance of SF is strongly suggested by the strong magnetic features shown by these systems and by the evident interplay between magnetic signals and superconductivity. Signatures and hints of strong AFM-SF were observed experimentally in properties such as magnetic susceptibility [61], magnetic hyperfine spectrum [62], normal-state spin dynamics [63] and de Haas–van Alphen oscillations [64].

From a fundamental point of view it is important to consider that the sign of interaction mediated by SF in the case of singlet pairing (as it is in IBSs) is negative, *i. e.* the interaction is repulsive. However, repulsive interaction can be pairing if the parts of the FS that are connected by the wave vector of these fluctuations are characterized by order parameters with opposite sign [15]. In the case of IBS, the wave vector of AFM-SF is $(\pi, 0)$, too large to connect different parts of the same FS pocket [26]. The combination of the fermiology typical of IBSs and this type of interaction can only couple a FS located around the Γ point with one at the M point, therefore leading to a superconducting state in which the order parameters on hole and electron bands have opposite sign. This is the so-called s_{\pm} symmetry of the order parameter.

The details of such a systems can still vary strongly: an s_{\pm} state can be isotropic or anisotropic, it can present nodes with different topologies (accidental, equatorial or vertical lines, loops and more) and the magnitude of the gaps can vary strongly from one particular system to another [42, 50]. A few examples are schematically shown in Fig. 1.6.

A model alternative to that of AFM-SF that received lots of attention is that of orbital fluctuations proposed by Kontani *et al.* [65–67] that would result in the sign preserving s_{++} state. A fluctuating ordering of the d orbitals of iron, induced by the presence of

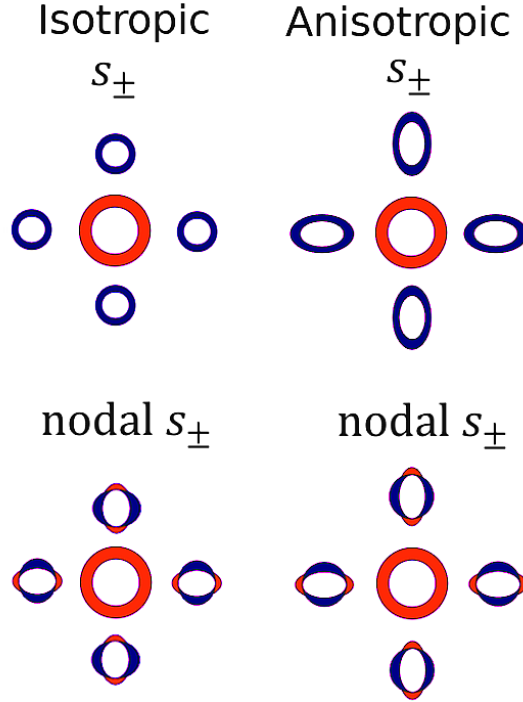


Figure 1.6: Schematic representation of possible realizations of the s_{\pm} symmetry of the order parameter in a two-bands case. The circles and ellipses represent planar cuts of the tubular FSs and red and blue represent positive and negative values of the gap.

magnetic stripes, could in principle lead to an attractive pairing mechanism that would give the s_{++} symmetry [68–70]. However, it seems that the strength of these fluctuations required to explain the observed characteristics of IBs are in contrast with DFT calculations [15, 55]. This stems from the fact that their contribution to the coupling can only appear in vertex corrections, but slow orbital fluctuations are excluded by the Migdal theorem, and fast ones are included in DFT calculations that yield a too weak coupling to explain the observed properties [15]. Therefore the mechanism orbital fluctuations that would give the s_{++} state, although possible, is likely to be of secondary importance with respect to the AFM-SF one that results in the s_{\pm} symmetry.

Chapter 2

Experimental technique

Part of the topics discussed in this chapter were published in Ref.s [71–74]

2.1 Experimental setup

As stated in the introduction, this work aims to investigate the fundamental features of IBSs by looking at the effects of disorder on their superconducting properties. In particular, strong indications about the order parameter symmetry can be deduced by studying the superfluid density, ρ_s , of a material: its value, its temperature dependence and the way it is affected by defects. This quantity, also called superfluid stiffness, represents the density of Cooper pairs in the condensate and is proportional to the inverse squared of the London penetration depth λ_L [75]:

$$\rho_s(T) = \frac{m^*}{\mu_0 e^2} \frac{1}{\lambda_L(T)^2}, \quad (2.1)$$

where m^* is the effective mass of the electrons, e is their charge and μ_0 is the vacuum magnetic permeability. This can be intuitively understood by thinking that a stronger, denser, condensate screens better external magnetic fields, and therefore has a smaller λ_L .

The analysis of the superfluid density and of the temperature dependence of its value normalized at $T = 0$ (the superfluid fraction $\rho_s(T)/\rho_s(0)$) are often carried out thanks to techniques that yield λ_L , a quantity that contains almost the same information, as

evident from Eq. 2.1. The London penetration depth can be estimated starting from measurements of optical conductivity [76], of vortex distribution in the mixed state [77, 78] and of the field of first penetration or of the lower critical field [79]. Another standard approach relies on the use of microwave radiation, and the most powerful techniques are resonant ones, since they grant very high sensitivity. In these cases λ_L can be obtained by measuring the perturbations to the resonance of a resonator caused by the presence of the sample in the cavity in a region where the rf magnetic field has a maximum and the electrical field has a node [80–82]. In addition, in order to study how the superconducting properties of a material are influenced by the presence of irradiation-induced disorder, it is important to investigate them with techniques that are not invasive on the samples, so that measurement can be performed on the same crystals before and after each irradiation session. This is very important because different samples, although nominally similar, could have small differences that can be mistakenly attributed to the irradiation process.

In our group a technique was developed [82, 83], and I contributed to its improvement

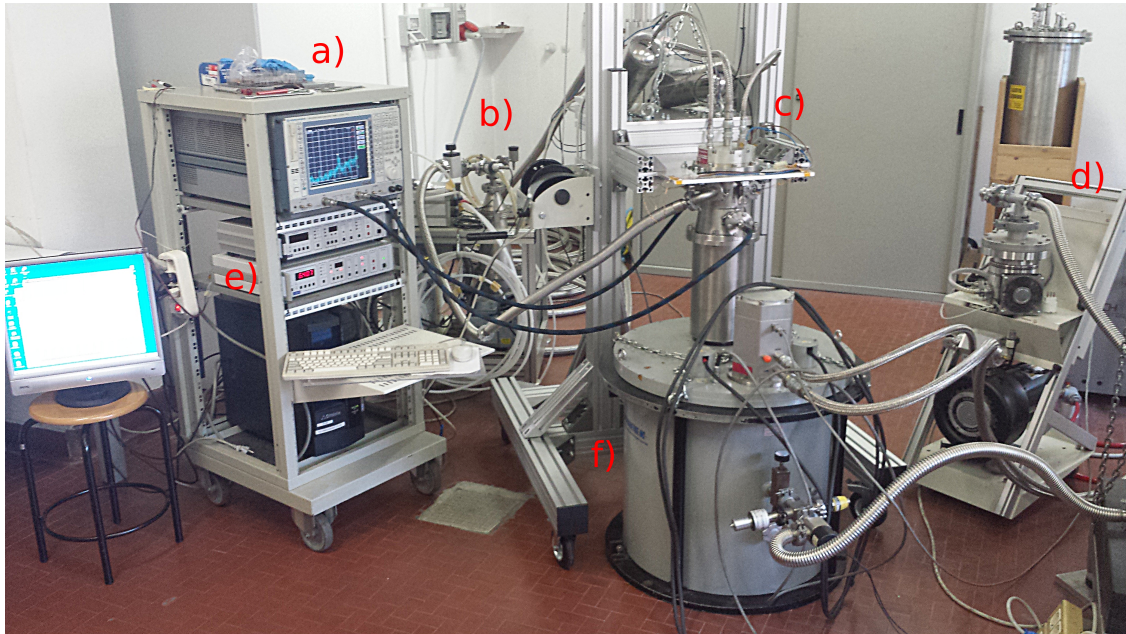


Figure 2.1: The experimental setup: a) network analyzer, b) vacuum system, c) cryocooler, d) and f) superconducting magnet and its vacuum system, e) temperature controller.

during my PhD, to satisfy these requirements and measure the London penetration

depth of small single crystals of superconductors with T_c s ranging from about 15 K to 60 K. The experimental setup (a picture of which is shown in Fig. 2.1) consists of:

- a vacuum system that reaches 3.0×10^{-5} mbar, equipped with vibration dampers,
- a Cryomech PT-415 pulse-tube cooler that allows to obtain a base temperature at the sample position of about 5 K (limitations on the minimum temperature are mainly due to the heat carried in by the coaxial cables),
- an Oxford temperature controller ITC503 equipped with a Cernox thermometer and two heaters that allow us to measure and control the temperature near the sample position with a 0.001 K sensibility,
- a Rohde Schwarz ZVK vector-network-analyzer that can operate up to 40 GHz,
- the measurement cell that consists of a coplanar waveguide resonator (CPWR) obtained from a $\text{YBa}_2\text{Cu}_3\text{O}_{7-x}$ (YBCO) film of thickness of 250 nm grown on a non magnetic MgO substrate. The resonator was patterned in-house by standard optical lithography on a commercial THEVA GmbH [84] film with $T_c = 88$ K [85]. The geometry is optimized to match the impedance (50Ω) of the measuring system and to have a resonance frequency of about 8 GHz: the central strip is $350 \mu\text{m}$ wide and each ground plane is distant from it $150 \mu\text{m}$. The YBCO film is positioned into a brass closed structure equipped with RF launchers.

The measurement cell is mounted on a long stand so that, if needed, it can be inserted in the bore of a magnet to perform measurement with external DC magnetic field applied. Investigated samples are high quality single crystals cut and cleaved to have the shape of small platelets with the c -axis along the thickness. Typical dimensions are $2a \times 2b \times 2c = 250 \times 350 \times 10 \mu\text{m}^3$, with the constraints that the width $2a$ must be smaller than the width w of the central strip of the resonator (see scheme in Fig. 2.2) and the thickness $2c$ must be smaller than the implantation depth of the ions used to introduce disorder in the system.

The sample under study is coupled to the CPWR by placing it with the broad face on the film at the center of the waveguide strip with a small amount of vacuum grease that ensures adhesion and good thermal contact. At this position, the electric field generated by the resonator has a node and the magnetic field has a maximum. Moreover, far from the strip edges ($10 \mu\text{m}$), the magnetic field is uniform within 5% and the only

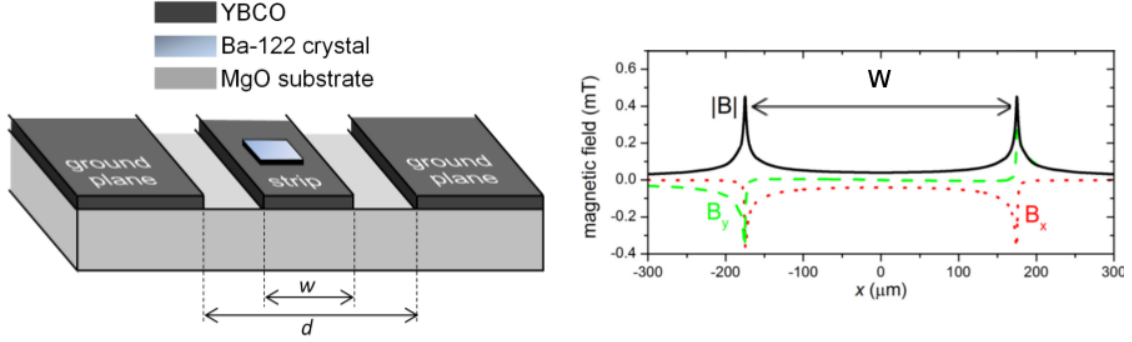


Figure 2.2: Left: schematic illustration of the CPWR with the IBS sample coupled to it. Right: rf magnetic field distribution at the sample position. Adapted from [82, 83]. ©2017, American Physical Society and ©2016 IEEE.

nonzero component is the one parallel to the film surface, and in particular to w (in the ab -crystallographic plane of the sample). The field was evaluated (right side of Fig. 2.2) using the Biot-Savart law on the current density distribution $j^{rf}(x)$ for the center conductor of a CPWR given by [86]:

$$j^{rf}(x) = \frac{I_{tot}}{K\left(\frac{w}{d}\right)w\sqrt{\zeta(x)}} \quad (2.2)$$

where x is the coordinate along the transverse direction, I_{tot} is the total current,

$$\zeta(x) = \begin{cases} \frac{\lambda_{eff}}{w} \left[1 - \left(\frac{w}{d}\right)^2 \right], & 0 \leq \frac{w}{2} - |x| < \lambda_{eff} \\ \left[1 - \left(\frac{2x}{w}\right)^2 \right] \left[1 - \left(\frac{2x}{d}\right)^2 \right], & |x| < \frac{w}{2} - \lambda_{eff} \end{cases} \quad (2.3)$$

K is the complete elliptic integral and the effective penetration depth of the YBCO thin film is $\lambda_{eff} = \lambda_L \coth(t/2\lambda_L)$. The resulting rf magnetic field produced at the sample position is the probe for the superconducting properties of the material.

An input power in the range of -20 to -40 dBm is used for the measurement, well below the nonlinearity threshold of the resonator and high enough to obtain a clean signal. The transmission coefficient S_{21} of the system composed of the resonator and sample is continuously recorded in a frequency window of about 25-50 MHz around the resonance frequency, while the system is slowly heated from the base temperature to about 20-30K

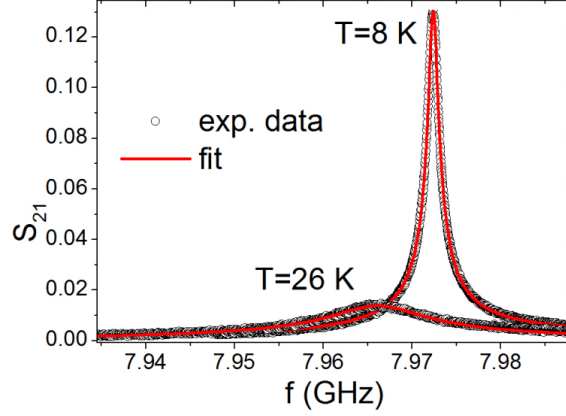


Figure 2.3: Frequency dependence of the transmission coefficient of the resonator with the sample (optimally Rh-doped Ba-122 in this case) coupled to it below and above the critical temperature of the material. Red curves are the fit described in the text.

above the T_c of the sample. The typical heating rate is 0.25K/min, slow enough to ensure that no thermal drift effects influence the resonance curves. As shown in Fig. 2.3, each $S_{21}(T)$ curve is fitted with a Lorentzian function ($S_{21}(f) = S_{21}^{max} / \sqrt{1 + Q_L^2 (f/f_0 - f_0/f)^2}$) superimposed to a linear background to yield the resonance frequency, f_0 and loaded quality factor Q_L of the system at a particular temperature. From Q_L it is possible to calculate the unloaded quality factor, Q_0 , as $Q_0 = Q_L / (1 - S_{21}^{max})$. Performing the temperature scan yields then the $f_0(T)$ and $Q_0(T)$ curves, an example of which is shown in red in Fig. 2.4. A second measurement is performed after the sample has been removed, giving the reference $f_0(T)$ and $Q_0(T)$ curves for the resonator alone (gray symbols in Fig. 2.4). The relative shifts $\Delta f_0/f_0$ and $\Delta(1/Q_0)$ are then computed in order to analyze the perturbations to the resonance of the resonator induced by the presence of the sample.

2.2 Cavity perturbation method

The response of a resonator can be characterized by the complex angular frequency $\omega = \omega' + j\omega''$, and its quality factor and resonance frequency can be expressed respectively, as [87]

$$Q_0 = \frac{\omega'}{2\omega''} \quad f_0 = \frac{\omega'}{2\pi}. \quad (2.4)$$

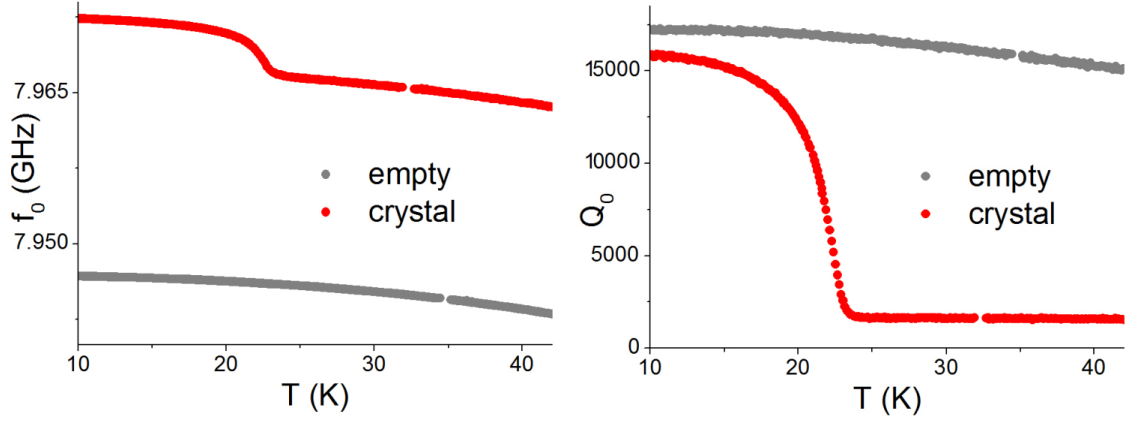


Figure 2.4: Temperature dependence of the resonant frequency and quality factor of the resonator only (gray symbols) and of the resonator with the sample coupled to it (red symbols) for an optimally Rh-doped Ba-122.

When a sample is coupled to the resonator, provided that it is much smaller than the cavity (as it is in our case) and therefore the electromagnetic field outside of it does not change significantly, the angular frequency shift due to the presence of the sample can be calculated as [87]

$$\frac{\omega - \omega_0}{\omega} = - \frac{\int_{V_S} (\Delta\epsilon \mathbf{E} \cdot \mathbf{E}_0^* + \Delta\mu \mathbf{H} \cdot \mathbf{H}_0^*) dV}{\int_{V_C} (\epsilon_0 \mathbf{E} \cdot \mathbf{E}_0^* + \mu_0 \mathbf{H} \cdot \mathbf{H}_0^*) dV} \quad (2.5)$$

where the subscript 0 indicates that the sample is absent. The asterisks denote complex conjugates, V_S and V_C are the sample and cavity effective volumes, respectively. In our case the sample is positioned in a region where \mathbf{E} has a node, and elsewhere $\mathbf{E} \approx \mathbf{E}_0$, $\mathbf{H} \approx \mathbf{H}_0$. By assuming that $\omega' \approx \omega'_0$ and $Q, Q_0 \gg 1$, Eqs. give:

$$\left(\frac{f - f_0}{f} \right) + j \left(\frac{1}{2Q} - \frac{1}{2Q_0} \right) \approx - \frac{\int_{V_S} (\mu - \mu_0) |\mathbf{H}_0|^2 dV}{2 \int_{V_C} \mu_0 |\mathbf{H}_0|^2 dV} \approx - \frac{1}{2} \Gamma \chi \quad (2.6)$$

where $\Gamma \approx V_S/V_C$ takes into account all the geometrical factors connected to the distribution of the fields in the cavity and χ is the complex magnetic susceptibility. In our specific case of perturbation approach, the frequency and quality factor shifts are affected in slightly different ways by the presence of the sample, therefore two geometrical factors are needed [87]. For a superconductor with non negligible losses, χ can be

related to the complex propagation constant κ of the rf electromagnetic wave (which in turn is related to λ_L) yielding:

$$2 \frac{\Delta f_0}{f_0} = \Gamma \left\{ 1 - \Re \left[\frac{\tanh \kappa c}{\kappa c} \right] \right\}, \quad (2.7)$$

$$\Delta \left(\frac{1}{Q_0} \right) = \Gamma' \Im \left[\frac{\tanh \kappa c}{\kappa c} \right], \quad (2.8)$$

where c is the half-thickness of the crystal, Γ and Γ' are the two geometrical constants related to the effective magnetic volume of the sample in the resonator.

2.3 Calibration procedure

The geometrical constant Γ and Γ' unfortunately can not be calculated with an acceptable accuracy for the open geometry of our measurement system. For this reason their values need to be determined from a self-consistent calibration procedure that makes use of the experimental data measured above the critical temperature of the investigated sample. Above T_c IBs are metallic (although not excellent metals). For a metal, the real and imaginary parts of the propagation constant κ are related to the classical skin depth δ by: $\Re(k) = \Im(k) = 1/\delta$. The classical skin depth is the thickness of the region in which screening currents are present when the sample is exposed to an alternating magnetic field, and is related to the resistivity ρ of the sample and to the frequency of the external field ω by $=\sqrt{2\rho/(\omega\mu_0)}$, where μ_0 is the vacuum permeability. Due to the geometry of our measurement cell and to the small dimension of the investigated crystals, that can not be considered infinite in any dimension, we need to consider that the field penetrates in the metallic sample from all sides due to demagnetization effects. Therefore, instead of only the term $(\tanh \kappa c)/\kappa c$ in Eqs. 2.7 and 2.8, that is valid for an infinitely large slab, we consider a sum over all three dimensions of analogous terms. In addition, we notice that $\tanh z = (\sinh 2x + i \sin 2y)/(\cosh 2x + \cos 2y)$ where $z = x + iy$. With these considerations in mind one can rewrite Eqs. 2.7 and 2.8 as:

$$2 \frac{\Delta f_0}{f_0} = \Gamma \left\{ 1 - \sum_1^3 A(x_i) \right\} \quad \Delta \left(\frac{1}{Q_0} \right) = \Gamma' \sum_1^3 B(x_i), \quad (2.9)$$

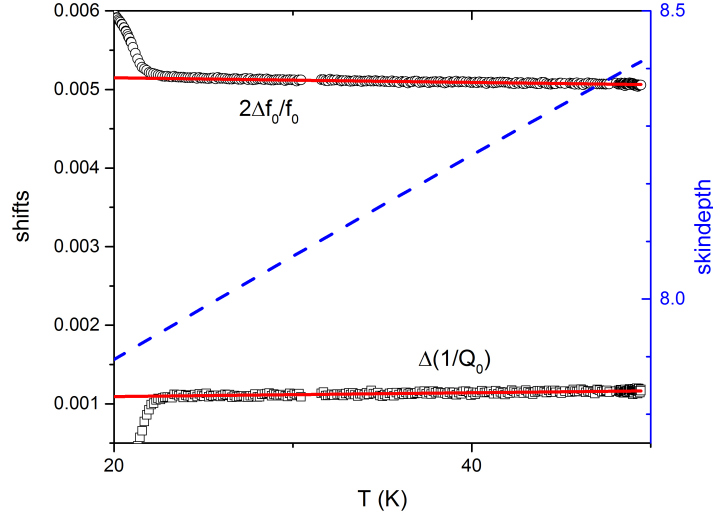


Figure 2.5: Resonance frequency and quality factor relative shifts above T_c , induced by the presence of a Rh-doped Ba122 sample (symbols) and their fits by means of Eqs. 2.9 and 2.10 (red solid lines), as discussed in the text, the same resistivity and therefore skin depth (blue dashed line) is used for both curves.

where

$$A(x_i) = \frac{\delta \sinh(2x/\delta) + \sin(2x/\delta)}{2x_i \cosh(2x/\delta) + \cos(2x/\delta)} \quad B(x_i) = \frac{\delta \sinh(2x/\delta) - \sin(2x/\delta)}{2x_i \cosh(2x/\delta) + \cos(2x/\delta)}. \quad (2.10)$$

At this point one can fit the experimental $\Delta f_0/f_0$ and $\Delta(1/Q_0)$ data above T_c (an example is shown in Fig. 2.5) using the same resistivity for both curves and fixing the geometrical factors Γ and Γ' . It should be noted that the temperature dependence of $\Delta f_0/f_0$ and $\Delta(1/Q_0)$ is mainly due to the temperature dependence of the resistivity, and that contributions given by the sample thermal expansion are negligible. The two geometrical factors found usually differ less than 20% from each other. The difference stems from the fact that the shift of Q_0 due to the perturbation is not only given by the imaginary part of the sample permittivity but also, to a much smaller extent, by its real part [87].

2.4 Measured quantities

The calibration procedure described in detail in the previous paragraph allows one to calculate the propagation constant κ in the material in the whole temperature range. In this way one can extract from the raw experimental data information about the properties of the investigated sample. In particular one can obtain the London penetration depth λ_L (from which the superfluid density can be calculated) and the quasiparticle conductivity σ_n . Typical results of the measurement are shown in Fig. 2.6 for the case of a Rh-doped Ba122 syngle crystal. In this section, the procedure to extract λ_L and σ_n is explained.

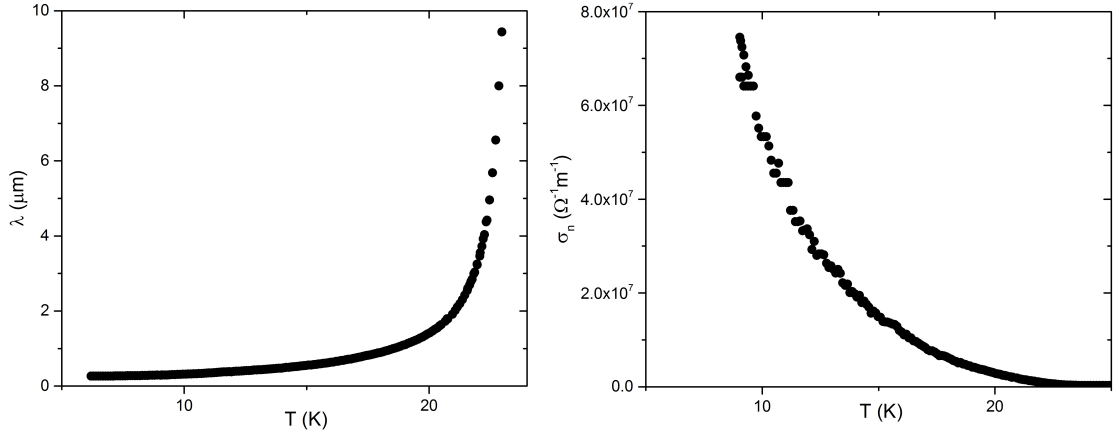


Figure 2.6: Typical outcome of the measurements performed with the CPWR technique: $\lambda_L(T)$ (left) and $\sigma_n(T)$ (right) here for an optimally Rh-doped Ba122 syngle crystal.

Employing also below T_c the geometrical factors values obtained from the calibration procedure above T_c , Eqs. 2.7 and 2.8 can be inverted to yield the real and imaginary part of the propagation constant $\kappa = \alpha + i\beta$ over the whole temperature range. Specifically, the equations solved for α and β are:

$$\frac{\alpha \sinh(2\alpha c) + \beta \sin(2\beta c)}{c (\alpha^2 + \beta^2)(\cosh(2\alpha c) + \cos(2\beta c))} = \Re \left(\frac{\tanh(\kappa c)}{\kappa c} \right)_{exp} \quad (2.11)$$

$$\frac{\alpha \sinh(2\beta c) - \beta \sin(2\alpha c)}{c (\alpha^2 + \beta^2)(\cosh(2\alpha c) + \cos(2\beta c))} = \Im \left(\frac{\tanh(\kappa c)}{\kappa c} \right)_{exp} \quad (2.12)$$

It should be noted that, at this stage, demagnetization effects (*i. e.* the penetration of

fields from all sides of the sample) are disregarded: they are accounted for, unitedly with anisotropy, by the approach explained in the next section. From the obtained α and β it is possible to calculate the London penetration depth and quasiparticle conductivity since they are related by [88]:

$$\kappa = \alpha + i\beta = \sqrt{1/\lambda_L^2 + i\omega\mu_0\sigma_n} \quad (2.13)$$

Specifically, Eq. 2.13 can be rewritten as:

$$\sqrt[4]{1/\lambda_L^4 + \omega^2\mu_0^2\sigma_n^2} \cos\left(\frac{\arctan(\omega\mu_0\sigma_n\lambda_L^2)}{2}\right) = \alpha \quad (2.14)$$

$$\sqrt[4]{1/\lambda_L^4 + \omega^2\mu_0^2\sigma_n^2} \sin\left(\frac{\arctan(\omega\mu_0\sigma_n\lambda_L^2)}{2}\right) = \beta \quad (2.15)$$

that are solved numerically to yield λ_L and σ_n . Moreover these two quantities are connected with the surface impedance of the sample Z_s by [86]

$$Z_s = R_s + iX_s = \frac{i\omega\mu_0\lambda_L}{\sqrt{1 + i\omega\mu_0\sigma_n\lambda_L^2}}. \quad (2.16)$$

Therefore one can use them to calculate the surface resistance R_s and reactance X_s as:

$$R_s = \frac{\omega\mu_0\lambda_L}{\sqrt[4]{1 + \omega^2\mu_0^2\sigma_n^2\lambda_L^4}} \sin\left(\frac{\arctan(\omega\mu_0\sigma_n\lambda_L^2)}{2}\right), \quad (2.17)$$

$$X_s = \frac{\omega\mu_0\lambda_L}{\sqrt[4]{1 + \omega^2\mu_0^2\sigma_n^2\lambda_L^4}} \cos\left(\frac{\arctan(\omega\mu_0\sigma_n\lambda_L^2)}{2}\right). \quad (2.18)$$

In summary, this CPWR technique allows to measure at the same time the temperature dependence of the London penetration depth, of the quasiparticle conductivity and of the surface impedance of small single crystals with T_c in the range between 15 and 60 K without the risk of damaging them (because there is no need of soldering contacts onto the sample).

As previously stated, measurements of λ_L give access to the superfluid density, but the

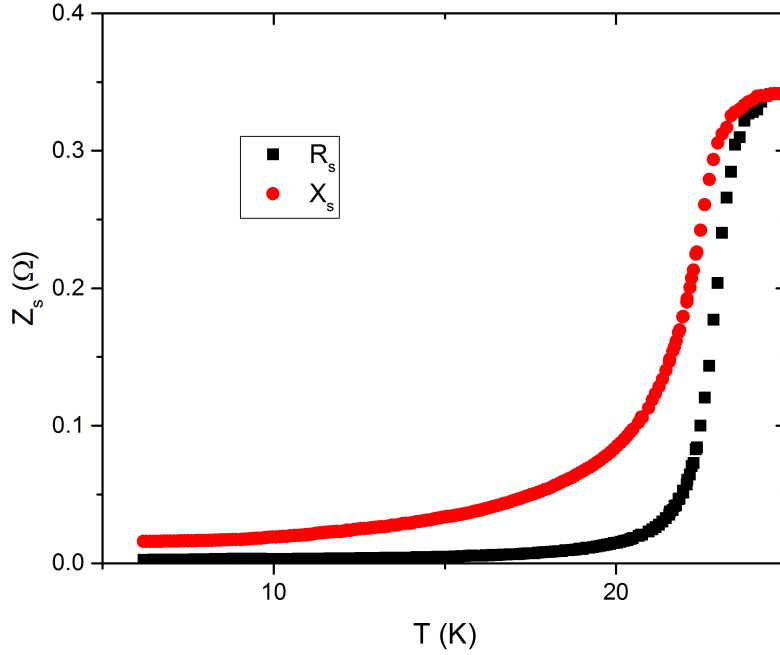


Figure 2.7: Surface impedance of a Rh-doped Ba122 sample calculated with the procedure explained in the text from the measured λ_L and σ_n showed in Fig. 2.6.

London penetration depth is a very interesting quantity *per se*, since it can give an insight on the nodal character of the superconducting gap [89], on its symmetry [90, 91], and even on the presence of quantum critical points (QCP) in the phase diagram of specific systems [39, 92–94]. The low temperature variation of its value with temperature, $\Delta\lambda_L(T \ll T_c)$, is dependent on the amount of thermally excited quasiparticles. For this reason, a fully gapped Fermi surface results in an exponential behavior, whereas a linear dependence on T is obtained for the case of gaps with line nodes. If disorder is introduced in the system, a quadratic dependence on T is expected in the limit of a dirty superconductor regardless the symmetry of the order parameter. In addition, for a clean superconductor, the absolute value of the London penetration depth $\lambda_L(0)$ depends only on the normal state properties, specifically on the effective mass of the carriers: $\lambda_L^2(0) \sim m^*$ [75]. Since near a quantum phase transition the effective mass is enhanced, measurements of $\lambda_L(0)$ for different values of doping of an IBS system can reveal a QCP if a peak is observed. Moreover, λ_L is one of the two length scales of a superconductor (together with the correlation length ξ) and determines the properties of vortex matter in the mixed state [77].

Since the most important quantity obtained from our measurements is λ_L , it is worth comparing this technique with the most common alternative ones to highlight its strengths and weaknesses.

A similar approach to the one explained here is used with the tunnel diode resonator (TDR) technique [95]. In this case the rf field is generated by a coil and the sample is inserted in the middle of the coil where the magnetic field is most uniform. The tunnel diode is biased to a region in which it has a negative differential resistance, so that it compensates for the losses mostly due to the presence of the sample, resulting in a self-resonating oscillator [96]. This means that the TDR is automatically always locked exactly at its resonant frequency. The shifts of f_0 caused by the variation of the AC magnetic susceptibility of the sample are recorded with an extremely high precision (down to 0.1 Hz with respect to an operating f_0 in the range of 10 to 100 MHz). However, the fact that the system is locked to operate always at f_0 does not allow to measure the quality factor of the resonance, for this reason only variations of the London penetration depth with temperature ($\Delta\lambda_L(T)$) can be obtained with this technique [97], but not its absolute value ($\lambda_L(0)$ that can be determined only with coating procedures that damage the sample [98]).

Another technique often used to obtain information about the superfluid density is muon spin rotation (μ SR) [77]. For this technique a source of muons is obviously needed, so it is performed at dedicated facilities. Muons are implanted in the sample under study and are a local probe for the bulk properties of the materials. From their precession, dephasing and relaxation it is possible, through the application of specific models, to obtain information about the magnetic field distribution inside the sample. The superfluid density is usually obtained studying the mixed state of type II superconductors and, specifically, the vortex lattice arrangement and intervortex distance that depends on the value of λ_L . This is the most important difference with respect to the CPWR and TDR techniques that, in contrast, make use of weak magnetic fields smaller than H_{c1} . It is also worth mentioning that the London penetration depth can also be calculated starting from measurements of the field of first vortex penetration H_p that can be related to the lower critical field H_{c1} if demagnetization effects for the specific geometry of the sample are considered [99]. Therefore, any magnetometry technique that is very sensitive to weak magnetic fields can be used to infer λ_L [100]. One specific example that has been developed recently is the NV-centers-in-diamond magnetometry

technique [101]. H_p is measured by looking at the the optically-detected magnetic resonance (ODMR) between energy levels split by the Zeeman effect in the NV centers of a diamond indicator that is positioned directly on the top of a sample. This technique, although precise, has the drawbacks of being slow, of needing very well geometrized samples and of relying also on the estimate of the correlation length from measurements of the upper critical field H_{c2} [79]. In order to compare some of these techniques, test their similarities and differences, verify the agreement between their outcomes and take advantage of their complementarity, I was invited by Prof. Prozorov to the Ames Laboratories where some of these techniques are routinely employed to study with multiple techniques $\text{CaKFe}_4\text{As}_4$ samples [74].

2.4.1 Anisotropy of λ_L

In our geometry the applied rf magnetic field that probes the sample properties is oriented in plane and not along the c -axis, therefore the measurements yield an effective penetration depth λ_L that is a combination of the main in-plane and out-of-plane components $\lambda_{L,ab}$ and $\lambda_{L,c}$. These two quantities can be similar or very different depending on the material, and the way they combine to give λ_L depends on the geometry of the sample measured. Therefore, the anisotropic contributions can be deconvolved from the measured λ_L , by studying samples with different aspect ratios and analyzing how they combine.

Since the samples are small (and therefore can not be considered infinite in any direction), one should consider that the penetration of the magnetic field occurs starting from all sides of the sample due to demagnetization effects. The screening supercurrent is therefore in plane (j_{ab}) in a thickness $\lambda_{L,ab}$ along the c -axis from both bottom and top faces, and out of plane j_c in a thickness $\lambda_{L,c}$ along the a and b directions from the two sides. With this in mind, and limiting to the case in which $\lambda_{L,ab} \ll c$ and $\lambda_{L,c} \ll a, b$, the fraction of volume penetrated by the field can be estimated as $\lambda_{L,ab}/c + \lambda_{L,c}/a + \lambda_{L,c}/b$ [82]. Thus, the penetration depth that is measured with the procedure described in the previous sections can be expressed as:

$$\lambda_L = \lambda_{L,ab} + f_s \cdot \lambda_{L,c}, \quad (2.19)$$

where $f_s = c \cdot (1/a + 1/b)$ is the shape factor of the sample.

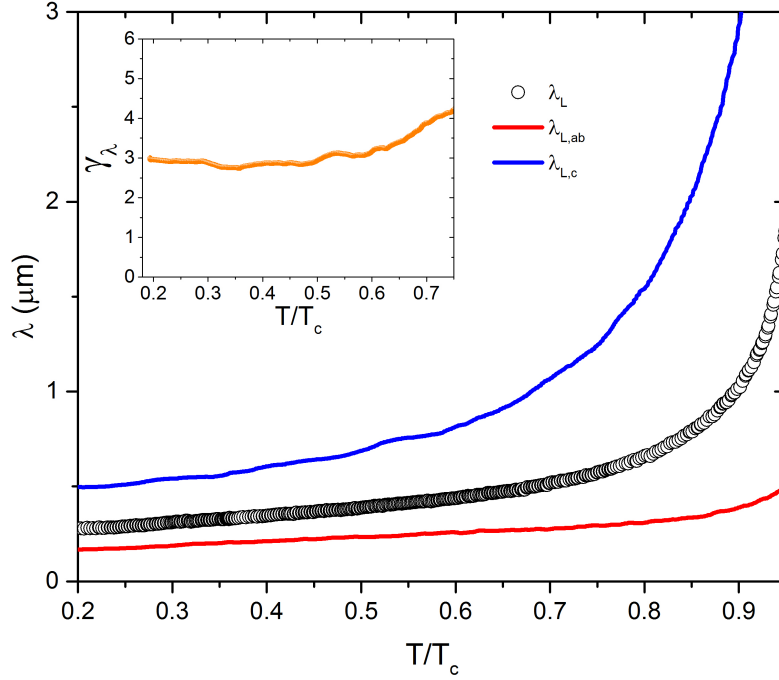


Figure 2.8: Measured λ_L as a function of reduced temperature of a $\text{CaKFe}_4\text{As}_4$ sample (black circles) and the $\lambda_{L,ab}$ and $\lambda_{L,c}$ components (red and blue solid lines respectively) obtained with the procedure explained in the text. The inset shows the anisotropy factor γ_λ .

Therefore, it is possible to deconvolve the $\lambda_{L,ab}$ and $\lambda_{L,c}$ contributions from the total λ_L measured on two samples with very different shape factors f_s [82]. This procedure allows to determine the anisotropy parameter $\gamma_\lambda = \lambda_{L,c}/\lambda_{L,ab}$. This quantity can have a temperature dependence and from its features it is possible to discuss both intrinsic quantities, such as multigap character [102], nodes in the gap [103, 104] and contributions coming from disorder [105]. In Fig. 2.8 these quantities are shown for the $\text{CaKFe}_4\text{As}_4$ system as an example.

The possibility to obtain the in plane component of the London penetration depth is also crucial to compare the results found by different experimental techniques, since most of them yield only a measurement of $\lambda_{L,ab}$. In Figure 2.9 the CPWR results on $\text{CaKFe}_4\text{As}_4$ are compared to measurements performed with the TDR technique to obtain the $\Delta\lambda_{L,ab}(T)$ combined with the NV-centers-in-diamond magnetometry technique to obtain $\lambda_{L,ab}(0)$ during my stay at the Ames Laboratory in the group of Prof. R. Prozorov. The $\lambda_{L,ab}(0)$ values obtained with the two techniques are remarkably close (170 ± 20 for

CPWR and 196 ± 12 nm for NV) and also the temperature dependence shows an overall agreement, representing an important validation of the experimental techniques.

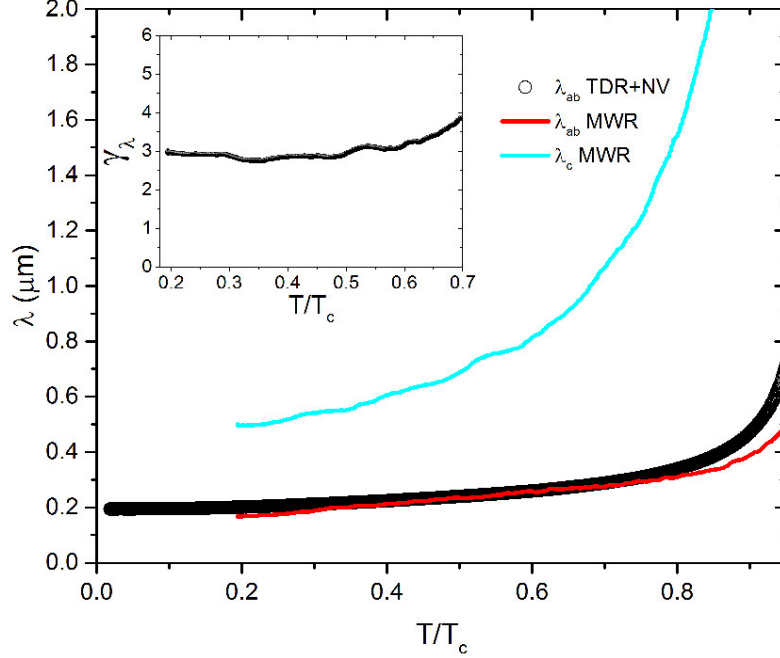


Figure 2.9: Deconvolved components $\lambda_{L,ab}$ and $\lambda_{L,c}$ (red and cyan lines respectively) and anisotropy factor γ_λ (in the inset) from CPWR measurement on $\text{CaKFe}_4\text{As}_4$. The $\lambda_{L,ab}(T)$ obtained on the same material from the combination of TDR and NV measurements is shown for comparison as black circles. Adapted from [74]. ©2019 American Physical Society.

2.4.2 Uncertainty analysis

In the present section, an analysis of the sources of uncertainty in the experimentally determined value of λ_L is carried out for a typical case.

The uncertainty in λ_L depends mainly on:

- uncertainty in the determination of resonance frequency and quality factor by Lorentzian fitting
- noise in the measurement
- uncertainty in the determination of the temperature during the frequency scan (heat ramp dependance)

- possible small differences in the CPWR properties due to heating and cooling
- uncertainty in the determination of the crystal thickness
- uncertainty in the calibration (determination of the geometrical factors)

The first four sources affect the value of $\Delta f/f$ and $\Delta(1/Q)$, whereas the last two the value of Γ and Γ' in eq.s 2.7 and 2.8. Both these uncertainties then propagates to affect λ_L by affecting first the real and imaginary part of $\tanh(kc)/kc$.

Let us now estimate one by one the sources of uncertainty for the typical measurement. The Lorentzian fits (as the ones visible in Fig. 2.3) are extremely reliable, with each fit yielding a reduced chi-squared $\tilde{\chi}^2 \lesssim 1$, resulting in an uncertain on the extracted values that is negligible if compared to other sources.

The noise of the measurement can be estimated by the spread of experimental data taken at the same temperature (shown in Fig. 2.10).

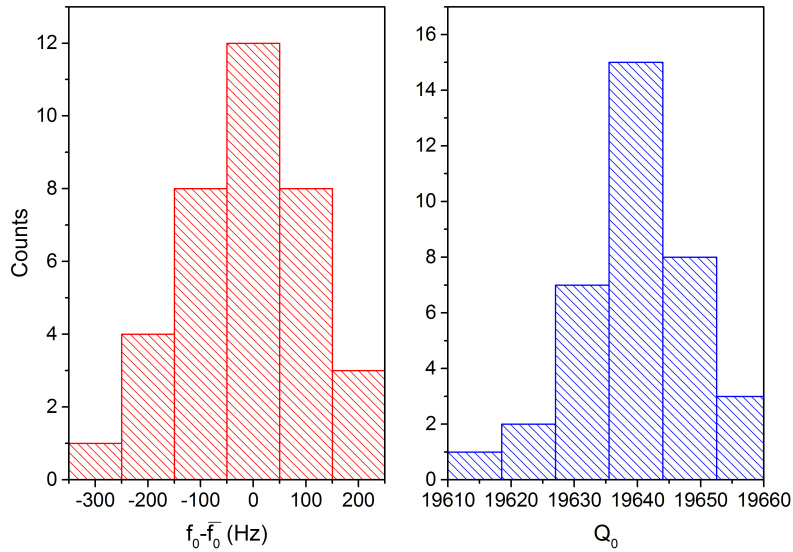


Figure 2.10: Distribution of the f_0 and Q_0 values of the empty resonator taken at $6.10\text{K} \pm 0.01\text{ K}$. The relative variation is $2 \cdot 10^{-6}\%$ for f_0 and 0.05% for Q_0 . \bar{f}_0 is the average value of f_0 .

During the 5 seconds long frequency scan, the temperature varies of about 0.02 K

with the typical temperature ramp. The temperature is read before and after each frequency scan and the average value is assigned to the frequency and quality factor obtained during the frequency scan. The uncertainty on the temperature measurement can be considered to be $\pm 0.01\text{K}$. Measurements carried out in heating and cooling mode with the same rate yield no differences in the $f_0(T)$ and $Q_0(T)$ curves, as well as measurements carried out with lower heating rates, ensuring that the measured temperature is the sample temperature.

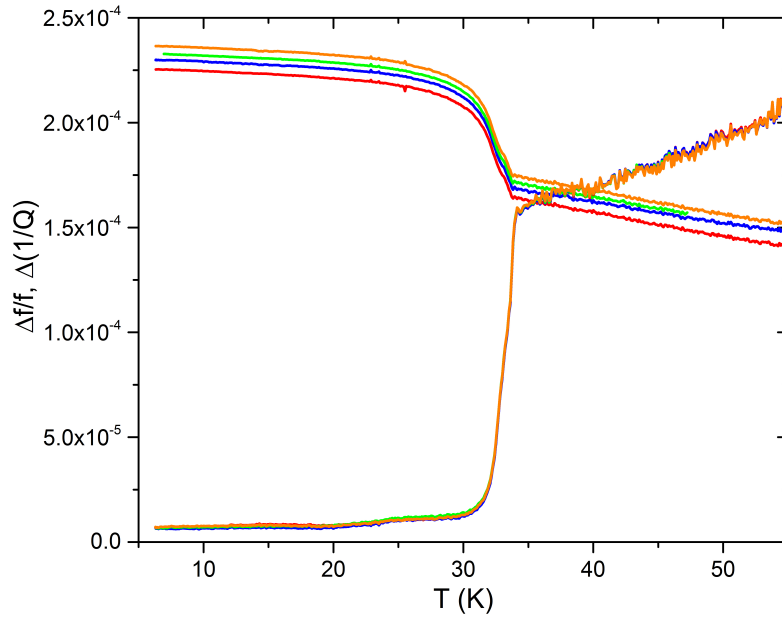


Figure 2.11: $\Delta f/f$ and $\Delta(1/Q)$ curves obtained by repeated measurements (several days apart) of the empty resonator that has been brought to room temperature between each measurement.

Due to the need to extract the sample from the system at room temperature between the measurement with the sample and the reference measurement, the CPWR properties may change slightly. However, the influence of these modifications are minor, as visible from Fig. 2.11 where $\Delta f/f$ and $\Delta(1/Q)$ curves obtained with several measurements of the same empty resonator are compared. The maximum spread of $\Delta f/f$ values is smaller than 5% and that of $\Delta(1/Q)$ is smaller than 10%. This is to be considered a worst case scenario since this spread is the result of measurements several days apart and for which the system experienced a large number of heating and cooling cycles,

whereas the real reference measurement is always done directly after the measurement with the sample. Moreover, the modifications are close to a rigid shift, therefore they do not affect the temperature dependence of λ_L , and they can be effectively accounted for during the determination of the geometrical factors in the calibration procedure, yielding a rather small influence also on the absolute value.

The uncertainty on the determination of the crystal thickness is about $0.5 \mu\text{m}$, and in the case of particularly thin samples it can be the major source of uncertainty since it directly affects the determination of the penetration depth. In fact, at low temperature the London penetration depth is approximately $\lambda_L \simeq c \cdot [(\Delta 1/Q)^2 + (2\Delta f/f - \Gamma)^2] / [\Gamma(\Gamma - 2\Delta f/f)]$.

Finally, the uncertainty related to the calibration procedure itself (and therefore on the geometrical factors) is usually negligible due to the strong constraints given by the temperature dependence of both $\Delta f/f$ and $\Delta(1/Q)$ (as visible in Fig. 2.5).

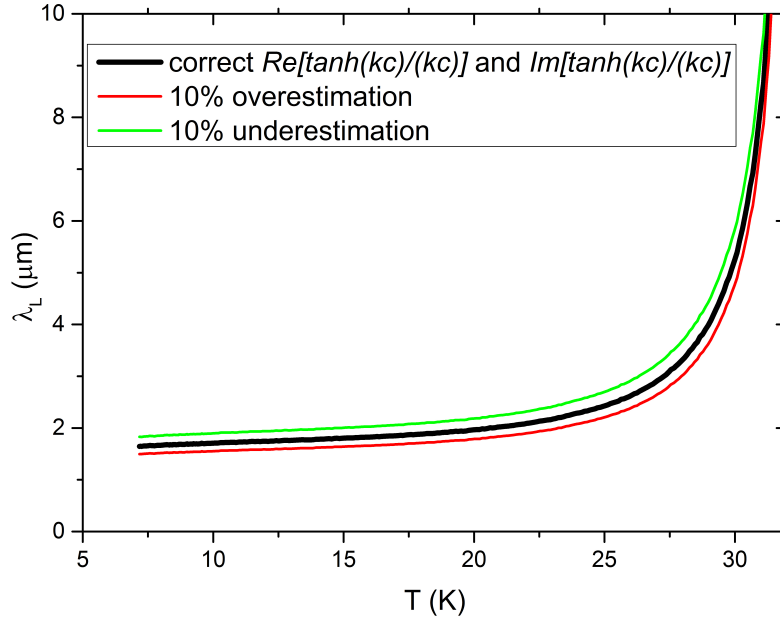


Figure 2.12: Modifications of $\lambda_L(T)$ produced by a 10% overestimation and underestimation of the real and imaginary part of $\tanh(kc)/kc$.

As stated in the beginning of this section, all the above mentioned sources of uncertainty affect the real and imaginary part of $\tanh(kc)/kc$. Their propagation is almost

straightforward, for example (as visible from Fig. 2.12), a $\pm 10\%$ uncertainty in the determination of the real and imaginary part of $\tanh(kc)/kc$ propagates to produce an uncertainty in the determination of the London penetration depth absolute value of $+11\%/-9\%$, whereas the temperature dependence of λ_L is affected in a negligible way. In the end, by adding up all the above discussed contributions and considering the way they propagate down to the determination of the London penetration depth, we generally obtain an uncertainty on λ_L between 5% and 10%.

Chapter 3

Ion irradiation and disorder

The study of the effects of disorder in superconducting materials can be carried out with two different approaches: chemical substitution and irradiation [106, 107]. The former consists in exchanging an atomic species of the material with a different one during the synthesis process. This results in a modification of the potential landscape with inhomogeneities at the impurity sites, and can give access to a large variety of scattering potentials (magnetic and non-magnetic) by employing different substituents. However, this approach suffers of several drawbacks: chemical substitution can also result in the introduction of extra charge (doping), not all substitutions are possible for all compounds and it is not possible to measure the same sample without the defects, so that interpretation is subject to the problem of sample to sample variability [27].

The latter approach makes use of the interaction of energetic particles (such as neutrons, photons, ions or electrons) with solid state matter. This interaction results in the displacement of atoms from their equilibrium position and therefore in the creation of defects. The morphology and distribution of defects (and hence their scattering potential) depends on the choice of projectile particle, energy and exposure time [107, 108]. Since defects are introduced in an already existing crystal, in this case it is possible to investigate the same sample with and without defects, as well as with increasing amount of defects. Moreover, the same defect typology can be introduced in any material allowing an easy comparison [109].

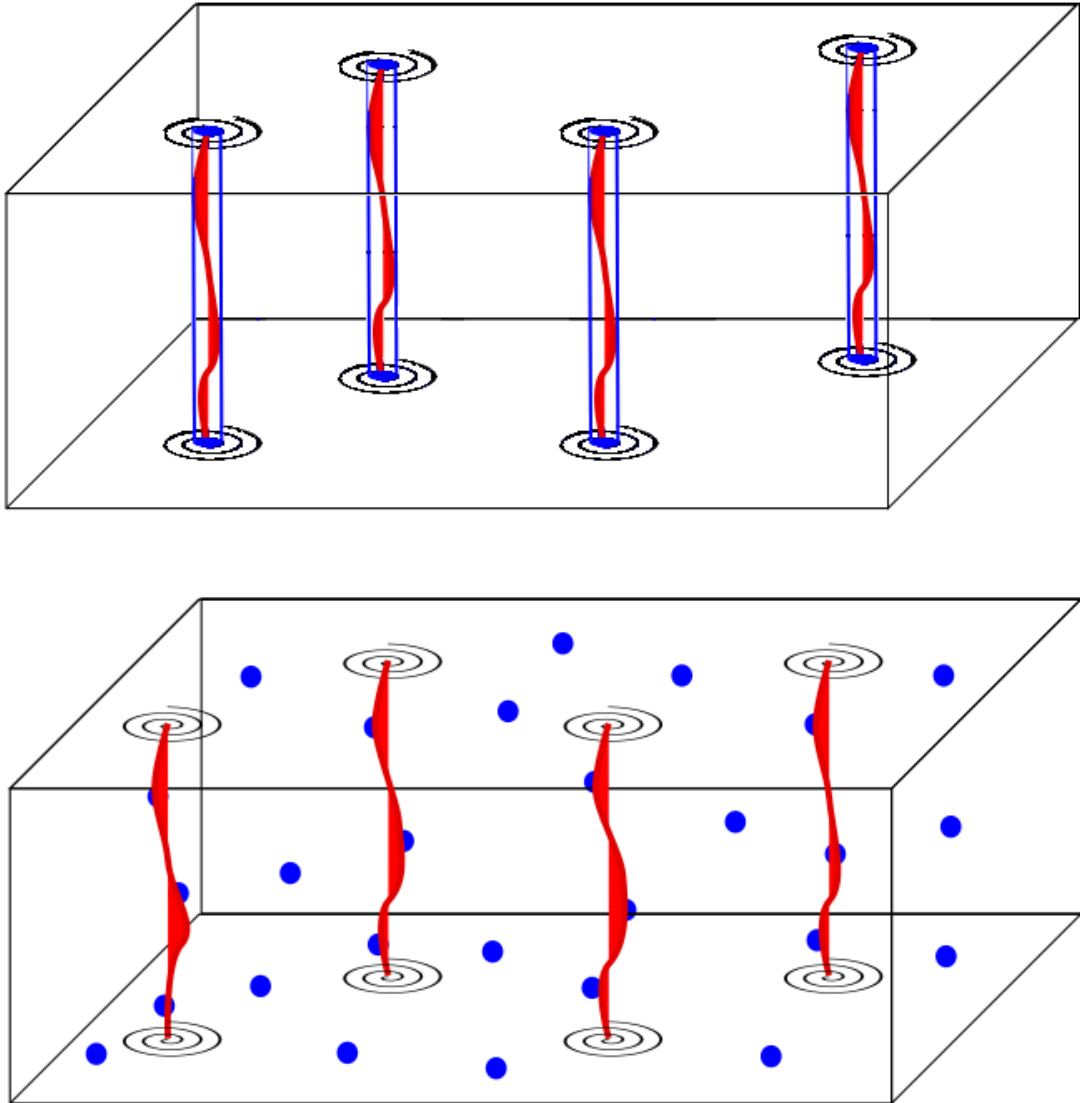


Figure 3.1: Sketch of vortex pinning by columnar defects on the top and randomly distributed point defects on the bottom (not on scale). Red lines represent core of the vortices and blue features the defective regions.

Although the word defect has commonly a negative connotation, in the field of superconductivity defects are often exploited to tune the properties of a material for specific applications [110]. Defects can act as pinning centers for vortices, limiting their motion and therefore suppressing dissipation and increasing the critical current j_c of a superconductor [111, 112]. High j_c values are a requirement for applications such as the

development of high field magnets for radiation harsh environments [113, 114]. Within this context ion irradiation has been greatly exploited because both columnar defects (whose symmetry matches that of fluxons) [115–117] and homogeneously distributed point defects [118] can be easily introduced with controllable densities. Apart from pinning vortices, defects also act as scattering centers for charge carriers [15, 23, 106, 119], and this is the role of defects that will be exploited in this thesis.

The effects of scattering centers in a multiband superconductor are much more complex than in single band materials: they decrease the critical temperature [120], shorten the quasiparticle lifetime [71], make the material more isotropic [121, 122], lift nodes in the gap [123, 124] and can even change the symmetry of the order parameter [24, 65, 125, 126]. For these reasons the study of disorder in IBSs is particularly interesting and relevant in their characterization.

3.1 Radiation damage

The interaction of energetic particles with matter results in what are known as a radiation damage events [127]. The term damage is used because the crystal structure of the sample is modified as a consequence of this interaction, creating disorder in the disposition of atoms [128]. These structural changes in turn influence the properties of the target material. Since only ion irradiation was used in this work, the description of radiation damage will be here limited to the case of charged particles, although also neutrons [107] and photons [129] can modify the structure of materials.

Charged particles can transfer energy to a sample mainly through two classes of processes: electronic and nuclear ones. In the former case, the projectile deposits energy in the target material by Coulomb interactions with the electronic system, this process is quantified by the electronic stopping power (S_e) and dominates for heavy particles with high energy. In the latter case the projectile undergoes collisions with the nuclei that compose the crystal lattice, a process that is predominant at low energies and is characterized by the nuclear energy loss S_n . When an atom is displaced from its lattice site with an energy that is sufficiently high, it can become itself a projectile for more collisions, creating a displacement cascade [130].

When the target materials is a superconductor, the most interesting typologies of defects are two: point defects and columnar defects. Continuous columnar defects are

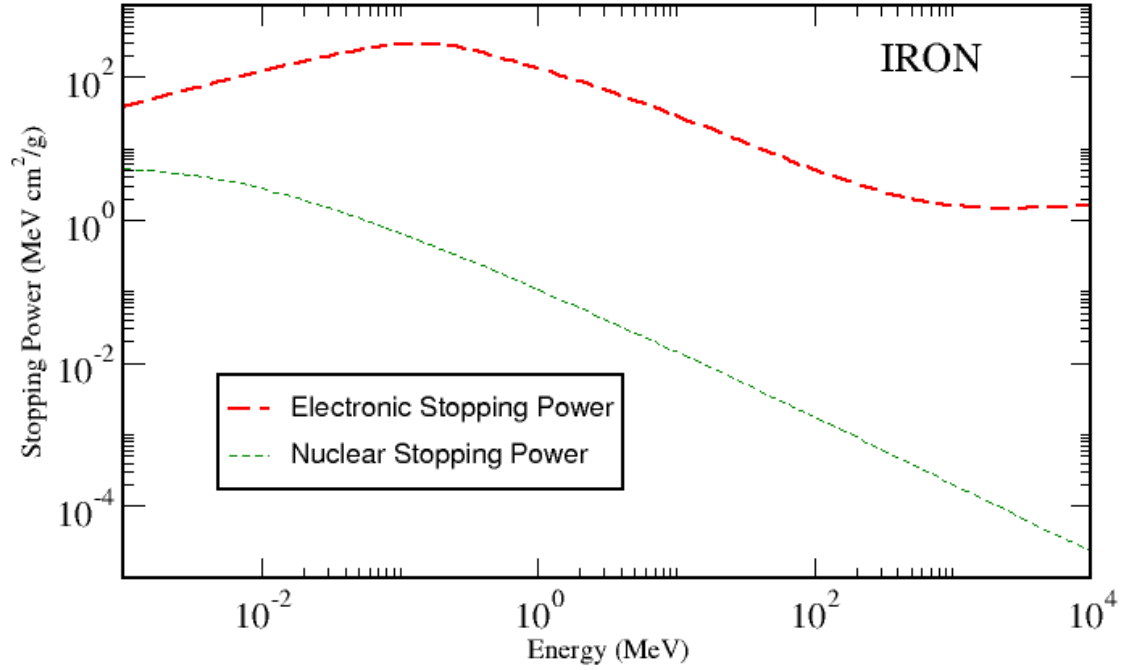


Figure 3.2: Electronic and nuclear stopping power of protons in iron calculated from the PSTAR database of the National Institute of Standards and Technology.

realized by high energy heavy ions if the electronic stopping power exceeds a certain threshold, about $30 \text{ MeV}/\mu\text{m}$ in the case of cuprates [107], above which local melting takes place. These tracks have a diameter of a few nanometers and their core can be an amorphous insulator for ceramic materials as the cuprates [131] or a disordered metal as in IBs [132]. Point defects, on the other hand, consist of isolated vacancies and interstitials (Frenkel pairs) and are generated most efficiently by electron irradiation [133], but also by every kind of ion irradiation where they are accompanied by more extended defects. Light ions such as H^+ in the MeV energy range create mostly point like isolated defects together with some small clusters [134]. It should be noted that, since the projectile loses energy along its trajectory, the type of defects created in a thick sample can vary on the front and back face of the sample. If the goal of the irradiation experiment is to introduce structural disorder in a sample without additional effects such as extra charge, it is important to avoid ion implantation (the stopping of an ion inside the sample after all its kinetic energy has been transferred to the material). This is achieved simply by performing the irradiation on a sample thinner than the implantation depth

of the employed ion (at the chosen energy) in the material as estimated by Monte Carlo simulations.

In this thesis three types of irradiation will be discussed: 3.5 MeV protons, 250 MeV Au ions and 1.2 GeV Pb ions. These cases span from the small, mainly point-like defects generated in the former case to the continuous columnar defects created in the latter, with the 250 MeV Au ions effects to be considered as intermediate: they produce defects that are linearly correlated along the ion track but discontinuous.

3.2 Particles accelerators



Figure 3.3: Pictures of the Tandem XTU accelerator and outgoing beam pipe on the left and of the tower of the CN accelerator on the right. Courtesy of Andrea Alessio.

All irradiation experiments were performed at the Laboratori Nazionali di Legnaro (LNL) of the Istituto Nazionale di Fisica Nucleare (INFN), where several particle accelerators are open to external users upon approval of a project and allocation of beam time [135]. Proton irradiation in the few MeV range can be carried out at the CN accelerator. This machine is a Van de Graaff electrostatic device [136] about 7 m tall, that can achieve an accelerating voltage of 7 MV. On top of the accelerating tower are situated the sources of ions that can be employed: protons, deuterium, helium and nitrogen. In

the experimental hall are present seven beam lines, one of which is dedicated to our group and is equipped with a collimator, a Faraday cup to collect the charge and thus allow to measure the beam current at the sample position, and a stage where IBSs single crystals can be mounted for homogeneous irradiation. The irradiation fluence is obtained with an ORTEC 996 counter that integrates the current read by an amperometer connected to the Faraday cup. The beam at the sample position has a circular spot of about 5 mm of diameter and its homogeneity is checked using a Mylar indicator before and after each irradiation session and a quartz scintillator glass inserted in the beam line several times during the process. Typically we perform 3.5 MeV proton irradiation in high vacuum, at room temperature, keeping the beam current below ≈ 25 nA to avoid heating of the sample, for a duration of several hours in order to achieve an ion fluence of the order of 10^{16} cm⁻², necessary to induce appreciable changes in the materials properties [126]. Several small samples can be mounted together on the same sample holder on double sided adhesive kapton tape.

Heavier ions can be accelerated with the Tandem XTU machine up to few hundreds of MeV. In this case the high voltage terminal is at the center of a horizontal tank, the projectile ions enter with a weakly negative charge on one side of the tank and are attracted, gaining kinetic energy, by the terminal that can reach 14.5 MV. Here, in a region screened from electrostatic fields, the ions pass through a thin carbon film that strips them of many electrons [137] (the total charge acquired depends on the ion and energy but is of the order of 10-20 e). When they exit the terminal, they are subject to a repulsive electrostatic force that increases again their kinetic energy until they exit from the opposite side of the tank. This types of machines are called tandem because the ions are accelerated in two stages. With the Tandem XTU accelerator we performed the 250 MeV Au ions irradiation. An important limitation of tandem machines is the use of strippers that is not compatible with the reaching of particularly high energies with heavy ions such as Pb. To accelerate such ions at high energies the Piave-Alpi facility is therefore necessary.

Piave is an injector and needs a second accelerator (Alpi) to provide a beam in the experimental hall. Piave works with an electron cyclotron resonance ion source [138] that produces directly highly positively charged particles without the need of using a stripper foil. The source is positioned at a high voltage (up to 400 kV) platform that gives a first acceleration to the ions that then undergo a second acceleration step provided by a set of superconducting radio frequency quadrupole accelerating structures [139, 140]. At



Figure 3.4: Picture of the group's beamline at the Tandem XTU and Piave-Alpi facility.

this point the ions are fast enough to enter the Alpi accelerator, where the final particle energy is obtained by several sets of quarter wave superconducting resonator cavities [141] operating at 80 and 160 MHz frequencies. With this setup we performed the 1.2 GeV Pb ion irradiation.

Both Tandem XTU and Piave-Alpi (actually it is also possible to couple Tandem XTU with Alpi) provide the ion beam in the same experimental hall where our group has another dedicated beam line. Also in this case the end of the beam line is equipped with a Faraday cup to measure the beam current at the sample position. For energetic heavy ions that produce continuous or discontinuous columnar tracks it is usually sufficient to work with fluences of the order of 10^{12} cm^{-2} [72].

3.3 Monte Carlo simulations

To ensure that no ion implantation occurs and to estimate the amount of defects created in a specific sample, Monte Carlo simulations can be a great aid to the experiment design. Many pre-compiled codes exist that allow to obtain this kind of information, each with different features and advantages. The most commonly employed is SRIM

[142], mostly due to its simplicity of use, the fact that it is well benchmarked by the developers [130] and that most results in literature are obtained with it, allowing a quick comparison of data. This code can be used to obtain the implantation depth and the distribution of vacancies and interstitials along the direction of the beam inside the sample. Unfortunately it does not allow to simulate complex geometries, so its uses are somehow limited to simple systems such as single crystals and bulks. If a precise control of the geometry is needed (e.g. when considering layered or patterned systems) other codes based on the same approach, but equipped with a CAD assisted (or similar) design of three dimensional experimental setups, such as PHITS [143], are more convenient. These codes consider the target material as an amorphous mixture of atoms, disregarding effects of the crystal structure such as channeling. However, these effects are relevant only in specific cases in which the relative orientation between the beam and the crystallographic axes of the crystal is carefully selected [144]. The most important parameters that are fed to the code are the density and composition of the target material, the nature and energy of the projectile particles and the dimensions of the target. Monte Carlo simulations are always performed with a number of simulated particles high enough to ensure the statistical validity of the results. All simulations performed in this thesis were carried out using the Kinchin-Pease approach [145] for the evaluation of radiation damage in terms of displacement per atom (dpa) and assuming a displacement energy of 25 eV for all target atoms. The displacement energy is the minimum energy needed to remove an atom from its equilibrium position in a permanent way. 25 eV is the generic reference value for atoms in a solid, and its use is justified if the dpa values obtained are used for comparison between similar systems [146]. The Kinchin-Pease approach is an approximated analytical model that allows to obtain a quick evaluation of the total dpa produced in a cascade initiated by the projectile particle, by estimating the knock out energy of the first atom and disregarding the spatial distribution of the cascade. This procedure yields a reasonable estimate, unless a precision of the order of the cascade size is needed in the spatial distribution of dpa, with a great reduction of computational times [142].

In Fig. 3.5, the typical outcome of a Monte Carlo simulation, needed to set up the details of the irradiation experiment, is shown. In this case the code SRIM [142] was employed on a target of $\text{BaFe}_{1.864}\text{Rh}_{0.068}\text{As}_2$ material with 3.5 MeV protons as projectiles [126]. The normalized dpa profile as a function of depth inside the material is obtained

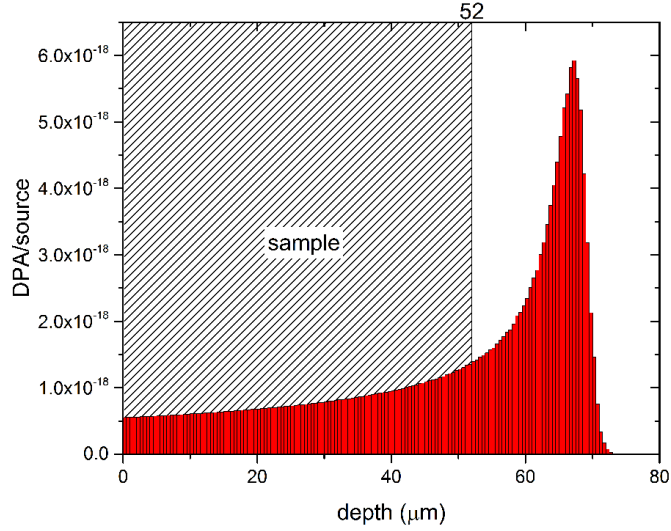


Figure 3.5: SRIM [142] calculation for the displacement per atom (dpa) as a function of depth inside the crystal for 3.5-MeV protons impinging on $\text{BaFe}_{1.864}\text{Rh}_{0.068}\text{As}_2$. The shaded area represents the thickness of a sample.

and the peak corresponds to the implantation depth of the ions. In this case, to avoid implantation, it is necessary to work on samples thinner than $60 \mu\text{m}$. For a sample thick $52 \mu\text{m}$ the average damage introduced can be estimated as the average over the first $52 \mu\text{m}$ of this curve multiplied by the total number of ions to which the sample was exposed during the irradiation process. In the case of thick samples it is important to reduce the uneven distribution of defects along the thickness by flipping front and back faces during long irradiations or between successive irradiation runs.

3.4 Defects as scattering centers

In this work, structural disorder is exploited to provide scattering centers for charge carriers. The most efficient type of defects for this goal are small ones, whereas larger defects are less efficient scatterers [107]. This is due to the transferred momentum that is larger for smaller defects and results mainly in interband scattering instead of intraband scattering. The effects of scattering on the properties of a superconductor depend on the

specific system, and in particular on the symmetry of its order parameter and on the number of bands [15, 106]. For conventional low temperature superconductors, the well known Anderson theorem states that their T_c , order parameter and superfluid density are not influenced by nonmagnetic scattering [147]. Magnetic impurities instead are effective in decreasing the critical temperature [148].

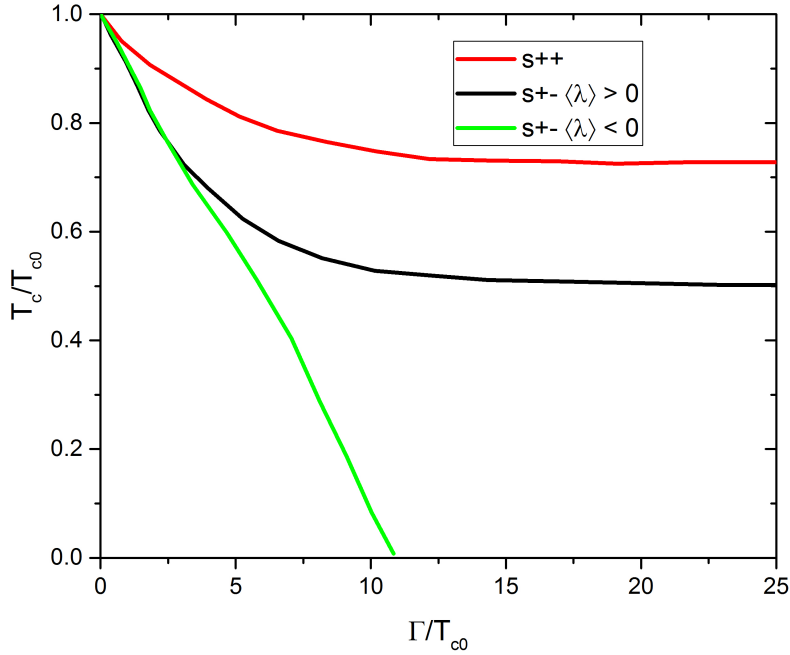


Figure 3.6: Expected decrease of critical temperature with increasing interband scattering for different order parameter symmetries and coupling details proposed for IBSs. Data extracted from [106].

Conversely, after their discovery it was quickly realized that the cuprates are extremely sensitive to the presence of disorder[108]. This results from the fact that non-magnetic scattering of a Cooper pair is pairbreaking if the two points of the FS connected by the event have an order parameter with opposite signs [106]. This is true for different regions of the d-wave symmetry that characterizes cuprates, whereas in conventional systems all regions of the FS have the same sign. This also holds for IBSs with the different gaps characterized by opposite signs of the order parameter. It should be noted that the very opposite is true for magnetic scattering: it is pairbreaking on regions of the FS that have the same sign and ineffective on regions with opposite sign [106].

An additional complication arises from the multigap nature of IBSs: the effect of scattering on the gaps is to average their values [15, 106], driving them to converge to the same value. For this reason, also the s_{++} order parameter is influenced by scattering, although the rate of decrease of the critical temperature is expected to be smaller than for the s_{\pm} case and, more importantly, must completely flatten at the reaching of gap convergence where the system becomes equivalent to a conventional single gap one (see Fig. 3.6) [106].

In the case of the s_{\pm} state, a transition to the s_{++} one was predicted [23, 24, 65] with increasing nonmagnetic scattering because the two gaps need to have the same sign before reaching value convergence.

Additional effects relevant to some IBSs are related to the presence of accidental nodes in the gap. It has been shown that nonmagnetic scattering, through the above mentioned averaging process can lift the nodes recovering a fully gapped system [123, 124, 149].

Chapter 4

Theoretical model

In order to gain a deeper insight in the physics of IBSs, in this thesis measurements are accompanied by calculations that aim to reproduce the experimental data and yield additional information on the order parameter and on the coupling matrix. In the following chapter the choice of theoretical approach based on the solution of the Eliashberg equations is justified, the procedure employed to relate to the experiment is explained and the information extracted are discussed. Parts of these topics were published in Ref.s [72, 73, 126]

4.1 The Eliashberg approach

As discussed in the introduction, the most likely interaction mechanism for superconductivity in IBSs is that of antiferromagnetic spin fluctuations [12] whilst phonons alone are too weak to be responsible for the observed properties [12, 52–54]. In addition, multiple bands are present [47–49] so that several gaps open on the Fermi surfaces [40–43]. From these facts it is evident that BCS theory can not be employed to evaluate the superconducting properties of these materials: it has been shown that multiband superconductivity is incorrectly described by the BCS theory even in the weak coupling limit and that, to be employed for IBSs, it would need to be renormalized with a procedure that makes use of the Eliashberg equations [150].

An extension of BCS theory that can be applied to strong coupling, multiband, non phononic systems, is the Migdal-Eliashberg formalism [151]. The essence of Migdal's theorem is that, to go beyond the weak coupling approximation of BCS theory, it is

sufficient to consider only one vertex correction Feynman graph that gives the single boson scattering term contribution to the electronic self-energy [152]. This stems from the adiabatic approximation, in which the electronic subsystem is considered not to be sensitive to the time dependence of the ionic lattice.

Eliashberg theory, in addition, generalizes BCS theory to incorporate the Migdal theorem and time-dependent electron-boson interaction [153]. Therefore, differently from BCS theory, the electron-boson coupling in the Eliashberg theory can be retarded in time, local in space and not necessarily weak.

Since it is based on Migdal’s theorem, Eliashberg theory has the same validity constraints: it is necessary that $\Lambda\Omega_0/E_F \ll 1$, where Λ is the coupling constant and Ω_0 is the characteristic frequency of the boson that mediates the interaction (e.g. for the case of phonons it would be the Debye frequency ω_D) [154, 155]. For the specific case of IBSs, electron boson coupling (whose value is close to 1) is provided by spin fluctuations that, in the superconducting state, are characterized by a spectral function that has the shape of a Lorentzian function [156] peaked at a frequency Ω_0 . This characteristic frequency is found to follow the phenomenological law Ω_0 (meV) = $2T_c(K)/5$ [25]. For the systems studied in this thesis T_c ranges from about 20 K to less than 40 K, therefore Ω_0 is in all cases smaller than 16 meV. The Fermi level of IBSs instead is at least of the order of 100–200 meV [157–159]. It results that the two energy scales (Ω_0 and E_F) are not separated by several orders of magnitude as it happens in simpler systems, but still the regime considered is such that the approximation on which Migdal’s theorem is based holds, and therefore the Eliashberg theory is applicable [160].

The Eliashberg approach consists in writing the Green functions matrix for electrons and bosons in the Migdal approximation. This yields a system of equations for the components of the self-energy that can be solved self consistently to obtain the values of the order parameter and renormalization function [161]. In the weak coupling limit the renormalization function goes to 1 and a non renormalized limit is retrieved (this limit coincides with BCS if the pairing interaction has the same characteristics as the BCS one, which is not the case for IBSs [150]).

The so obtained Eliashberg equations are still extremely complex to solve since all momenta \mathbf{k} appear explicitly. To simplify the calculations and turn the Eliashberg equations in a tool that can be useful as a support for experiments, one can try to eliminate the momentum dependence [152]. Fortunately, in the case of IBSs the gaps are very weakly anisotropic [162], this means that also the interaction can be reasonably

considered momentum independent on each Fermi sheet. Therefore it is possible to substitute the \mathbf{k} -dependent order parameter and renormalization function with an average value for each Fermi sheet considered in the model. With this approach the Eliashberg equations become a set of $2N$ equations for the N \mathbf{k} -averaged order parameters and renormalization functions, where N is the number of bands in the model [72, 73, 82, 126].

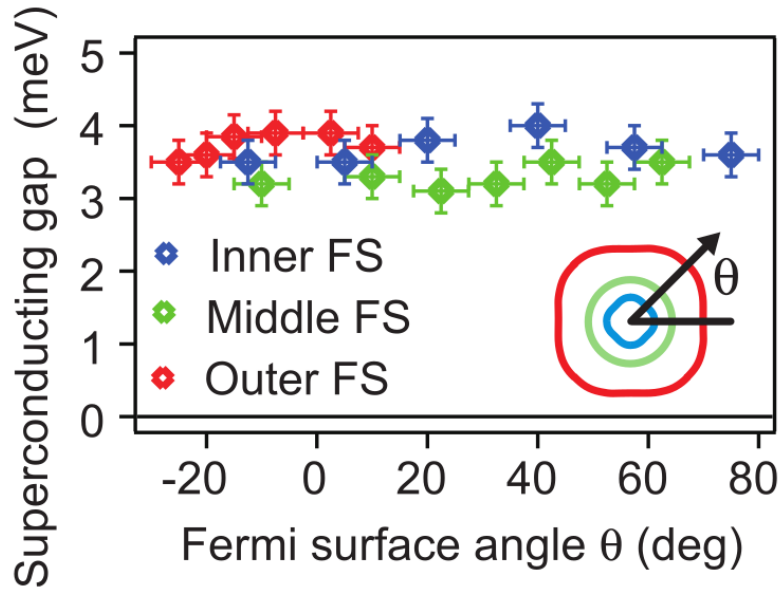


Figure 4.1: Angular dependence of the gap values on different Fermi surfaces from ARPES measurements for P doped $\text{BaFe}_{1-x}\text{As}_2$. Adapted from [163]. ©2011, American Association for the Advancement of Science.

The weak anisotropy of the gaps has been observed by Angle Resolved Photoemission Spectroscopy (ARPES) measurements by several groups on many IBSs systems [40, 41, 162, 163] (see Fig. 4.1 for an example). Although in some cases significant differences in the size of the gap amplitude for different Fermi surface sheets have been observed by different groups, there seems to be a consensus between most measurements that the value on an individual Fermi sheet is weakly dependent on the direction. It is important to note that this is only an indirect information about the momentum dependence of the interaction itself, but indeed supports the choice of using the averaged value of the interaction over the momentum. In fact, it has been shown that in general the interaction

can be expanded in spherical harmonics, only some of which are relevant in any specific case (usually the s-symmetric one). If one needs to consider a momentum dependent interaction, will have to keep higher harmonics with their characteristic angular dependency. This specific angular dependency would then be reflected in the calculated quantities, such as the order parameter, that would result to be anisotropic [152].

4.2 Eliashberg equations and input parameters

With the approach described in the previous section, the Eliashberg equations can be written, on the imaginary axis, as [106, 153, 164]:

$$\begin{aligned} \omega_n Z_i(i\omega_n) = & \omega_n + \pi T \sum_{m,j} \Lambda_{ij}^Z(i\omega_n, i\omega_m) \frac{\omega_m}{\sqrt{\omega_m^2 + \Delta_j^2(i\omega_m)}} \\ & + \sum_j \Gamma_{ij}^N \frac{\omega_m}{\sqrt{\omega_m^2 + \Delta_j^2(i\omega_m)}} \end{aligned} \quad (4.1)$$

$$\begin{aligned} Z_i(i\omega_n) \Delta_i(i\omega_n) = & \pi T \sum_{m,j} [\Lambda_{ij}^\Delta(i\omega_n, i\omega_m) - \mu_{ij}^*(\omega_c)] \times \Theta(\omega_c - |\omega_m|) \frac{\Delta_j(i\omega_m)}{\sqrt{\omega_m^2 + \Delta_j^2(i\omega_m)}} \\ & + \sum_j \Gamma_{ij}^N \frac{\Delta_j(i\omega_m)}{\sqrt{\omega_m^2 + \Delta_j^2(i\omega_m)}}, \end{aligned} \quad (4.2)$$

where Θ is the Heaviside function, ω_c is a cutoff energy needed for the numerical solution of the equations, $\Delta_i(i\omega_n)$ and $Z_i(i\omega_n)$ are respectively the frequency dependent order parameter and renormalization function on the i^{th} band, ω_n is the n^{th} Matsubara frequency, $\Lambda_{ij}^Z(i\omega_n, i\omega_m) = \Lambda_{ij}^{ph}(i\omega_n, i\omega_m) + \Lambda_{ij}^{sf}(i\omega_n, i\omega_m)$, $\Lambda_{ij}^\Delta(i\omega_n, i\omega_m) = \Lambda_{ij}^{ph}(i\omega_n, i\omega_m) - \Lambda_{ij}^{sf}(i\omega_n, i\omega_m)$, are the frequency dependent coupling matrix elements that are, in principle, composed by phononic (ph) and a spin fluctuation (sf) contributions [82]. Their frequency dependence can be expressed as follow:

$$\Lambda_{ij}^{ph,sf}(i\omega_n, i\omega_m) = 2 \int_0^{+\infty} d\Omega \Omega \alpha_{ij}^2 F^{ph,sf}(\Omega) / [(\omega_n - \omega_m)^2 + \Omega^2], \quad (4.3)$$

where $\alpha_{ij}^2 F^{ph,sf}(\Omega)$ are the spectral functions for phonons and spin fluctuations. For the case of IBSs, we neglect the phononic contributions [26, 164–166] and considered a Lorentzian shape for the spectral function of spin fluctuations in the superconducting state:

$$\alpha_{ij}^2 F^{sf}(\Omega) = C_{ij} \left\{ \frac{1}{(\Omega + \Omega_{ij})^2 + Y_{ij}^2} - \frac{1}{(\Omega - \Omega_{ij})^2 + Y_{ij}^2} \right\}.$$

Here C_{ij} are normalization constants necessary to obtain the proper values of the coupling constants, Ω_{ij} and Y_{ij} are the peak energies and the half-widths of the Lorentzian functions. Based on the results of inelastic neutron scattering measurements [156], we set $\Omega_{ij} = \Omega_0$ and $Y_{ij} = \Omega_0/2$, where the characteristic frequency of the AFM SF Ω_0 is the one discussed previously: Ω_0 (meV) = $2T_c(K)/5$ [25]. It should be noted that the spectral function used is different from the analytical expression in the normal state ($\alpha_{ij}^2 F^{sf}(\Omega) = B_{ij} \Omega \Omega_{ij} \Theta(\Omega_{max} - \Omega) / (\Omega^2 + \Omega_{ij}^2)$ [167]) that was shown to be modified in the superconducting state yielding a narrower peak [156] (an example is given in Fig. 4.2).

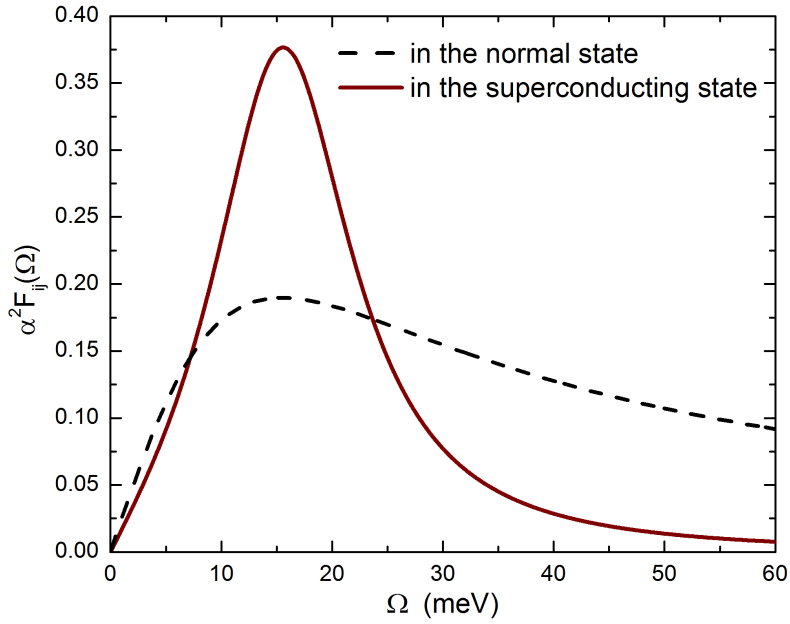


Figure 4.2: Spectral function for spin fluctuations in the normal (dashed black line) and superconducting (solid red line) state for the K-doped BaFe_sAs_2 system. Adapted from [73]. ©2019 American Physical Society.

The remaining terms in Eqs. 4.1 and 4.2 are the Morel-Anderson coulombian pseudopotential matrix elements μ_{ij}^* , that can be set to zero because in IBSs are small and tend to compensate the small phononic contributions to the coupling [15, 164–166], and the scattering rates from non-magnetic impurities Γ_{ij}^N .

By analytical continuation of the Green’s functions, the Eliashberg equations can be also written on the real frequencies axis [168]:

$$\begin{aligned} \Delta_i(\omega, T)Z_i(\omega, T) &= \int_0^{\omega_c} d\omega' \Re \left(\frac{\Delta_i(\omega', T)}{\sqrt{\omega'^2 - \Delta_i^2(\omega', T)}} \right) \sum_j \left\{ \int_0^\infty d\Omega \alpha_{ij}^2 F^{sf}(\Omega) \right. \\ &\quad \times \left[(n(\Omega) + f(-\omega')) \left(\frac{1}{\omega + \omega' + \Omega + i\delta^+} - \frac{1}{\omega - \omega' - \Omega + i\delta^+} \right) \right. \\ &\quad \left. \left. - (n(\Omega) + f(\omega')) \left(\frac{1}{\omega - \omega' + \Omega + i\delta^+} - \frac{1}{\omega + \omega' - \Omega + i\delta^+} \right) \right] \right\} \\ &\quad + \sum_j \Gamma_{ij}^N \left(\frac{\Delta_j(\omega, T)}{\sqrt{\omega^2 - \Delta_j^2(\omega, T)}} \right), \end{aligned} \quad (4.4)$$

$$\begin{aligned} [1 - Z_i(\omega, T)] \omega &= \int_0^\infty d\omega' \Re \left(\frac{\omega'}{\sqrt{\omega'^2 - \Delta_i^2(\omega', T)}} \right) \sum_j \left\{ \int_0^\infty d\Omega \alpha_{ij}^2 F^{sf}(\Omega) \right. \\ &\quad \times \left[(n(\Omega) + f(-\omega')) \left(\frac{1}{\omega + \omega' + \Omega + i\delta^+} - \frac{1}{\omega - \omega' - \Omega + i\delta^+} \right) \right. \\ &\quad \left. \left. - (n(\Omega) + f(\omega')) \left(\frac{1}{\omega - \omega' + \Omega + i\delta^+} - \frac{1}{\omega + \omega' - \Omega + i\delta^+} \right) \right] \right\} \\ &\quad + \sum_j \Gamma_{ij}^N \left(\frac{\omega}{\sqrt{\omega^2 - \Delta_j^2(\omega, T)}} \right). \end{aligned} \quad (4.5)$$

Here the Morel-Anderson coulombian pseudopotential matrix and the phonic contribution to coupling have already been set to zero for simplicity, $f(\omega) = 1/(e^{\beta\omega} + 1)$ is the Fermi distribution function while $n(\omega) = 1/(e^{\beta\omega} - 1)$ is the Bose distribution function. The principal-value integrals in (4.4) and (4.5) determines the real part of $\Delta(\omega, T)Z(\omega, T)$ and of $Z(\omega, T)$, while the imaginary part comes from the delta-function terms. It is important to note that the denominators can vanish for particular values of the energy, therefore the integrals in (4.4) and (4.5) must be treated carefully when a

numerical approach is used.

These two alternative version of the Eliashberg equations are completely equivalent to each other [161], but each one can be more or less convenient to calculate observable quantities: from the former version it is possible to evaluate the London penetration depth [169], whereas the latter is suitable to obtain the quasiparticle conductivity [170]. Both sets of equations need the same input (free) parameters that, considering all the approximations discussed so far and an N -bands model, consist on the $N \times N$ coupling constant matrix and the $N \times N$ scattering rates matrix. Fortunately, not all entries of these matrices are non-zero as a consequence of the nature of IBSs [82]. The coupling matrix has negligible diagonal components if the system is modelled with all the physically relevant (at least three for most systems) bands. This is a consequence of the fact that spin fluctuations only couple separated Fermi surfaces (interband) and that phonons can be neglected (intraband contributions) [15, 26]. Moreover, also off-diagonal elements that refer to bands with the same character (hole-hole or electron-electron) will be zero due to the fact that their Fermi surfaces are too close to each other to be coupled by AFM SF (and, as a result they do not have opposite sign of the order parameter).

Conversely, if a simplified two-band approach is employed, also intraband coupling must be included, keeping in mind that all intraband contributions represent a combination of interband terms of a more realistic model that involves all the existing bands [55, 126]. In addition, symmetric contributions such as Λ_{ij} and Λ_{ji} are related to each other through the ratio of the density of states on the two bands ($v_{ij} = N_i(0)/N_j(0)$ where $N_i(0)$ is the normal density of states at the Fermi level for the i -th band) that can be estimated from the size of the Fermi surfaces $k_{F,i}$ and $k_{F,j}$ [82, 171]. The resulting coupling matrices for the two and three band model are the following:

$$\Lambda_{ij} = \begin{pmatrix} 0 & 0 & \Lambda_{13}^{sf} \\ 0 & 0 & \Lambda_{23}^{sf} \\ \Lambda_{31}^{sf} = \Lambda_{13}^{sf} v_{13} & \Lambda_{32}^{sf} = \Lambda_{23}^{sf} v_{23} & 0 \end{pmatrix} \quad (4.6)$$

$$\Lambda_{ij} = \begin{pmatrix} \Lambda_{11}^{sf} & \Lambda_{12}^{sf} \\ \Lambda_{12}^{sf} v_{12} & \Lambda_{22}^{sf} \end{pmatrix} \quad (4.7)$$

Regarding the scattering rate matrix, if only nonmagnetic scattering is considered (as relevant for this study), again the only pairbreaking contributions come from interband

scattering and all diagonal elements can be set to zero [106].

Disorder can be treated with two different approaches: if the level of disorder is at most moderate, the Born approximation can be employed [72], otherwise the T-matrix approach is needed [126]. The Born approximation only describes the global effect of disorder and not the details of the defects [152]. In the T-matrix approach instead it is possible to range from the Born approximation to the unitary limit of strong scattering and to consider both interband and intraband scattering [24, 106, 172]. Therefore the scattering terms can be written as

$$\Gamma_{ij}^N = \frac{\Gamma_i(1 - \sigma)}{\sigma(1 - \sigma)\eta[N_i(0) + N_j(0)]^2/[N_i(0)N_j(0)] + (\sigma\eta - 1)^2}, \quad (4.8)$$

where the generalized cross-section and normal state scattering rate are respectively $\sigma = \pi^2 N_i(0)N_j(0)u^2/(1 + \pi^2 N_i(0)N_j(0)u^2)$, $\Gamma_i = n_{imp}\pi N_j(0)u^2(1 - \sigma)$ and n_{imp} is the impurity concentration. η instead controls the ratio of intra to inter-band scattering: $v^2 = u^2\eta$, where v and u are the intraband and interband impurity potentials. The Born limit is achieved for $\sigma \rightarrow 0$, while for $\sigma \rightarrow 1$ the unitary limit is found. This disorder term is obtained from the more general equations 42 and 43 in [106] for $\eta = 1$.

The difference lies in the fact that we assume the factorizability of the Γ_{ij}^N and $N_j^\Delta(i\omega_n)$ terms, that is equivalent to say that there is no frequency dependence of the disorder induced scattering. The two expressions are exactly equivalent if $N_1^Z N_2^Z + N_1^\Delta N_2^\Delta \simeq 1$, as it is verified in all the cases discussed in this work [173]. If the focus of an experiment is on the material and only low levels of disorder are introduced, the most appropriate way to model the IBS is a three-band model with disorder treated in the Born limit, whereas if the focus is on the effects of high levels of disorder then it is needed to employ the T-matrix approach and to consider a simplified two bands model in order to keep reasonable the number of free parameters to be fixed.

4.3 Calculated quantities

The Eliashberg equations (both on the imaginary and real axis) can be solved self consistently for the order parameters and renormalization functions at all temperatures. From these quantities calculated on the imaginary axis ($\Delta_i(i\omega_n)$ and $Z_i(i\omega_n)$), it

is possible to compute the London penetration depth as [169]:

$$\lambda_L^{-2}(T) = \left(\frac{\omega_p}{c}\right)^2 \sum_{i=1}^3 w_i^\lambda \pi T \times \sum_{n=-\infty}^{+\infty} \frac{\Delta_i^2(\omega_n) Z_i^2(\omega_n)}{[\omega_n^2 Z_i^2(\omega_n) + \Delta_i^2(\omega_n) Z_i^2(\omega_n)]^{3/2}} \quad (4.9)$$

Here $w_i^\lambda = (\omega_{p,i}/\omega_p)^2$ are the weighting factors that determine how much each band contributes to the total observable value. They depend on the plasma frequency of each band $\omega_{p,i}$ normalized to the total plasma frequency ω_p . Since these quantities are unknown for most materials, the weights w_i^λ are considered as free parameter that can be tuned in order to reproduce at best the experimental $\lambda_L(T)$. They must obey the constraint $\sum_i w_i^\lambda = 1$.

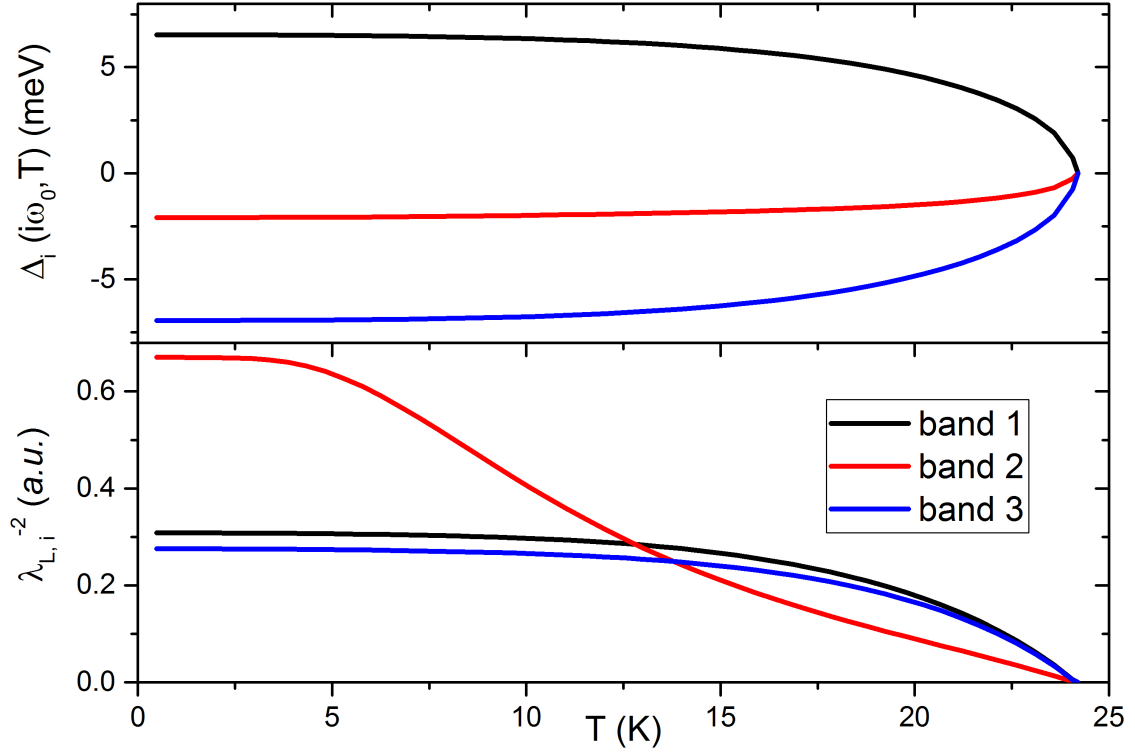


Figure 4.3: Temperature dependence of the gaps (upper graph) and of the single band contributions to the total superfluid density for optimally Co-doped BaFe₂As₂.

It should be noted that the multiplicative factor involving the plasma frequency comes from the relation $\omega_p = c/\lambda_L(0)$ that is strictly valid only at $T = 0$, for a clean

uniform superconductor and if Fermi-liquid effects such as strong coupling ones are negligible [106] (this point will be discussed further in Chapter 5).

Eq. 4.9, consists of a sum of single band contributions (shown in Fig. 4.3 for an optimally Co-doped BaFe₂As₂ sample together with the temperature dependence of the corresponding gaps) without any cross terms. Such terms would represent contributions to the total superfluid density (that is proportional to λ_L^{-2}) from Cooper pairs composed of electrons located on different Fermi surfaces (and therefore located at very different k points) that have a negligible probability of formation.

From the self consistent solution of the real axis version of the Eliashberg equations ($\Delta_i(\omega)$ and $Z_i(\omega)$) it is possible to determine the microwave conductivity [170]:

$$\begin{aligned} \sigma_1(\omega \rightarrow 0) &= \sum_i w_i^\sigma \sigma_{1,i} = & (4.10) \\ &= \sum_i w_i^\sigma A_i \times \int_0^{+\infty} d\omega \left(-\frac{\partial f(\omega)}{\partial \omega} \right) [(\text{Re } g_i^Z(\omega))^2 + (\text{Re } g_i^\Delta(\omega))^2] \end{aligned}$$

where $A_i = N_i(0)v_F^2 e^2 \tau_i(T)$, $N_i(0)$ are the density of states on each band (often unknown, therefore the A_i terms are basically composed of a scale factor multiplied by the scattering time), $\tau_i(T)$ are the temperature dependent quasiparticle scattering times, w_i^σ are the weights of each band, and

$$\begin{aligned} g_i^Z(\omega) &= Z_i(\omega)\omega / \sqrt{[Z_i(\omega)\omega]^2 - [\Delta_i^2(\omega)Z_i^2(\omega)]} \\ g_i^\Delta(\omega) &= \Delta_i(\omega)Z_i(\omega) / \sqrt{[Z_i(\omega)\omega]^2 - [\Delta_i^2(\omega)Z_i^2(\omega)]} \end{aligned}$$

An effective scattering time can be estimated with a phenomenological modified two-fluid model [71, 174] and, assuming that τ_i follows the same temperature behavior for all bands and that all scale factors are equal ($A_i = A$), the mixing weights in Eq.4.10 are left as the only free parameters available to reproduce the experimental data. These weights are subject to the same constraints as the ones for the London penetration depth $\sum_i w_i^\sigma = 1$.

The solution of the Real and imaginary axis Eliashberg equations are presented in Fig. 4.4 for the optimally K-doped BaFe_sAs₂ as a comparison between the two sets of obtained quantities.

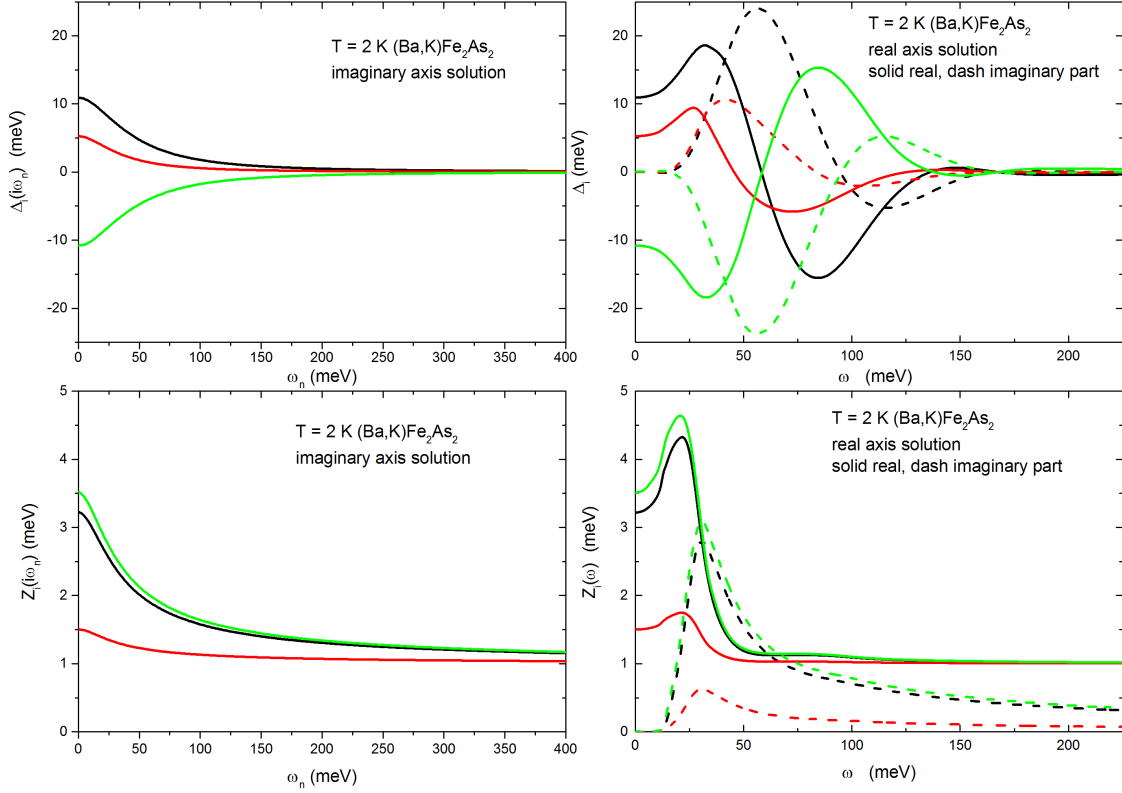


Figure 4.4: Order parameters (upper half) and renormalization functions (lower half) on each band calculated from for the K-doped BaFe_sAs_2 system at $T = 2$ K on the imaginary (left side) and real axis (right side). Adapted from [73]. ©2019 American Physical Society.

4.4 Fitting procedure

In this last section, the procedure employed to fix the free parameters left in the model (the coupling constant matrix, the scattering rates, the mixing weights and the plasma frequency) is explained.

As already mentioned, in order to investigate the effects of disorder one has always to characterize a pristine sample first: let us start the discussion from this case. All the samples examined in this thesis are high quality single crystals (as indicated by their narrow superconducting transitions) for which intrinsic disorder can be considered negligible [82], especially if compared to the levels introduced by ion irradiation [72, 126]. For this reason all the scattering rates Γ_{ij} are set to zero in the analysis of pristine samples. The remaining parameters needed to solve the Eliashberg equations are the non zero

independent elements of the coupling constant matrix (three parameters both for the two band and three band models) that are fixed with the following procedure.

- A set of Λ_{ij} is chosen, the imaginary axis Eliashberg equations are solved self consistently at a temperature T coincident with the experimental T_c . This step is repeated adjusting the set of Λ_{ij} until the order parameters converge to zero.
- The equations are also solved at low temperature to check if the gap values agree well with those reported in literature measured by ARPES. If the agreement is not good, a different combination of coupling constants is chosen starting from the previous step.
- The imaginary axis Eliashberg equations are solved for finely spaced temperatures up to T_c and the obtained gaps and renormalization functions are employed to calculate the London penetration depth and the superfluid density (that does not depend on the plasma frequency). The w_i^λ weights are adjusted so that this value agrees well with the experimentally determined one. If $\rho_s(T)$ does not agree well with the experimental data, the coupling constants are varied a little going back to the first step.
- Also the $\lambda_L(T)$ calculated curve is compared to the experimental one and the plasma frequency is fixed.

The coupling constants determined by fitting the superfluid density are then used also in the real axis Eliashberg equations to obtain the $\Delta(\omega, T)$ and $Z(\omega, T)$ necessary to calculate the $\sigma_{1,i}$ terms in Eq. 4.10. As discussed in the previous section, in order to fit the quasiparticle conductivity the scattering time must be estimated. The role of inelastic scattering in IBSs can be studied with a two fluid model [174] that, despite its simplicity, gives a good insight in the properties of these materials. Furthermore, the scattering time τ_{TF} employed in the model can be related to the quantities measured with our experimental technique: Z_s , λ_L and σ_n [71].

Since the surface impedance in general can be written as $Z_s = R_s + iX_s = \sqrt{i\mu_0\omega/(\sigma_1 - i\sigma_2)}$ (where $\sigma_1 \equiv \sigma_n$), the conductivity can be expressed as:

$$\begin{aligned}\sigma_1 &= 2\omega\mu_0 \frac{R_s X_s}{(R_s^2 + X_s^2)^2} \\ \sigma_2 &= \omega\mu_0 \frac{X_s^2 - R_s^2}{(R_s^2 + X_s^2)^2}.\end{aligned}\tag{4.11}$$

Then, if the normal fluid can be modeled with a Drude form (*i. e.* if $\omega\tau_{TF} \ll 1$), by considering that the total density of carriers is given by the sum of the normal and superconducting densities (ρ_n and ρ_s respectively) and that at $T = 0$ only superfluid is present, $\rho_s(0) = \rho_s(T) + \rho_n(T)$, then it is possible to write the complex conductivity as

$$\sigma_1 - i\sigma_2 = \frac{\rho_n e^2}{m^*} \frac{\tau_{TF}}{1 + i\omega\tau_{TF}} - \frac{i}{\mu_0 \omega \lambda_L^2(T)}. \quad (4.12)$$

Combining Eqs. 4.11–4.12, one finally gets the two fluid estimate of the scattering time that can be calculated from the experimental data measured with our MWR technique [73]:

$$\tau_{TF} = \left(\frac{1}{\mu_0 \lambda_L^2(0) \sigma_1} - \frac{\omega(X_s^2 - R_s^2)}{2X_s R_s} \right)^{-1}. \quad (4.13)$$

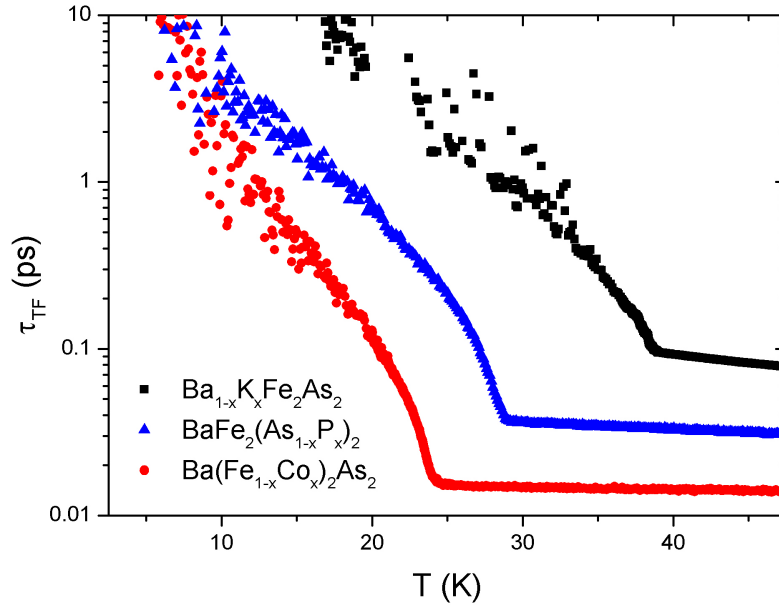


Figure 4.5: Scattering time τ_{TF} obtained through the two-fluid model presented in the text as a function of temperature for K, Co and P doped Ba-122. Adapted from [73]. ©2019 American Physical Society.

In some cases, at low temperature the resulting τ_{TF} are affected by high uncertainty mainly due to the uncertainty on σ_n . When this is the case a smoothing procedure [73] is performed before employing τ_{TF} in Eq. 4.10. The values of τ_{TF} obtained with this

procedure (see Fig. 4.5) are in good agreement with previously reported results [175] and, in general, at low temperature they are about two orders of magnitude larger than in the normal state [176].

Once the scattering time has been calculated, the experimental quasiparticle conductivity normalized at T_c can be fitted by adjusting only the weights w_i^σ (since the scale factor drops in $\sigma_n(T)/\sigma_n(T_c)$). The overall $\sigma_n(T)$ can then be obtained by fixing also the scale factor A [73].

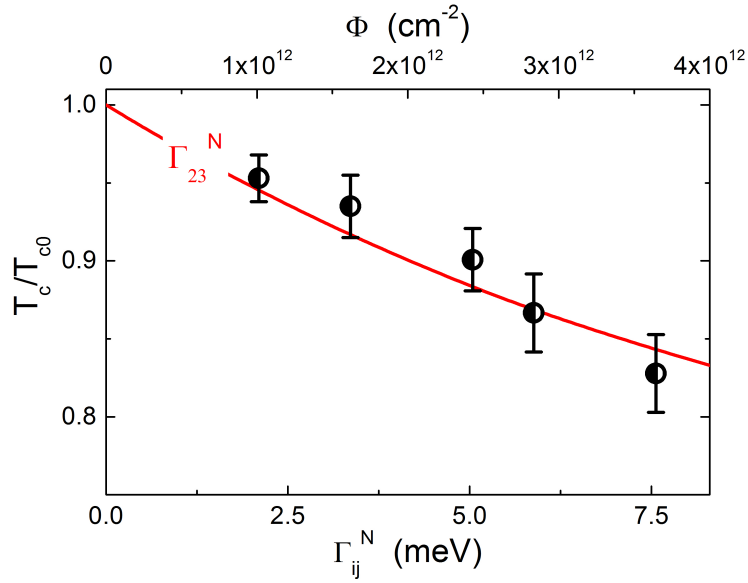


Figure 4.6: Experimental T_c degradation as a result of 250 MeV Au ions irradiation on optimally K-doped BaFe_3As_2 samples compared to Eliashberg calculations in order to fix the interband scattering parameter [72].

When a sample with additional irradiation-induced disorder is considered, the procedure described above must be repeated, but in this case the coupling constant matrix is the same as for the pristine sample and the interband scattering rate needs to be fixed to reproduce the new (decreased) experimental T_c [72, 126]. In general multiple irradiation experiments are performed on the same sample and, since the scattering rate Γ_{ij} has to be proportional to the concentration of defects, and therefore to the irradiation dose, this remaining free parameter is easily fixed. An example of the experimental and calculated decrease of T_c is shown in Fig. 4.6 for optimally K-doped BaFe_3As_2 samples irradiated with multiple doses of 250 MeV Au ions.

Chapter 5

Results

In this chapter, the results obtained on the combined experimental and theoretical study of IBSs with the approach previously discussed are presented. In Sect. 5.1, different pristine samples are analyzed and compared, with a focus on the penetration depth anisotropy in Sect. 5.1.2. The results of this section were also presented in Ref.s [73, 74]. Disorder is treated in Sect. 5.2 for the case of spatially extended defects generated by different types of ion irradiation: in Sect. 5.2.1 the similarities and differences due to defects shape are discussed and in Sect. 5.2.2 the complete experimental and theoretical approach is employed for the case of irradiation with 250 MeV Au ions. The results discussed in Sect. 5.2 can be found in Ref.s [71, 72]. Finally, in Sect. 5.3 the case of pointlike defects and small clusters introduced by 3.5 MeV protons is discussed. In the first part (Sect. 5.3.1) the effects of disorder on anisotropy are presented, whereas in Sect. 5.3.2 the case of elevate dpa levels able to modify the order parameter symmetry is examined. These results can be found in Ref.s [126, 177].

5.1 Pristine samples

As previously discussed, the study of the effects of disorder on superconducting materials needs to start from the characterization of pristine samples. In this section the analysis of differently doped Ba-122 [73] and of CaK-1144 [74] is presented, with a particular focus on the differences between hole, electron and isovalent doping in Ba-122 and on the anisotropic contributions to the penetration depth of CaK-1144. This also serves as a validation of the approach before treating the effects of scattering.

5.1.1 Ba-122 family

The critical temperature, penetration depth and quasiparticle conductivity of isovalently substituted, electron- and hole- doped Ba-122 can be all interpreted within the same framework of a multi band, s_{\pm} -wave Eliashberg model based on coupling provided by AFM-SF. To show this, samples with separate substitutions of all atomic species in the BaFe_2As_2 system (K for Ba, Co for Fe, and P for As) were studied with the experimental technique described in the second Chapter and the theoretical model discussed in the fourth.

Among the different substitutions it should be noted that the K for Ba one takes place out of the FeAs planes that support superconductivity, whereas the other two directly involve the FeAs planes. Substitution of Ba with K leads to a hole doped superconductor, whilst Co for Fe to an electron doped one. P instead is isovalent to As and does not change the doping level but increases chemical pressure.

For this study, optimally doped single crystals were employed: $\text{Ba}_{1-x}\text{K}_x\text{Fe}_2\text{As}_2$, $\text{Ba}(\text{Fe}_{1-x}\text{Co}_x)_2\text{As}_2$, and $\text{BaFe}_2(\text{As}_{1-x}\text{P}_x)_2$ with an analyzed substitution content respectively of $x=0.42$, 0.075 , and 0.33 . The samples were grown by the FeAs self-flux method by the group of Prof. Tamegai in Tokyo and were cut and cleaved to the shape of thin plates with thickness, along the crystallographic c -axis, of about $10 \mu\text{m}$ and an approximate aspect ratio of 10:10:1.

The Eliashberg analysis of these three systems was carried out within the realistic three band model, where two bands support holes and one electrons for K and P substitution and viceversa for Co substitution [40, 41, 156].

The main achievement of this study consists in the coherent interpretation of multiple properties experimentally measured on several samples of the same family, covering all possible types of substitution, within the same general model. The critical temperatures, gap values as well as the temperature dependences of both the penetration depth and the quasiparticle conductivity are very satisfactorily reproduced by the calculations despite the several constraints in the model (discussed in Chapter four) resulting in a very small number of free parameters and a limited range of variability with respect to the amount of data to be reproduced. Therefore, although

in some cases the matching is not quantitatively perfect, the overall agreement with the experimental data should be considered remarkable and the approach successful.

Critical temperature and energy gaps

The measured critical temperature (presented in Table 5.1 for the investigated compounds) is defined as the temperature at which the penetration depth diverges and the values found agree well with the literature [59, 178]. This definition is consistent with the one in the theoretical model: when the order parameters go to zero the superfluid density vanishes, corresponding to a divergence of λ_L . Also the energy gaps estimated with the Eliashberg procedure previously described reproduce well, at low-temperature, those reported in literature from ARPES measurements [40, 42, 43, 178, 179]. The imaginary axis solutions for the gaps as a function of temperature $\Delta_i(T)$ are shown in Fig.5.1, whereas the low-temperature values on the real axis $\Delta_i^R(0)$ are reported in Table 5.1. These values coincide with those obtained by analytical continuations from the imaginary axis with the Padé approximants technique.

Table 5.1: Summary of experimental values of the analyzed quantities and of the model parameters used to reproduce the data for the three different substitution studied in the Ba-122 family: experimental critical temperature T_c , low-temperature value of the penetration depth $\lambda_L^{exp}(0)$, microwave conductivity at T_c $\sigma(T_c)$, components of the electron-boson coupling-constant matrix Λ_{ij} , low-temperature values of the gaps on the real axis $\Delta_i^R(0)$, total plasma frequency ω_p , weights of the i -th band contribution to the penetration depth and quasiparticle conductivity w_i^λ and w_i^σ respectively.

dopant	T_c (K)	$\lambda_L^{exp}(0)$ (nm)	$\sigma(T_c)$ ($\Omega^{-1}m^{-1}$)	Λ_{12}	Λ_{23}	Λ_{13}	Λ_{ii}	$\Delta_1^R(0)$ (meV)	$\Delta_2^R(0)$ (meV)	$\Delta_3^R(0)$ (meV)	$\hbar\omega_p$ (meV)	$w_{1,2,3}^\lambda$	$w_{1,2,3}^\sigma$
K	38.7	197	$1.95 \cdot 10^6$	0.00	0.75	3.37	0.00	12.0	5.4	-12.0	1.00	0.1, 0.1, 0.8	0.6, 0.2, 0.2
Co	24.2	165	$0.47 \cdot 10^6$	0.20	0.00	2.72	0.30	7.2	-3.9	-7.8	0.20	0.85, 0.05, 0.1	0.39, 0.26, 0.35
P	29.0	160	$1.13 \cdot 10^6$	0.00	7.69	0.70	0.00	3.8	10.8	-8.3	0.55	0.5, 0.4, 0.1	0.12, 0.53, 0.35

Penetration depth

A comparison of experimentally determined (symbols) and calculated (solid lines) penetration depth increments $\Delta\lambda_L(T) = \lambda_L(T) - \lambda_L(0)$ for the three investigated

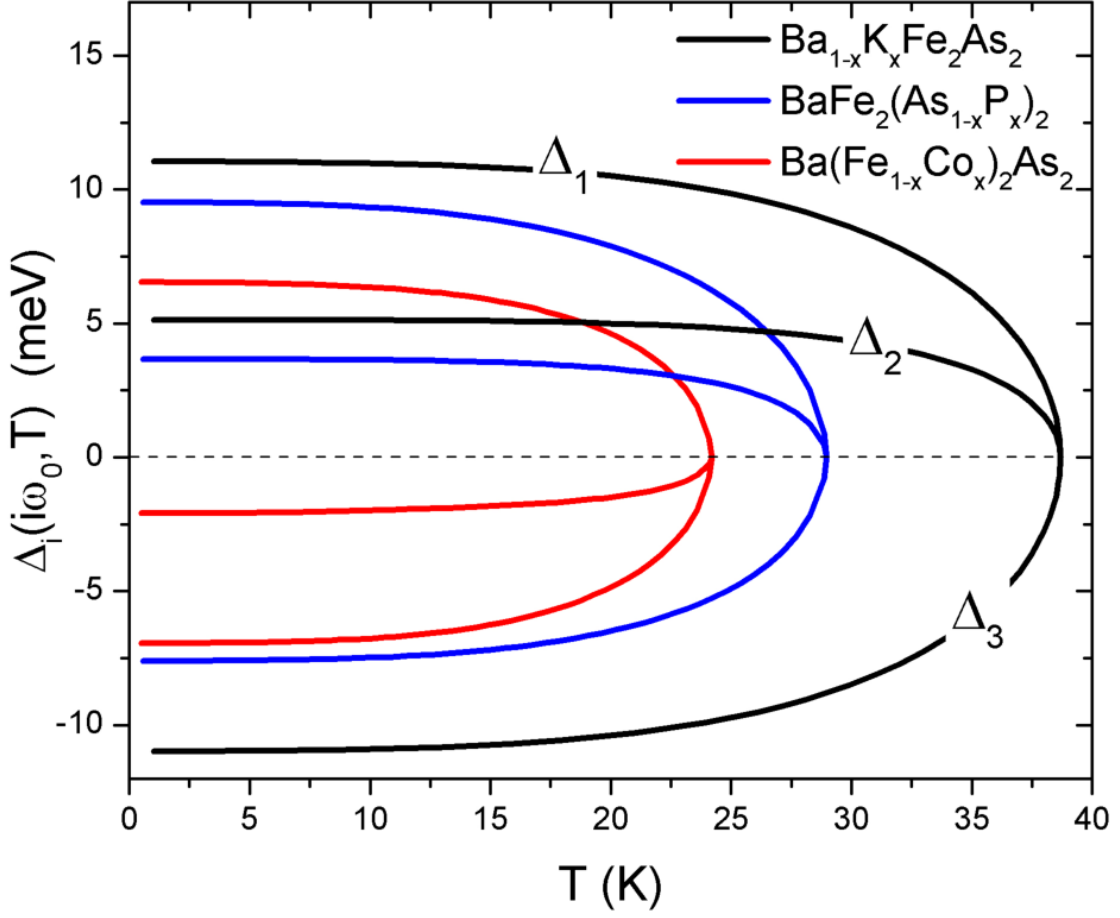


Figure 5.1: Imaginary axis solutions for the gaps as a function of temperature for the three compounds investigated. Adapted from [73]. ©2019 American Physical Society.

compounds is presented in Fig. 5.2. For all systems, it was possible to achieve a very good agreement between the experimental data and the calculated one and also with literature [180]. Nonetheless, it is necessary to make a distinction between the hole doped system and the other two. In the former case, it has been possible to obtain within the model also a $\lambda_L(0)$ value in remarkable agreement with the experimental one, i.e. $\lambda_L^{th}(0) = 230$ nm and $\lambda_L^{exp}(0) = 197 \pm 20$ nm, by employing a value of the plasma frequency in good agreement with literature data: $\omega_p = 1$ eV.

Conversely, for the electron doped and isovalently substituted systems the comparison is not as satisfying. Although the temperature dependence of the penetration depth is also very well reproduced (Fig. 5.2), the theoretical low temperature values largely

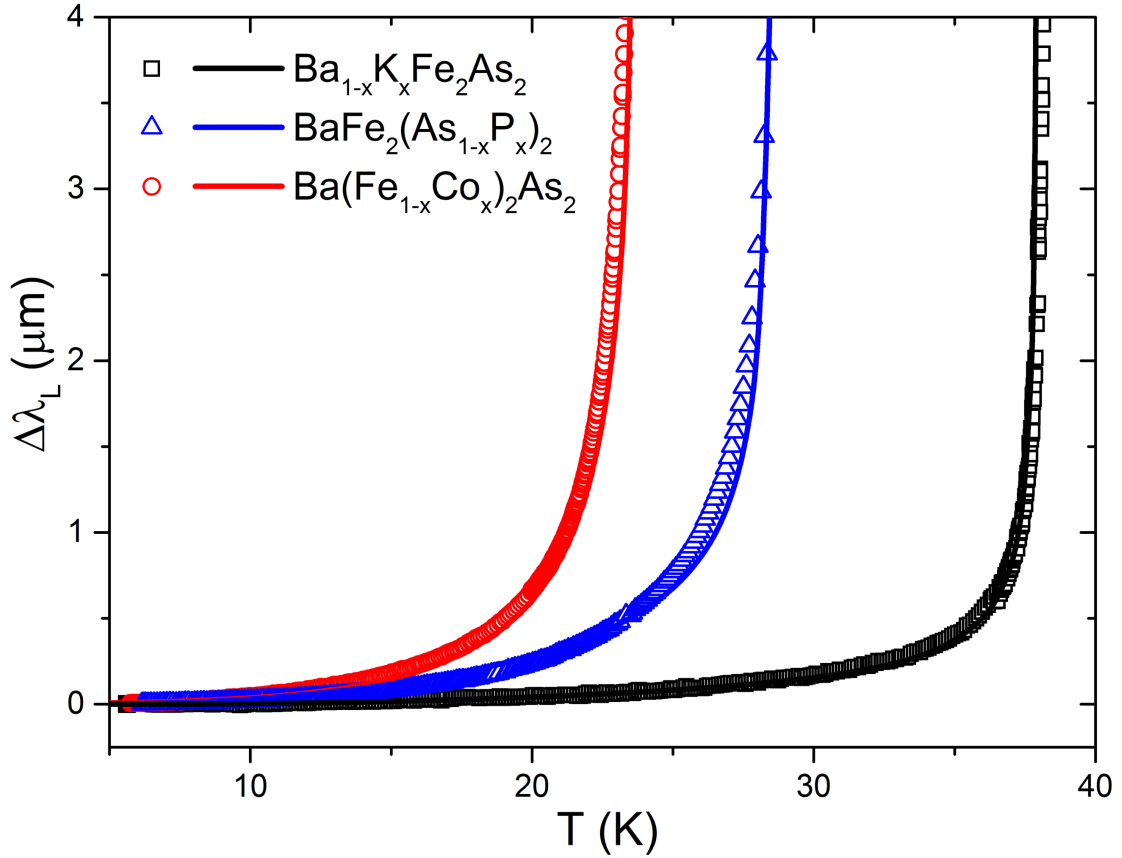


Figure 5.2: Comparison between measured (symbols) and theoretical (lines) penetration depth increments, $\Delta\lambda_L = \lambda_L(T) - \lambda_L(0)$, for the three systems. Adapted from [73]. ©2019 American Physical Society.

exceed the experimental ones (even reaching almost $1 \mu\text{m}$ for the Co doped case). The experimentally determined $\lambda_L^{\text{exp}}(0)$ for the three systems are in line with the (little) data present in literature, where values around 200 nm are usually given for compounds of the Ba-122 family [181].

This discrepancy between experiments and theory was already reported for the case of Co doping and it has previously been attributed to Fermi-liquid effects that were not taken into account in the adopted model [182]. In the case of Eliashberg models though, strong coupling effects are taken into account by the presence of the renormalization functions $Z_i(i\omega_n)$, and therefore these explanations by themselves are not satisfactory. Therefore the origin of these differences is still unclear and deserves further discussion. It seems likely that the discrepancy originates from the fact that the relation between

$\lambda_L(0)$ and ω_p ($\omega_p = c/\lambda_L(0)$) loses its validity or needs to be modified. For this reason we preferred to give the calculated ω_p in Table 5.1 instead of $\lambda_L^{th}(0)$ as a reference. A possible cause for this needed change of relation could lie in the fact that our model does not include vertex corrections.

From a structural point of view, it should be noted that the main difference between the cases of Co and P substitution with respect to K, lies in the involvement of atoms in the FeAs planes (responsible for the superconducting properties) that is not present in the case of K for Ba. Additionally, the three-dimensionality of the FSs is believed to be sensitive to the pnictogen height from the FeAs plane [183]. Substituting P for As reduces this parameter, whereas substitution of Ba with K does not [184]. Therefore, it is possible that the observed anomalous relation between $\lambda_L(0)$ and ω_p could be ascribed to the direct introduction of chemical disorder in the FeAs active layers and/or to the variation of the height of the pnictogen from these planes that in turn might influence the electronic properties. However, although this disorder could also originate carriers scattering, as discussed in the fourth chapter of this thesis in our model we need to consider the pristine optimally doped samples as free from scattering in order to keep manageable the number of input parameters.

Quasiparticle conductivity

The experimental and calculated quasiparticle conductivity are compared for each compound in Fig. 5.3. The curves show a very good agreement for P and Co substituted samples and a still reasonable one for K substitution, in particular if one considers that this is not an optimized fit of this experimental data by itself but that most parameters were already fixed to reproduce at best the London penetration depth curves. Noteworthy is the fact that the temperature at which the maximum of the broad peak is found (just below $T_c/2$) is fairly well reproduced for all systems.

It is important to discuss the presence and nature of this peak, also in light of the fact that it has been possible to reproduce it well within the model. In fact, the observation of the so-called coherence peak allows to discuss the superconducting order parameter symmetry, being often considered evidence of a uniform gap function. A coherence peak is observed just below T_c in the quasiparticle conductivity curve of dirty isotropic *s* wave BCS superconductors [185], and it develops if the portions of FS probed by the experiment have gaps of similar magnitude and same sign [186]. For this reason it is

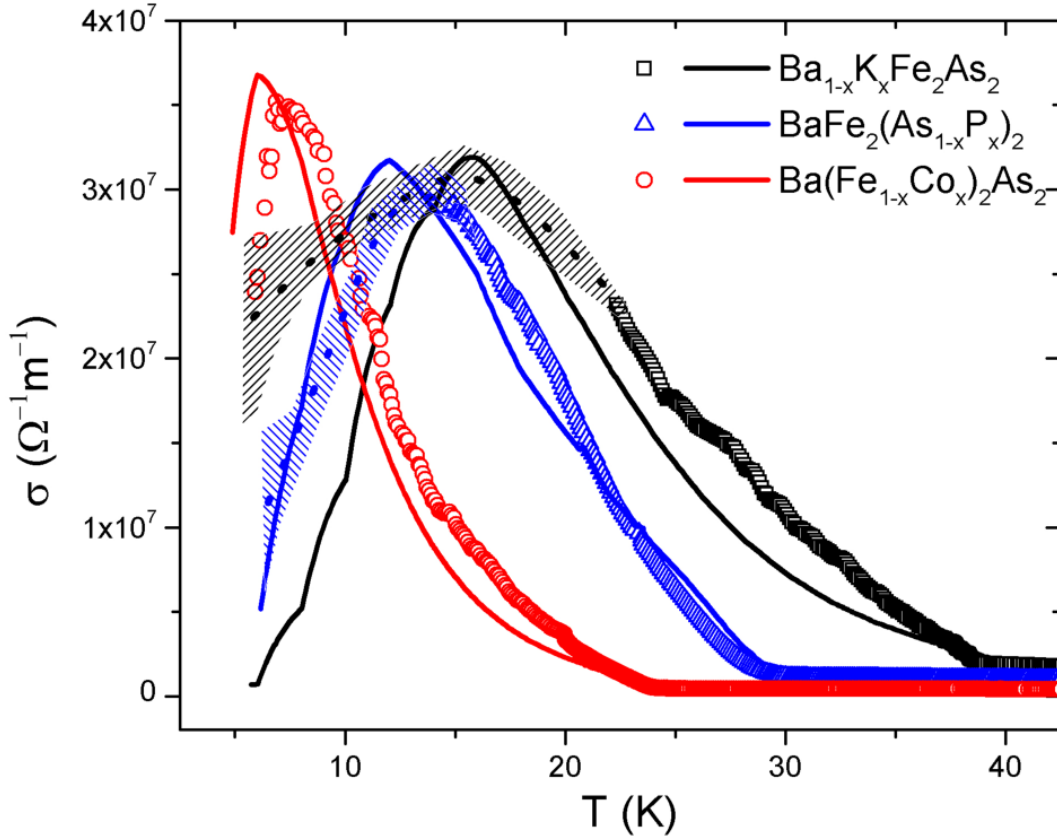


Figure 5.3: Comparison between measured (symbols) and theoretical (lines) quasiparticle conductivity, for the three systems. In the cases of K and P substitution the low-temperature experimental data was subject to high uncertainty (shaded areas) and a smoothing procedure was performed (dotted lines) for clarity of presentation. Adapted from [73]. ©2019 American Physical Society.

important to consider if the experimental technique employed probes the system with a large or small momentum transfer with respect to the fermiology of the analyzed compound. Due to the sign-changing d wave nature of the order parameter in cuprate superconductors, no coherence peak is observed (with any technique) but rather a large one much below T_c [187] that develops due to the decrease of the quasiparticle density and concomitant increases of quasiparticle scattering time with decreasing the temperature.

For the case of IBSSs, and specifically for the Ba-122 family, it is still unclear whether

the coherence peak is present. It was not found with NMR measurements of the relaxation rate [188, 189] but it was observed with measurements of the terahertz conductivity on $\text{Ba}(\text{Fe}_{1-x}\text{Co}_x)_2\text{As}_2$ [186, 190]. These two contrasting results might be reconciled considering the different nature of the probes employed and the fermiology of Ba-122 compounds. NMR is a local probe that couples parts of the FS that differ by large momentum. Therefore the absence of a coherence peak supports the sign changing (s_{\pm}) extended s -wave symmetry of the order parameter in which different bands have gaps with different sign [175]. Conversely, the small momentum of photons at THz frequencies allows only to probe the zero-momentum excitations near the Fermi surface. Therefore a coherence peak can emerge because only a single sign of the order parameter (and a single gap value) is detected due to the large distance in momentum space of different sheets of the FSs on which the gap changes sign. The situation is then completely analogous to a single and uniform gap superconductor. The situation is similar for conductivity measurements with microwaves (GHz frequencies), due to the long wavelength. As a matter of fact, a hint of a coherence peak was detected with this type of technique in K doped Ba-122, although it was masked by the presence of another larger and higher peak at lower temperatures [175]. This larger peak, that was observed in several IBSs [176], could be due to the same mechanism described for the cuprates and in principle could completely cover and hide a coherence peak. In this case, it is possible to better highlight the traces of the coherence peak by subtracting a residual term in the surface resistance from the measured data [83]. In the present case, it has been possible to reproduce within the Eliashberg model, based on the s_{\pm} symmetry, the bare untreated data and, in particular, the broad peak below $T_c/2$ that therefore is not a coherence peak (coherence effects are not taken into account by the model) that could anyways be present and hidden by it.

Nodes in the energy gap

Starting from the obtained experimental data it is also possible to discuss the presence of nodes in the order parameter. This is particularly important because it was suggested that large changes in the nodal topology of IBSs could be induced by very small variations in the size and corrugation of FSs, resulting in different observable behaviors [184].

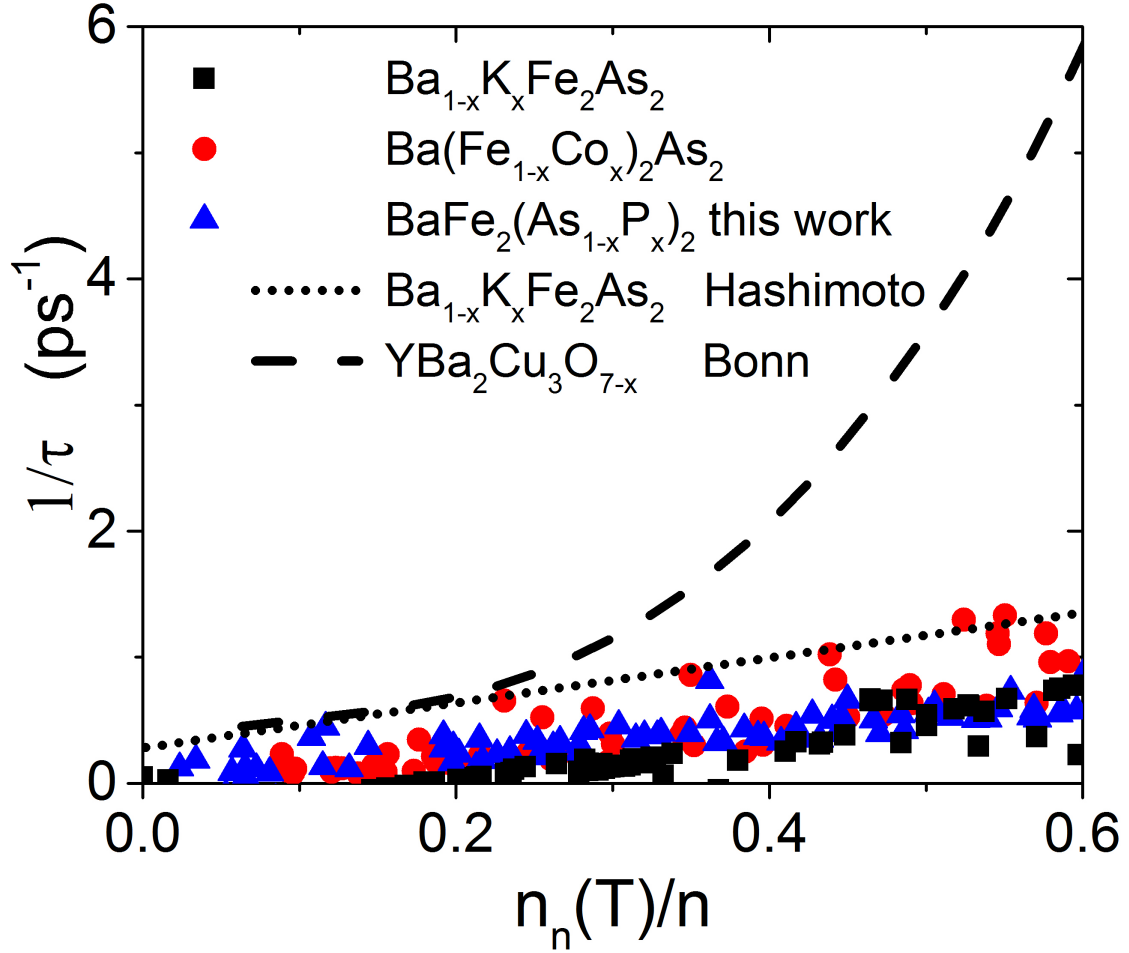


Figure 5.4: Quasiparticle scattering rate $1/\tau$ estimated with the two-fluid model as a function of the normalized quasiparticle density $n_n(T)/n$ for the cases of K, Co and P substitution, compared to the results at 28 GHz in $\text{Ba}_{1-x}\text{K}_x\text{Fe}_2\text{As}_2$ (dotted line) [175] and the results at 34.8 GHz in $\text{YBa}_2\text{Cu}_3\text{O}_{6.95}$ (dashed line) [191]. Adapted from [73]. ©2019 American Physical Society.

Among the discussed compounds, the one for which the existence of nodes is most debated is $\text{BaFe}_2(\text{As}_{1-x}\text{P}_x)_2$. Nakai *et al.* (using NMR) [192] and Yamashita *et al.* (with angle-resolved thermal conductivity measurements) [193] claimed that at optimal doping this compound presents line nodes. It was also proposed (from specific heat measurements) that, with increasing doping, the system goes from fully gapped for $x=0.32$ to strongly anisotropic gaps and possible nodes when overdoped with $x=0.55$ [194]. ARPES measurements by Yoshida *et al.* exclude horizontal nodes but could be consistent with

a modified s_{\pm} order parameter with nodal loops [43, 195]. Also ARPES measurements by Zhang *et al.* are consistent with the presence of circular line node on the largest hole band and rule out d wave character of the nodes while establishing the possibility of existence of "accidental" nodes in the extended s wave pairing symmetry that are not imposed by the symmetry of the system [196].

The presence or absence of line nodes can be inferred by looking at the quasiparticle scattering rate $1/\tau$ plotted against the normalized quasiparticle density n_n/n (calculated as $n_n(T) = n_{tot} - n_s(T)$ where $n_{tot} = n_s(0)$).

The relation between these two quantities is expected to be linear for an s wave superconductor without nodes [175] whereas for a d wave-like superconductor it should be superlinear: $1/\tau \sim n_n^3$. These data are plotted in Fig.5.4 for the three compounds studied and is compared to literature data for $Ba_{1-x}K_xFe_2As_2$ measured at 28 GHz [175] and for the d -wave case of $YBa_2Cu_3O_{6.95}$ at 34.8 GHz [191]. It can be seen that all the doped Ba-122 compounds follow a linear trend much like that of Ref.[175] and qualitatively very different from the case of YBCO. Therefore, our data excludes the presence of node lines (d wave like nodes) but nothing can be said about other nodal structures, such as nodal loops, that are consistent with the s_{\pm} symmetry.

5.1.2 Anisotropy in CaK-1144

As discussed in the second Chapter, by comparing measurements on samples with different aspect ratios it is possible to deconvolve the $\lambda_{L,c}$ and $\lambda_{L,ab}$ contributions to the penetration depth, and then obtain the anisotropy parameter $\gamma_{\lambda} = \lambda_{L,c}/\lambda_{L,ab}$. It is particularly interesting to study this quantity in $CaKFe_4As_4$ because, being superconducting without the need of introducing doping via chemical substitution, it is possible to look at this property in a clean system and evaluate the effects of disorder introduced both by chemical substitution and ion irradiation. In this section the anisotropy of $CaK(Fe,Ni)_4As_4$ single crystals with Ni content of 0%, 1.7% and 3.4% will be discussed, while the effects of proton irradiation induced disorder will be treated in section 5.3.1.

All studied samples are high quality single crystals of $CaK(Fe_{1-x}Ni_x)_4As_4$ grown out of FeAS flux by the conventional high temperature solution technique at the Ames Laboratories by the group of Prof. Canfield. Wavelength-dispersive X-ray spectroscopy

was used to determine the doping level [197]. The samples were cut and cleaved to the shape of rectangular thin plates with thickness, along the crystallographic c -axis, variable between about $2.5\mu\text{m}$ and $40\mu\text{m}$. Samples with different thicknesses, are fundamental to estimate the anisotropy in the material.

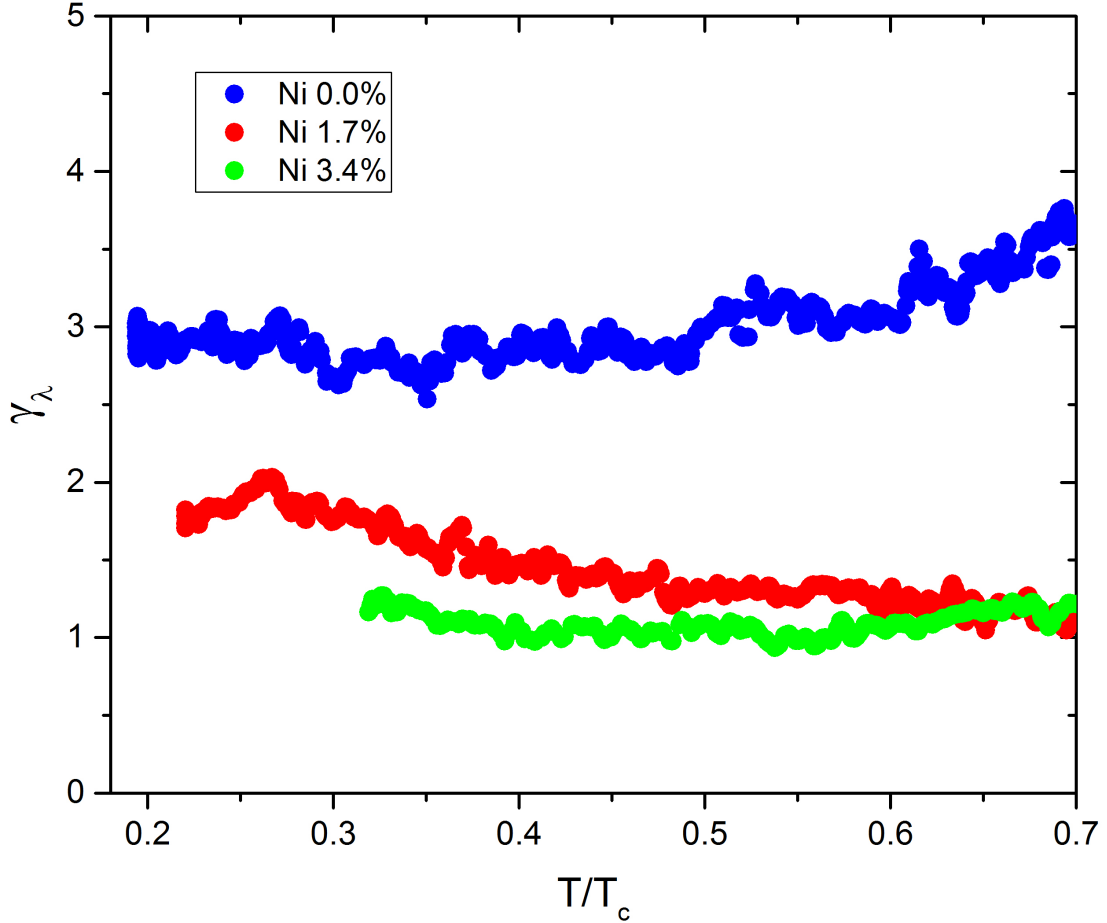


Figure 5.5: Anisotropy parameter $\gamma_\lambda = \lambda_{L,c}/\lambda_{L,ab}$ for the CaK-1144 system with Ni doping levels of 0% (blue symbols), 1.7% (red) and 3.4% (green).

Figure 5.5 shows the experimentally determined anisotropy of the penetration depth for all doping level analyzed. The data is shown only up to the temperatures for which all approximations discussed in Chapter two are valid (specifically the most restrictive is the requirement that $\lambda_{L,ab} \ll c$). Data for the undoped material is in good qualitative agreement with the literature [198] (γ_λ is first quite constant

and then increases with increasing temperature above $T/T_c > 0.5$), although with larger absolute value. This slight difference could be due to the different techniques employed, and specifically to the different frequency regimes: at GHz frequencies the characteristic time for quasiparticle scattering is comparable to the characteristic time of the probe, resulting in a reduction of the isotropization effect of scattering and an enhancement of γ_λ . Ni doped samples are markedly more isotropic due to the substitution enhanced scattering. Moreover the temperature dependence of γ_λ seems to change: it decreases slightly with increasing temperature for the 1.7% case and is practically constant (the system is almost isotropic) for the 3.4% case.

Table 5.2: Summary of the Critical temperatures T_c and low temperature values of the ab component of the penetration depth $\lambda_{L,ab}(0)$ and of the anisotropy parameter $\gamma_\lambda(0)$ for undoped and Ni doped CaK-1144 samples.

Ni content (%)	T_c (K)	$\lambda_{L,ab}(0)$ (nm)	$\gamma_\lambda(0)$
0	34.7	170	2.9
1.7	29.0	240	1.9
3.4	19.7	300	1.2

5.2 Extended defects

The presence of defects, even if with relatively low density, can be used to investigate many aspects of the physics of a superconductor. Here we focus on the modifications induced in the superconducting properties of IBs by different types of defects produced by ion irradiation.

5.2.1 Comparison between irradiation typologies

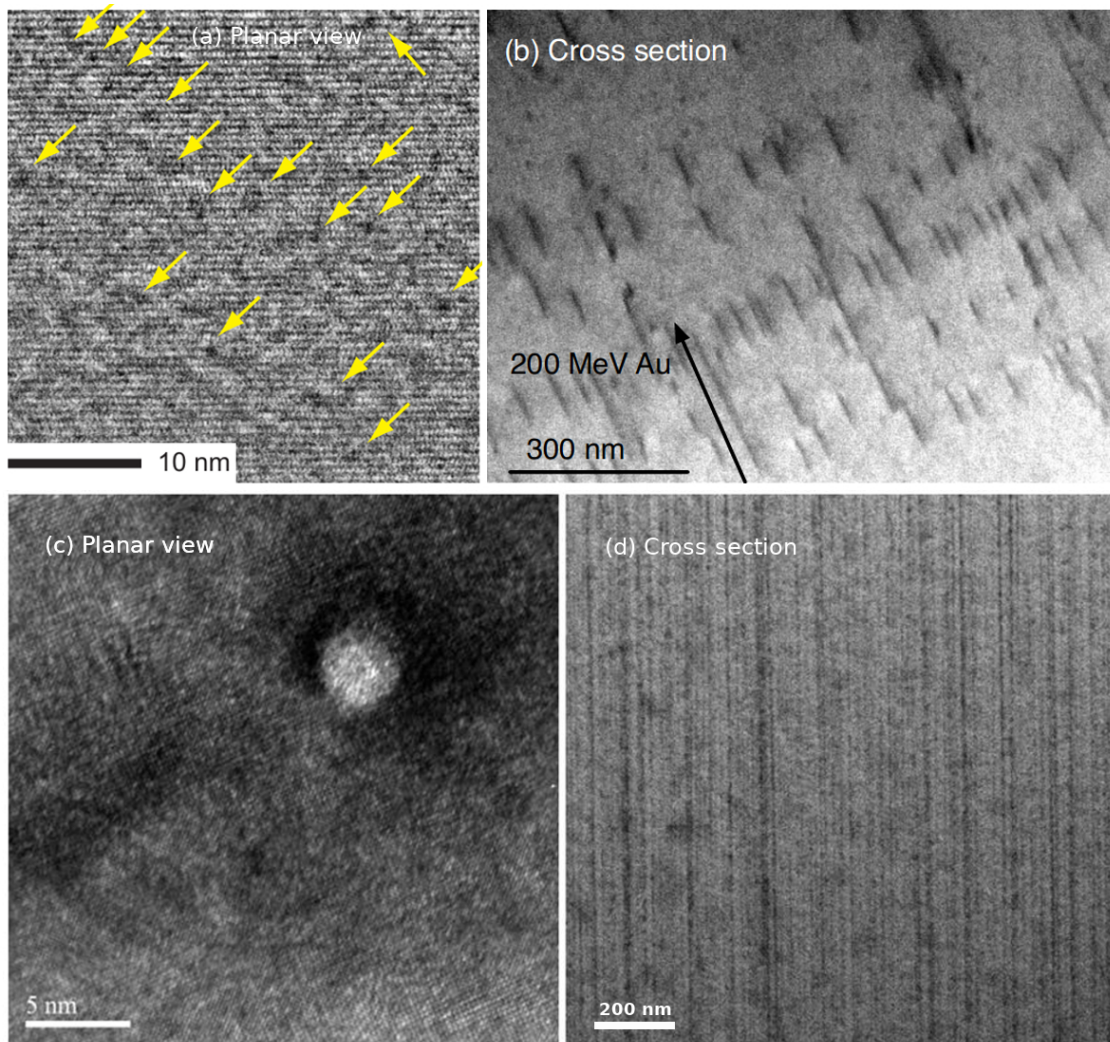


Figure 5.6: (a) TEM image of the planar view of a 3 MeV proton irradiated $\text{BaFe}_2(\text{As}_{1-x}\text{P}_x)_2$ crystal. Small defects cluster are marked by yellow arrows. Adapted from [199]. ©2018 American Physical Society. (b) TEM cross sectional image of a 200 MeV Au irradiated $\text{Ba}(\text{Fe}_{1-x}\text{Co}_x)_2\text{As}_2$ crystal. Adapted from [200]. ©2009 American Physical Society. (c) and (d) TEM Images by A. Ichinose (C.R.I.E.P.I. Kanagawa, Japan) of a 1.2-GeV Pb irradiated $\text{Ba}_{1-x}\text{K}_x\text{Fe}_2\text{As}_2$ crystal. The planar view (c) shows that the column's diameter is of about 3 nm while the cross-sectional view (d) shows that straight defects are created along the ion track.

In this section a comparison between the effects on critical temperature of different types of irradiation is carried out in order to investigate the importance of defect morphology on these quantities. As discussed in the third Chapter, 3.5 MeV protons mainly introduce point defects and small cluster [134], 1.2 GeV Pb ions produce continuous columnar tracks with a metallic core [132] and 250 MeV Au ions irradiation results in the formation of discontinuous but linearly correlated tracks [200]. Figure 5.6 shows TEM images of the different geometries of defects.

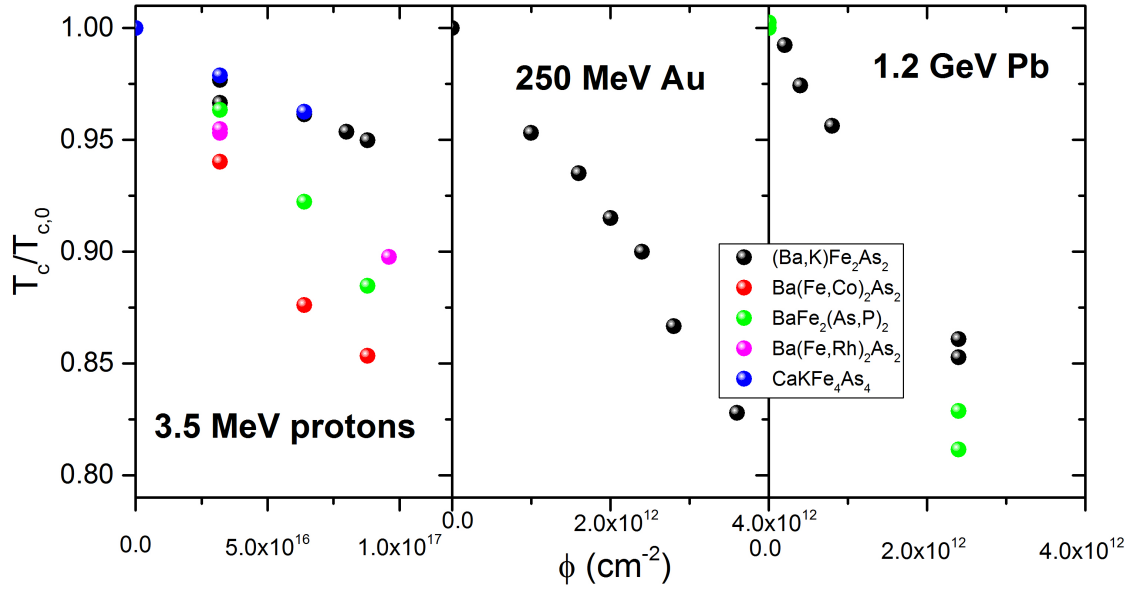


Figure 5.7: Critical temperature variation due to irradiation with 3.25 MeV protons on the left, 250 MeV Au ions in the center and 1.2 GeV Pb ions on the right, as a function of irradiation fluence for K-, Co, P-, Rh- doped Ba-122 and undoped CaK-1144 single crystals.

Figure 5.7 shows a comparison of the T_c degradation as a function of the irradiation fluence on different materials and with different ions and energies. When looking at the different dopings of the Ba-122 family exposed to 3.5 MeV proton irradiation, it emerges the fact that when substitution acts out of the superconducting plane the system is slightly more radiation hard than if the chemical substitution involves the FeAs planes.

By looking at the three fluence scales, it is clear that fluence alone is not a good parameter if different types of irradiation need to be compared: there is a four orders of magnitude difference between the fluences needed to produce comparable T_c

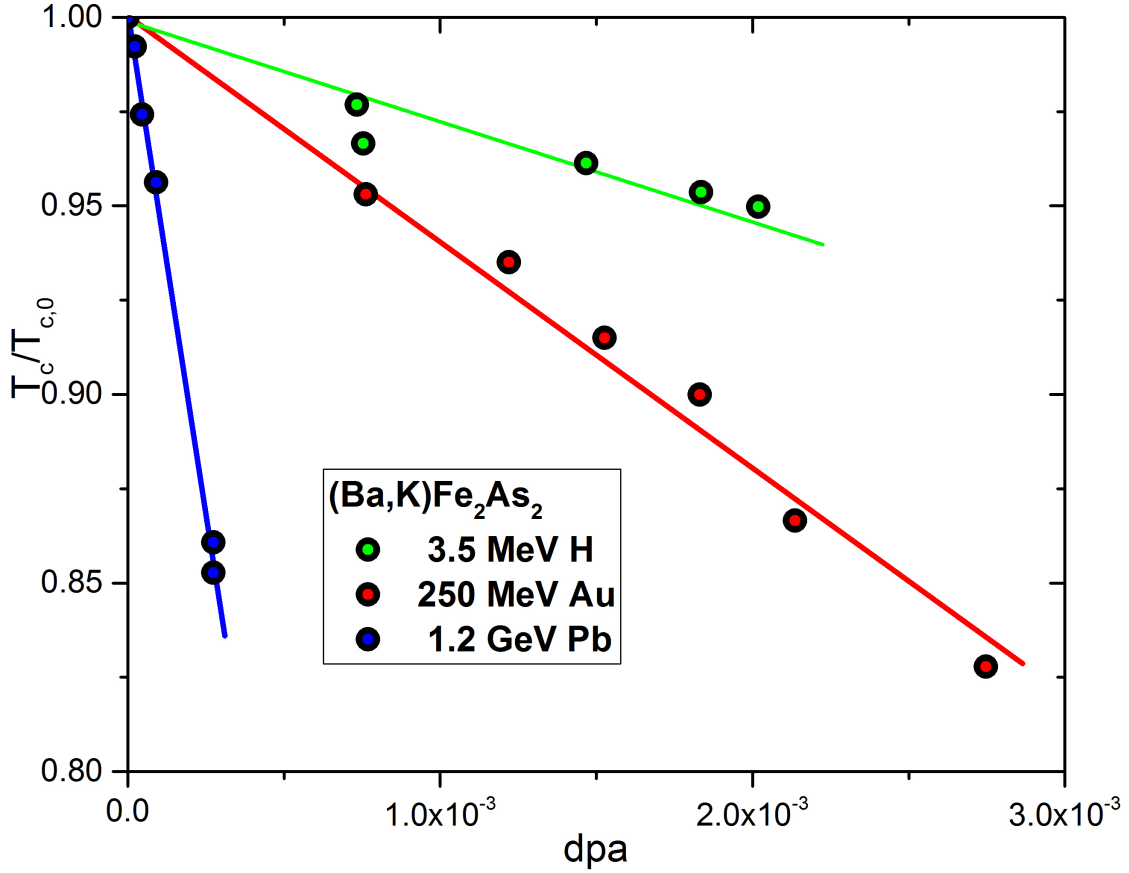


Figure 5.8: Critical temperature variation due to irradiation with 3.25 MeV protons, 250 MeV Au ions and 1.2 GeV Pb ions as a function of dpa for K-doped Ba-122 single crystals. Lines are guides to the eye.

decrements between the case of protons and that of heavy ions. Interestingly both discontinuous but correlated defects and continuous columnar ones seem to have a similar T_c vs fluence behavior. One would expect dpa to be a better parameter to compare systems in which disorder was introduced by different methods. However, as evident from Fig. 5.8 where the T_c degradation rates of the same material due to different types of irradiation are compared, also dpa fails in capturing all the effects of ion irradiation on a superconductor. This is due to the fact that the estimate of dpa relies on the assumption that a random distribution of pointlike defects is generated, whereas from the interaction of highly energetic heavy ions the defects are strongly correlated. Moreover, the electronic stopping power (that does not directly increase dpa) plays a very important role in the interaction mechanism of energetic heavy ions

with matter: the higher the ion energy and the heavier the ion, the more rapid is the degradation of T_c with respect to the calculated dpa.

5.2.2 250 MeV Au irradiation of $\text{Ba}_{1-x}\text{K}_x\text{Fe}_2\text{As}_2$

In this section, the effects of disorder induced by 250 MeV Au ion irradiation on $\text{Ba}_{1-x}\text{K}_x\text{Fe}_2\text{As}_2$ single crystals are discussed, highlighting that the observed modifications of the penetration depth and suppression of T_c are consistent with the s_{\pm} phase. The single crystals employed for this study were characterized also in the pristine state as discussed in the previous section. Disorder was then introduced by 250 MeV Au ion irradiation in multiple sessions. The implantation depth of the ions into the material estimated by SRIM [142] and PHITS [143] simulations is $14.5 \mu\text{m}$ and the samples were all thinner than $10 \mu\text{m}$. The total fluence achieved is $3.6 \times 10^{12} \text{ cm}^{-2}$, that corresponds to 72 T of dose equivalent field (the field needed to match the number of correlated tracks with fluxons) and the corresponding disorder level in dpa can be expressed as $7.6 \times 10^{-16} \times \Phi$, where Φ is the fluence expressed in cm^{-2} . A note of caution should be used here, since high energy ions create correlated defects, the use of dpa to quantify the disorder introduced in the samples has a larger uncertainty than in the case of, e. g., 3.5 MeV protons.

The measured penetration depth curves as a function of temperature for all irradiation doses are shown in Figure 5.9. Apart for decreasing the critical temperature, ion irradiation results in both an enhancement of the λ_L values and in a modification of its temperature dependence. This set of data was analyzed with the Eliashberg approach using the same three band model (and same parameters) employed for the pristine crystals discussed in the previous section, with the addition of impurity induced scattering treated in the Born approximation. As discussed in Chapter four, the scattering rates Γ_{ij}^N are directly proportional to the amount of defects present in the system, and therefore to the irradiation fluence. Moreover, when a three band model is considered, each non diagonal component of the scattering matrix could in principle be relevant in the modification of the observed properties. For the purpose of simplicity and to keep the number of parameters manageable, in a first approximation one can consider that only one of the interband scattering channels is responsible of the observable effects

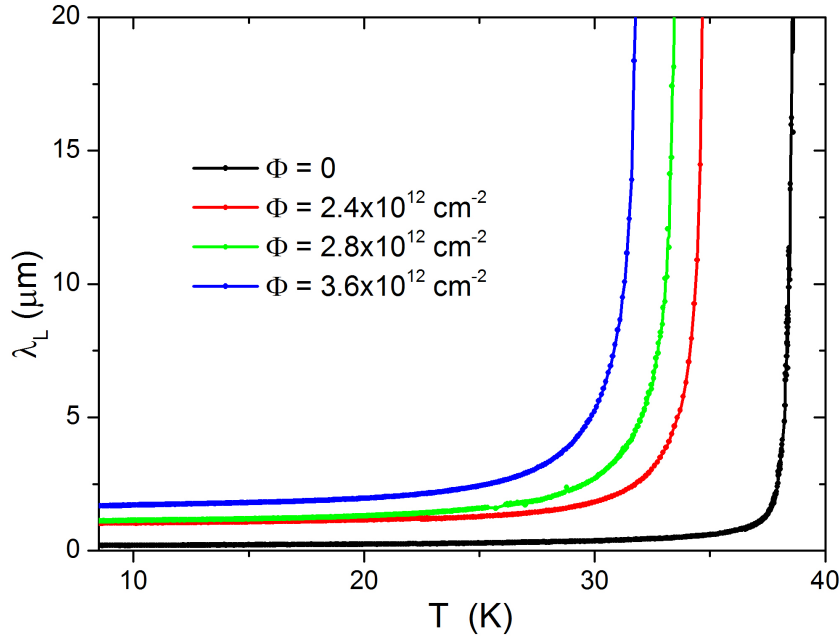


Figure 5.9: Measured temperature dependence of the London penetration depth of $\text{Ba}_{1-x}\text{K}_x\text{Fe}_2\text{As}_2$ crystal, before and with increasing irradiation doses of 250 MeV Au ions up to a total fluence of $\Phi = 3.6 \times 10^{12} \text{ cm}^{-2}$. Adapted from [72]. ©2017, Springer Nature

of disorder. Then it is necessary to determine which channel it is (which bands are involved). This was done by calculating the critical temperature decrease as a function of increasing scattering for each channel, and seeking agreement with experimental data by adjusting the proportionality constant between the scattering rate and the irradiation fluence (or equivalently dpa).

In Figure 5.10 this approach is shown with the upper (experimental data) and lower (theoretical calculations) scales already fixed on the only combination that gives a good agreement, identifying the scattering channel between bands 2 and 3 (scattering rate Γ_{23}^N) as the main mechanism responsible for the observed variation of properties. The proportionality constant between the fluence and scattering rate turns out to be $4.8 \times 10^{14} \text{ eV}^{-1} \text{ cm}^{-2}$.

Here it is particularly important to stress that the model employed for disorder is approximate and simplified. Not only in the fact that combined contributions by multiple scattering channels were neglected, but also the finite dimensions of the defects was

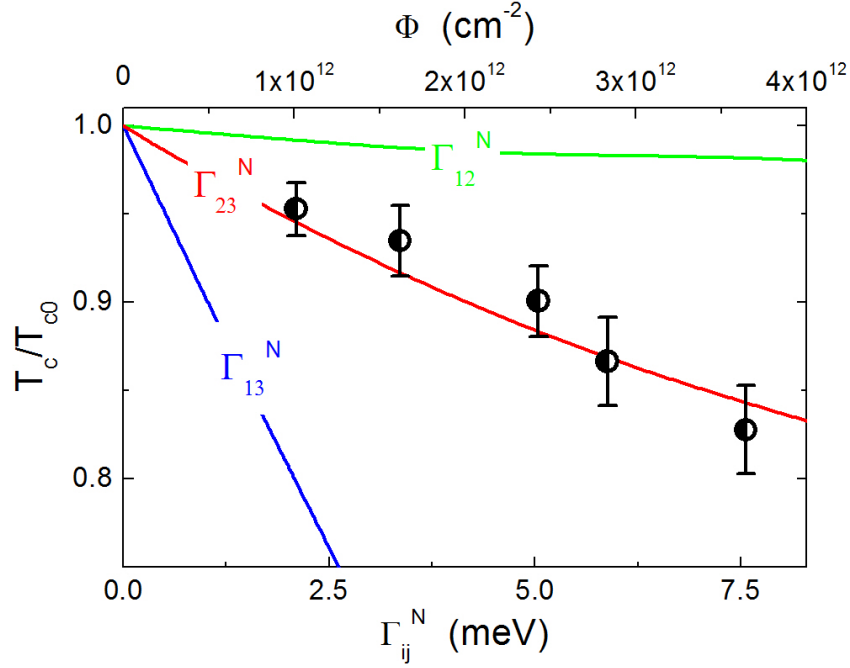


Figure 5.10: Experimental (symbols) variations of the critical temperature of K doped Ba-122 due to 250 MeV ion irradiation as a function of fluence (upper scale) compared to the calculated variation (solid lines) as a function of the interband scattering rate Γ_{ij}^N (lower scale). Blue, red and green lines represent the interband scattering channels that can cause the critical temperature suppression. The proportionality constant between the upper and lower scales has been modified until agreement between experimental and theoretical data was found. Adapted from [72]. ©2017, Springer Nature

disregarded. However, the good agreement found suggests that the observed effects can be explained effectively in terms of the pointlike defects and small clusters created by secondary particles. Therefore, either the contribution of the extended defects is of secondary importance -for the investigated properties- or they give a contribution analogous to that of small defects. Despite the already good agreement between experiment and theory, a very interesting development would be a model to obtain the carriers scattering parameters starting from a microscopic description of structural defect distributions.

In Figure 5.11 is shown the comparison between experimental and theoretical $\Delta\lambda(T)$ curves for the pristine sample and three irradiation doses. In all cases the agreement is very satisfactory and even small details such as the curvature change

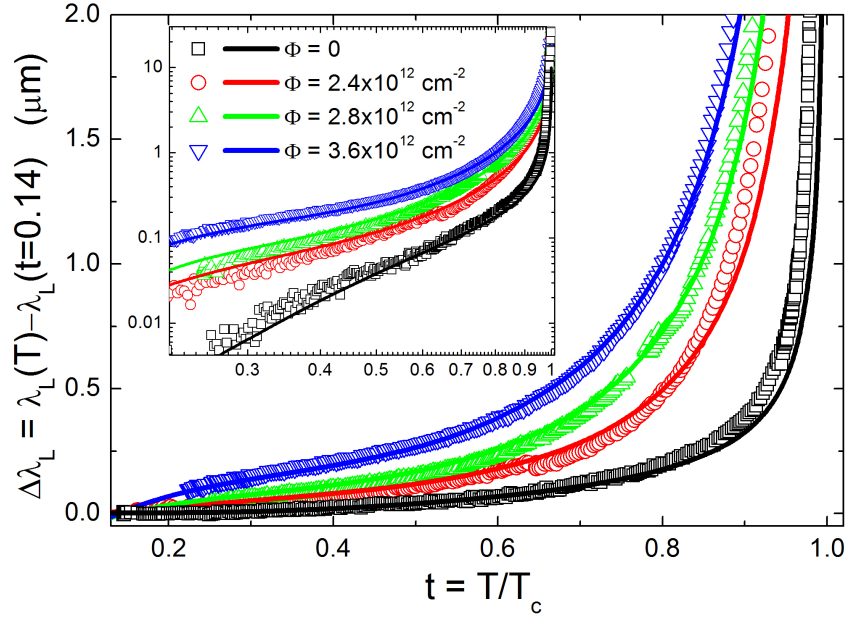


Figure 5.11: Comparison between the experimental (symbols) and calculated (lines) temperature dependence of the London penetration depth $\Delta\lambda_L(t) = \lambda_L(t) - \lambda_L(t = 0.14)$ for the pristine irradiated cases up to a total fluence $\Phi = 3.6 \times 10^{12} \text{ cm}^{-2}$. Adapted from [72]. ©2017, Springer Nature

in the highest fluence case is well reproduced. This nice agreement testifies that the three-band s_{\pm} model is able to explain consistently and in detail the behavior of IBSs and the effects of disorder on their penetration depth and critical temperature.

The estimated gap values on each band (different colors) are reported in Figure 5.12 for each disorder level (different line styles in the left panel) as a function of temperature on the left panel, from the imaginary axis solution, and of disorder (with values obtained on the real axis with the Padé approximants method) on the right panel. The values obtained for the pristine material ($\Delta_1 = 12.0 \text{ meV}$, $\Delta_2 = 5.2 \text{ meV}$ and $\Delta_3 = -12.0 \text{ meV}$) are in good agreement with earlier data [40]. With increasing disorder the gaps tend to shrink and the smallest one changes sign at the highest fluence. Despite this sign change, the symmetry of the system remains s_{\pm} because there are still gaps with opposite sign. In order to achieve the disorder induced s_{\pm} to s_{++} symmetry transition it is necessary to reach higher disorder levels (discussed in Sect. 5.3.2).

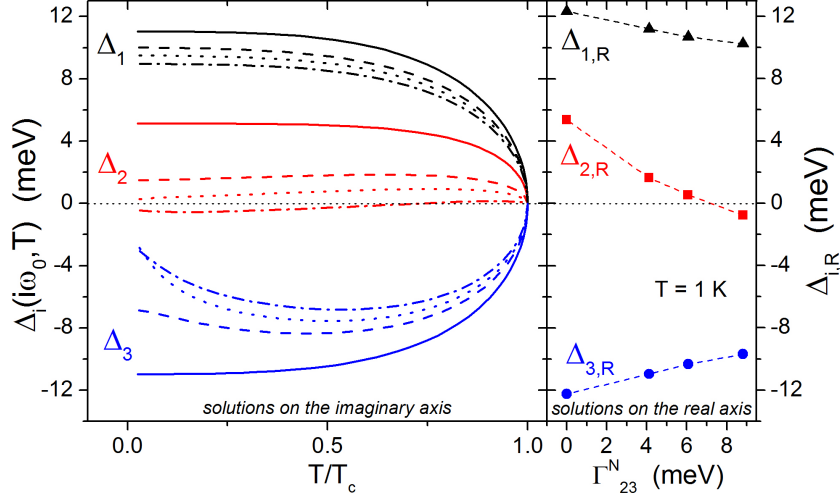


Figure 5.12: Left: imaginary axis solutions for the gaps on the three bands (black, red and blue) for the pristine material (solid lines) and with disorder levels corresponding to the fluences $\Phi = 2.4 \times 10^{12} \text{ cm}^{-2}$ ($\Gamma_{23}^N = 4.12 \text{ meV}$, dashed lines), $\Phi = 2.8 \times 10^{12} \text{ cm}^{-2}$ ($\Gamma_{23}^N = 6.07 \text{ meV}$, dotted lines), and $\Phi = 3.6 \times 10^{12} \text{ cm}^{-2}$ ($\Gamma_{23}^N = 8.81 \text{ meV}$, dashed dotted lines). Right: low temperature real axis solutions for the gaps on the three bands as a function of disorder. Adapted from [72]. ©2017, Springer Nature

As a consequence of irradiation, also the surface impedance gets modified. In Figure 5.13, both the real and imaginary parts are shown as a function of temperature for the pristine compound and with increasing disorder. As visible from the plot, at and above T_c $R_s = X_s$, meaning that as expected the system conforms to the classical skin effect. Right upon entering the superconducting state, a peak in the surface reactance emerges and it is progressively increased in size by irradiation. It was pointed out that its nature can be explained by the screening of the external microwave field: the reduction of the density of quasiparticles upon decreasing temperature is not compensated immediately by the superconducting current increase [174]. The temperature at which the peak is observed depends on a combination of external conditions and properties of the material: it is mainly determined by the product $\omega\tau$ between the microwave field frequency ω and the quasiparticle scattering time τ . Since disorder increases scattering, τ decreases with increasing the dose and therefore the peak shifts to lower temperature.

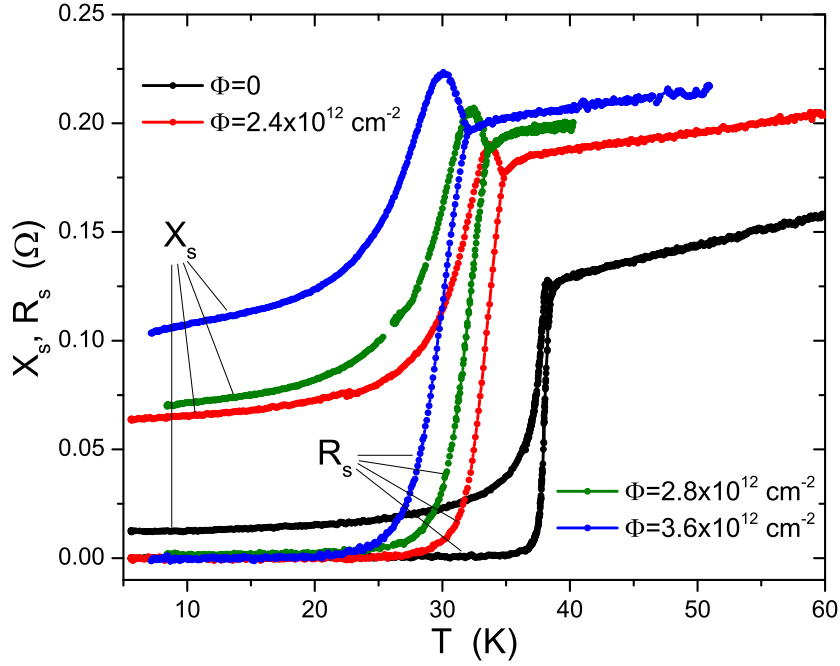


Figure 5.13: Normalized real (R_s) and imaginary (X_s) parts of the surface impedance (Z_s) as a function of temperature for the pristine case and for increasing levels of disorder induced by 250 MeV Au ions irradiation. Adapted from [71]. ©2018 IOP Publishing.

5.3 Pointlike defects

5.3.1 Anisotropy

The CaK-1144 samples discussed in section 5.1.2 were irradiated with 3.5 MeV protons in order to study how the penetration depth anisotropy is influenced by irradiation induced disorder.

Figure 5.14 shows the experimentally determined anisotropy of the penetration depth for the undoped samples of $\text{CaKFe}_4\text{As}_4$ in the pristine state and with additional irradiation induced disorder. The qualitative behavior is not strongly influenced by this type of disorder: γ_λ increases with temperature both for the pristine and disordered cases. From a quantitative point of view the anisotropy is reduced by disorder as expected: isotropic scattering from pointlike and small defects makes the system less direction dependent.

The same considerations hold also for the case of CaK-1144 with 1.7% of Ni substitution.

Table 5.3: Summary of the Critical temperatures T_c and low temperature values of the ab component of the penetration depth $\lambda_{L,ab}(0)$ and of the anisotropy parameter $\gamma_\lambda(0)$ for undoped and Ni doped CaK-1144 samples pristine and proton irradiated.

Ni content (%)	Irradiation fluence (cm^{-2})	T_c (K)	$\lambda_{L,ab}(0)$ (nm)	$\gamma_\lambda(0)$
0	0	34.7	170	2.9
0	3.2×10^{16}	34.0	480	1.4
0	6.4×10^{16}	33.8	680	1.0
1.7	0	29.0	240	1.9
1.7	1.6×10^{16}	28.5	500	1.2
3.4	0	19.7	300	1.2

Disorder makes the system more isotropic, and in this case the direction dependence is almost completely lost with values of γ_λ close to 1 for an irradiation fluence of $1.6 \times 10^{16} \text{ cm}^{-2}$. In the pristine state the anisotropy decreases with temperature as it does (although very faintly) for the disordered case. It is interesting to note that the irradiated case of 1.7% Ni doping has a very similar γ_λ profile to that of the pristine samples with 3.4% Ni doping.

From the study presented here and in Sect. 5.1.2 it emerges that substitutional and irradiation induced disorder act on the anisotropy of IBSs in different ways, possibly allowing to tune it as desired for specific applications.

5.3.2 Elevate disorder

In this last section, a study of the effects of high dpa levels in IBSs is presented, focusing on the experimental identification of the transition between the s_\pm and s_{++} order parameter symmetries and its validation with the Eliashberg approach.

As discussed in Chapter three, this disorder induced transition was proposed as a method to identify the s_\pm symmetry in the pristine compound [23, 24, 65, 201] and is

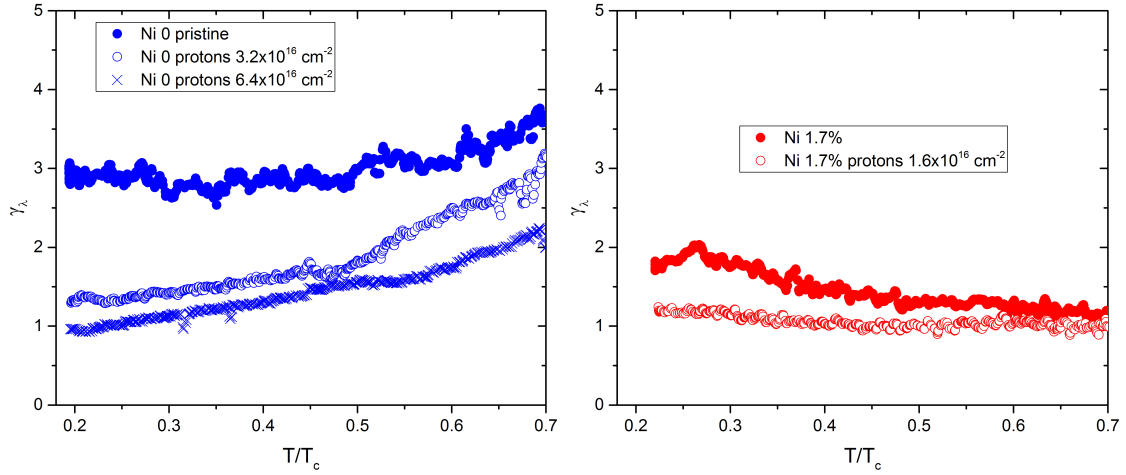


Figure 5.14: Left panel: Anisotropy parameter $\gamma_\lambda = \lambda_{L,c}/\lambda_{L,ab}$ for the undoped CaK-1144 system in the pristine state (full blue circles) and with increasing doses of proton irradiation (empty blue circles and crosses). Right panel: same quantity for the CaK-1144 system with 1.7 % Ni doping in the pristine state (full red circles) and after proton irradiation (empty red circles).

due to the tendency of the gaps to converge towards the same value when disorder is increased [24]. If the system starts with gaps that have opposite sign it is inevitable that, in order to converge to the same finite value, at least one gap has to close and reopen changing sign, thus realizing the s_{++} state. Most importantly, it was proposed that the transition would have specific signatures in observable properties, and in particular in the low temperature superfluid density: at the transition it should increase, breaking the monotonous decrease expected with increasing disorder [24, 125]. Other hallmarks are also expected in the optical conductivity (observed experimentally on $\text{Ba}(\text{Fe}_{1-x}\text{Co}_x)_2\text{As}_2$ thin films irradiated with 200-keV protons [125]) together with a weaker dependence of the critical temperature on disorder [106].

In order to observe the signature of this transition in the superfluids density, and more directly on the low temperature value of the penetration depth, a study on $\text{Ba}(\text{Fe}_{1-x}\text{Rh}_x)_2\text{As}_2$ single crystals was carried out with the combined experimental and theoretical approach described in the previous chapters. Disorder was introduced with multiple doses of 3.5 MeV proton irradiation that, as discussed in the third chapter, ensures that mostly isotropically distributed pointlike defects and small clusters are

introduced in the system. The total fluence reached was $2.08 \times 10^{17} \text{ cm}^{-2}$, equivalent to a dpa of 6.63×10^{-3} , as estimated by the PHITS [143] and SRIM [142] codes. A summary of the irradiation sessions and corresponding dpa values is given in Table 5.4.

Single crystals of optimally doped $\text{Ba}(\text{Fe}_{1-x}\text{Rh}_x)_2\text{As}_2$, with analyzed substitution level of $x=0.068$, that results in $T_{c0}=23.5 \text{ K}$, were produced with the self flux conventional growth technique [202–204] at the Ames Laboratories by the group of Prof. Canfield. The samples were cut and cleaved to the shape of thin plates with thickness, along the crystallographic c -axis, smaller than the implantation depth of 3.5-MeV protons in the material, estimated to be $67 \mu\text{m}$ by Monte Carlo simulations.

As discussed in the third chapter, at high levels of disorder the Born approximation is expected to lose its validity and therefore it is necessary to treat scattering within the T -matrix approach. Unfortunately this largely increases the number of free parameters of the model and makes unpractical the use of a realistic three band approach, making it necessary to work with a simplified two band model.

Rh doped Ba-122 has very similar behaviors [205, 206] to the Co doped compound due to the fact that Rh and Co are isoelectronic species. Therefore, although there is a lack of literature about this specific compound, it is reasonable to assume the same electronic structure as in the Co doped case as a starting point for the theoretical modelling. In particular, for the normal densities of states ratio between the two bands at the Fermi level, $N_1(0)/N_2(0)$, is employed the same value as for the Co doped compound discussed in the first section of this chapter with the precaution to sum up the contributions of the two electronic bands of the three-band model. The procedure described in the previous Chapter to fix all input parameters was employed to reproduce the experimental data for all levels of disorder resulting in the values summarized in Table 5.4. In particular, disorder was modelled keeping the intra- to inter-band scattering ratio $\eta = 1$, as done in Ref. [125], while Γ_1 is proportional to the amount of scatterers in the system and therefore increases linearly with dpa (reaching 2.35 meV for the most irradiated case) and the generalized cross section σ increases from 0 (Born limit, unirradiated crystal) to 0.278 going towards the unitary limit.

The bare experimental evidence for the disorder induced s_{\pm} to s_{++} transition is presented in Figure 5.15: the lower panel shows the low temperature values of the

Table 5.4: Summary of the parameters values employed to reproduce all experimental data: T_c , $\lambda_L(T)$ and $\sigma_n(T)$ for all doses of proton irradiation, *i.e.* for increasing disorder, here labelled both by the irradiation fluence and by the average dpa introduced in the samples. The normal state scattering rate Γ_1 is proportional to disorder, σ is the generalized cross-section that allows to move from the Born approximation to the unitary limit, η is intra- to inter-band scattering ratio, Λ_{ij} are the elements of the coupling-constant matrix and $w_1 = w_1^\sigma = w_1^\lambda$ is the weight of band the first band contribution to both the penetration depth and quasiparticle conductivity.

Cumulative fluence (cm^{-2})	dpa ($\times 10^{-3}$)	Γ_1 (meV)	σ	η	Λ_{11}	Λ_{22}	Λ_{12}	w_1
0	0	0	0	1	1	2.65	-0.17	0.98
3.2×10^{16}	1.02	0.361	0	1	1	2.65	-0.17	0.28
9.6×10^{16}	3.07	1.08	0.09	1	1	2.65	-0.17	0.25
12.8×10^{16}	4.10	1.44	0.10	1	1	2.65	-0.17	0.15
16.0×10^{16}	5.12	1.81	0.10	1	1.2	2.65	-0.13	0.90
17.6×10^{16}	5.63	1.99	0.14	1	1.2	2.65	-0.13	0.82
19.2×10^{16}	6.15	2.17	0.21	1	1.2	2.65	-0.13	0.78
20.8×10^{16}	6.63	2.35	0.28	1	1.2	2.65	-0.13	0.75

penetration depth for increasing disorder (expressed by the dpa value) with a clear drop that corresponds to the predicted increase of superfluid density. This drop identifies the s_\pm to s_{++} transition at a dpa value near 0.0046. Also the normalized critical temperature (upper panel, left scale) shows a clear change of behavior at the same value of disorder where $\lambda_L(0)$ drops: it becomes constant and even slightly recovers. The tiny increase of T_c above dpa $\sim 6 \times 10^{-3}$ is a minor effect that might have two opposite explanations, both related to the interaction with a secondary, weak, magnetic order. If a secondary competing order, such as spin density wave, is present and has a stronger suppression rate with disorder than superconductivity itself, it could cause a T_c enhancement [207]. Conversely, also the stabilization of superconductivity by a weak local magnetic phase induced by disorder is possible and could lead to a slight enhancement of the T_c [208] (indeed, a weak magnetic signal in proton-irradiated crystals was reported [204]). However, in both cases such a feeble

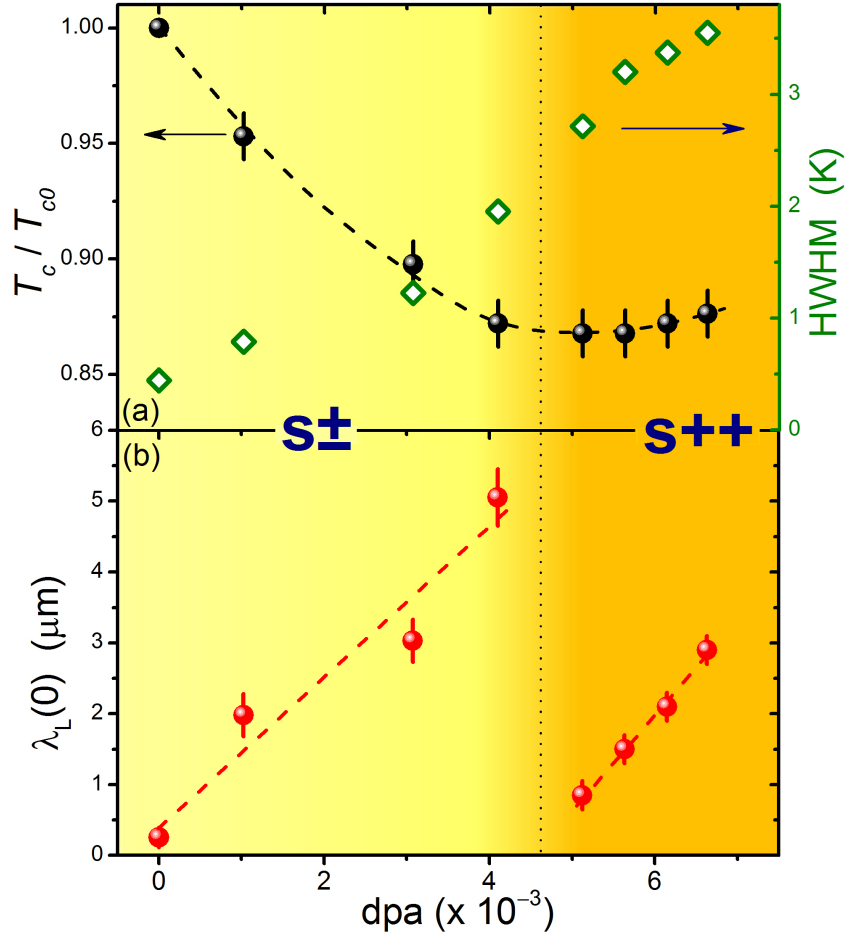


Figure 5.15: a) Modification of the critical temperature (left scale) by the irradiation-induced disorder, expressed by the dpa introduced in the sample as estimated by Monte Carlo simulations. Here T_c is the temperature at which $\lambda_L(T)$ diverges (T_{c0} for the pristine case). On the right scale the superconducting transition width is shown. (b) Disorder dependence of the low temperature value of the London penetration depth. The s_{\pm} and s_{+++} phases are indicated by different background colors and the disorder induced transition between them has been identified by the predicted $\lambda_L(0)$ drop. Dashed lines are guides to the eye. Adapted from [126]. ©2018 American Physical Society.

effect can emerge and become visible only in a state where the pair breaking effect of disorder on the primary superconducting order is weak (such as the s_{+++} state) again supporting the existence of a transition from s_{\pm} to s_{+++} . On the right scale of the upper panel of Figure 5.15 is shown that the superconducting transition width increases linearly with irradiation dose, testifying the increase of disorder in the system.

To validate the observation of the disorder driven s_{\pm} to s_{++} transition, the Eliashberg analysis was carried out, reproducing self consistently all the measured quantities starting from the critical temperatures for pristine samples and all irradiation doses and the temperature dependence of the superfluid density. Then also the quasiparticle conductivity was reproduced without any additional input parameter by taking the same weights for the bands contributions $w_1 = w_1^{\sigma} = w_1^{\lambda}$.

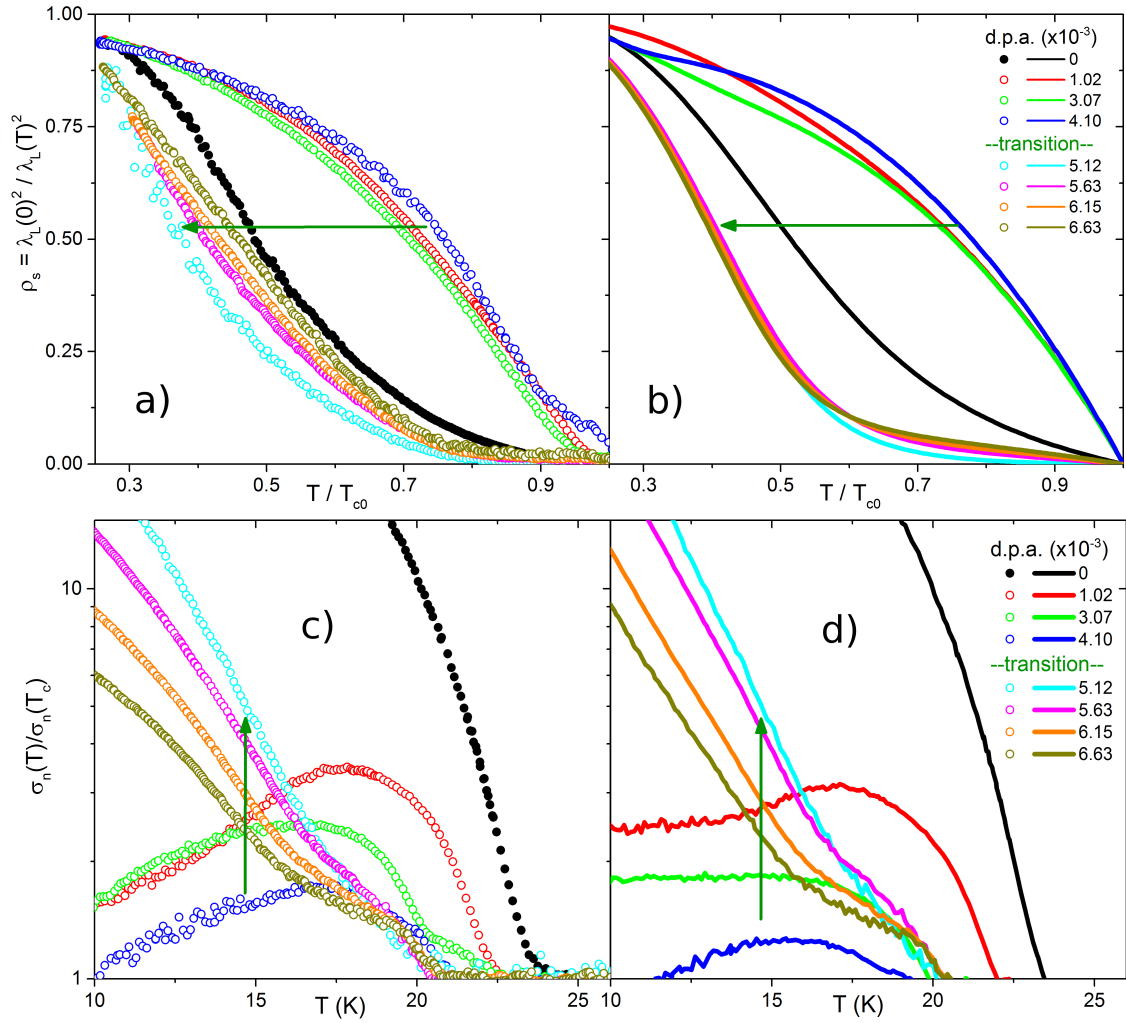


Figure 5.16: Comparison between the experimental (left column, symbols) and calculated (right column, solid lines) data of the superfluid fraction (top row) and normalized quasiparticle conductivity (bottom row) for all irradiation doses. Green arrows indicate the changes across the transition.

Figure 5.16 shows the experimental data in symbols in the left column and the calculated one in solid lines in the right column. The top row shows the superfluid fraction and the bottom row the normalized quasiparticle conductivity for all disorder levels. Despite the fact that it was possible to employ only an approximate two band model and not the more realistic three band one, the comparison is extremely satisfactory. All the qualitative behaviors are captured for the whole data set and also a semi-quantitative agreement is achieved .

It can be noted that the shape of the superfluid fraction curve changes drastically twice: after the first irradiation dose (from black to red), becoming more BCS-like due to the scattering induced increased band mixing, and after the transition from s_{\pm} to s_{++} state (indicated by the arrow) with the development of a long tale of low superfluid density at high temperature. Also the shape of the quasiparticle conductivity has two drastic changes. Pristine samples show a sharp, monotonous, increase of σ_n below T_c , while the irradiated system still in the s_{\pm} state have a qualitatively different shape. A large peak develops with a maximum between 15 and 17 K and the low temperature value of σ_n is strongly suppressed. When disorder drives the system in the s_{++} state a similar behavior to that of the pristine samples is surprisingly recovered, although with lower values that also keep decreasing with increasing disorder.

Here it should be noted that the quasiparticle conductivity at 8 GHz, although related, is not coincident with the optical conductivity studied by Schilling *et al.*[125] to trace the s_{\pm} to s_{++} transition. In their zero frequency case they observed a peak, that they attribute to coherence effects, at all levels of disorder. They argue that it is centered at a temperature proportional to the absolute value of the smallest gap. Instead, the quasiparticle conductivity peak develops only in the disordered s_{\pm} state and could be due to the competition between decreasing quasiparticle density and increasing quasiparticle scattering time and could be influenced by the operating frequency [176, 209].

In Figure 5.17, the 3D plots (left experimental data, right calculated) for the superfluid density (that is not normalized to the low temperature value) as a function of

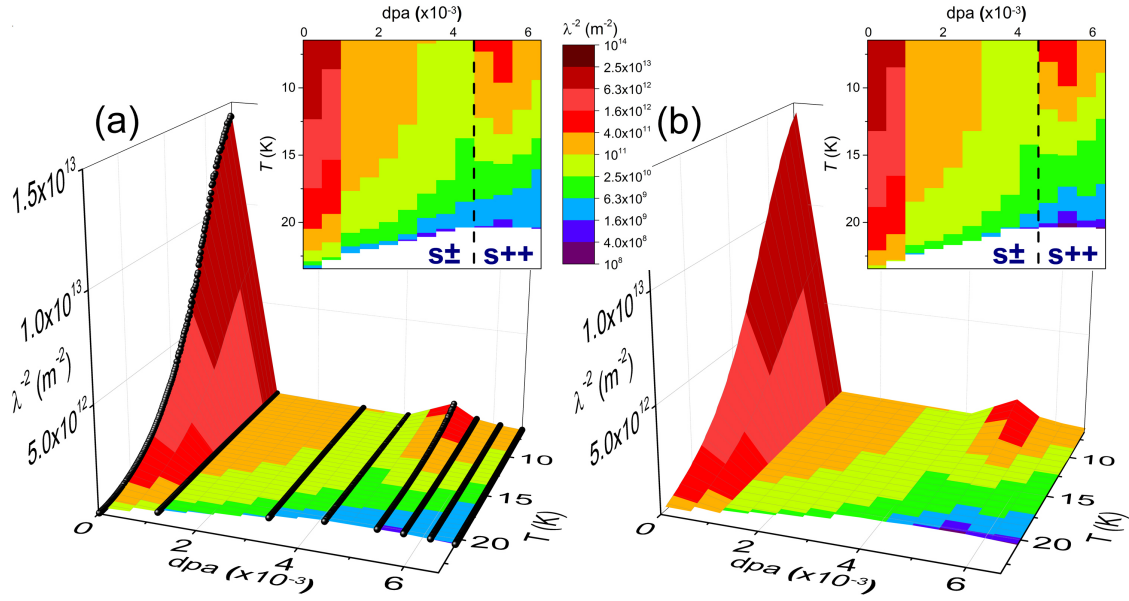


Figure 5.17: (a) Experimental data and (b) calculated data represented in a 3D surface plots and 2D color plots (insets) of λ_L^{-2} (proportional to the superfluid density) as a function of both temperature and disorder (dpa). In (a) the experimental data points are added as symbols to the surface plot. In the insets the s_{\pm} to s_{++} transition is identified with a dashed line. The same color scale has been used for all the graphs. Adapted from [126]. ©2018 American Physical Society.

both temperature and disorder level are shown, following the example of Ref. [125]. Also in this case the agreement is remarkable, testifying that the model reproduces very satisfactorily the experimental data.

With the good agreement between the calculated and measured data in mind, it is interesting to look at the behavior of the estimated gaps as a function of temperature and disorder, shown in Figure 5.18. Remarkably, at the level of scattering corresponding to the dpa at which the signatures of the s_{\pm} to s_{++} transition has been identified, the smallest gap changes sign realizing the s_{++} state. This is visible both on the imaginary-axis solutions on the left side of Figure 5.18, where also the temperature dependence is shown, and on the real-axis solutions at low temperature, presented on the right only as a function of disorder level. Interestingly, after the transition the gaps vary very little with increasing disorder, which is consistent with the observed T_c evolution.

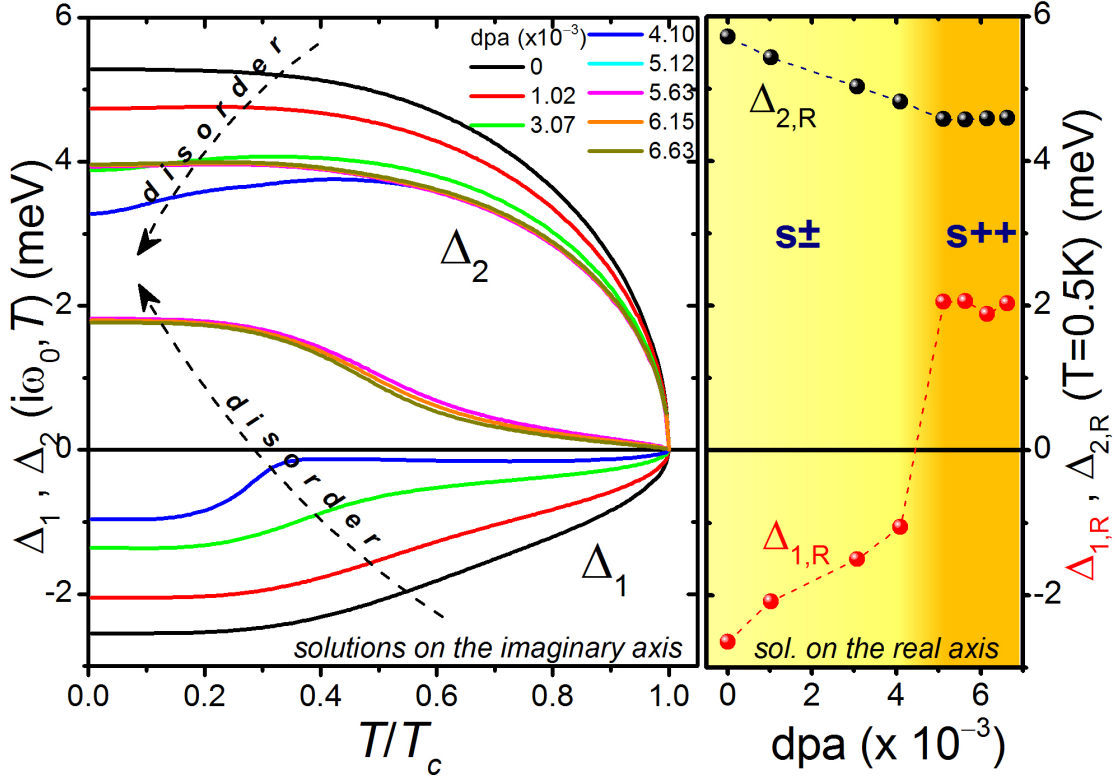


Figure 5.18: Left: imaginary axis solutions for the gaps as a function of temperature for the pristine sample (black lines) and after each irradiation dose (color lines). As the irradiation induced disorder increases the two gaps get closer in value and their temperature dependence is modified. Remarkably Δ_1 changes sign at the scattering value corresponding to the dpa at which $\lambda_L(0)$ drops. Right: Gaps values at low temperature from the real-axis Eliashberg equations as a function of disorder, expressed as dpa. The s_{\pm} and s_{++} phases are indicated by different background colors. Adapted from [126]. ©2018 American Physical Society.

At last, starting from the measured data it also possible to discuss the behavior of the surface impedance $Z_s = R_s + iX_s$ of the material across the symmetry transition. This is particularly relevant because this quantity can be measured by a larger variety of experimental techniques. Its real and imaginary parts are shown in Figure 5.19 both normalized to their values at T_c . In the normal state $R_s = X_s$ as expected in the regime of classical skin effect. Interestingly, the normalized surface resistance at low temperature increases monotonically with disorder, not showing any signature of the transition. Conversely, the reactance drops upon passing to the s_{++} state and develops a shoulder near $T = 15$ K.

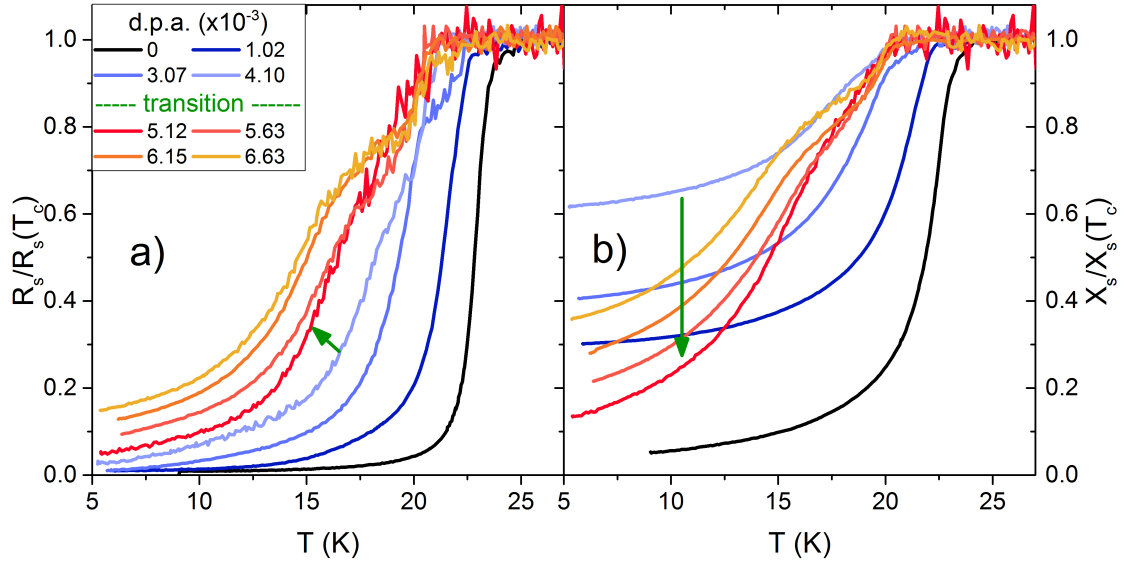


Figure 5.19: Temperature dependence of the normalized a) surface resistance (R_s) and b) reactance (X_s) for increasing dpa. The s_{\pm} to s_{++} disorder induced transition is indicated by the green arrows and takes place between $\text{d.p.a.} = 4.10 \times 10^{-3}$ and 5.12×10^{-3} . Adapted from [177]. ©2019 Springer Nature.

In summary, by studying the response of optimally doped $\text{Ba}(\text{Fe}_{1-x}\text{Rh}_x)_2\text{As}_2$ single crystals to the introduction of high levels of disorder, it was possible to identify (experimentally and with the support from Eliashberg analysis) the s_{\pm} to s_{++} order parameter symmetry transition in its signature in the low temperature superfluid density. Moreover, the possibility to measure at the same time the quasiparticle conductivity and then obtain the surface impedance made it possible to identify new hallmarks of this transition. Specifically a recovery of the monotonous evolution of the quasiparticle conductivity with temperature observed for the pristine sample and modified to a large peak in the disordered s_{\pm} state, a drop of the low temperature value of the surface reactance at the transition in contrast with the monotonous trend of the surface resistance, and the development of a shoulder below T_c in the surface impedance versus temperature curve.

Chapter 6

Conclusions

In this dissertation, a combined experimental and theoretical analysis of different IBSs was presented, with a particular focus on the effects of disorder on the superconducting properties.

Experimentally, the London penetration depth, quasiparticle conductivity and surface impedance as a function of temperature was measured for several single crystals of K, Co, Rh and P optimally doped Ba-122 and Ni doped CaK-1144 in the pristine state and upon introduction of disorder via ion irradiation.

Ion irradiation with several particles and energies was performed, as part of this PhD project, at the facilities of the Laboratori Nazionali di Legnaro of INFN and was guided by Monte Carlo simulations of the irradiation process performed with PHITS and SRIM codes.

Finally, the experimental data was analyzed within the framework of the multiband Eliashberg theory based on interaction provided by AFM-SF.

The first part of this work deals with the investigation of pristine single crystals of Ba-122 with different substitutional species (K, Co and P) covering hole and electron doping and isovalent substitution. This allowed to show that an Eliashberg model based on three bands and the s_{\pm} symmetry of the order parameter (induced by AFM-SF) is able to explain comprehensively a large set of experimental data (T_c , $\lambda_L(T)$, $\sigma_n(T)$, $\Delta_i(T = 0)$) for all possible types of chemical substitution of the parent compound. From the combination of experimental data and of calculation parameters it was possible to suggest that the modification of the superconducting FeAs planes by

chemical substitution could play a relevant role in the modification of superconducting properties, in addition to the straightforward effects of charge doping. Moreover, it has been possible to discuss the nature of a wide peak observed in the quasiparticle conductivity at microwave frequencies just below $T_c/2$ and the possible presence of nodes in the gap of the P optimally doped samples. The peak in $\sigma_n(T)$ is not due to coherence effects but rather emerges from a combination of quasiparticle scattering and temperature dependent depletion of carriers. The experimental data at 8 GHz is consistent with previous experiment in ruling out the existence of line nodes but it can not rule out nor confirm other accidental nodal structures such as loops [73].

The decrease of critical temperature with increasing irradiation doses of 3.5 MeV protons, 250 MeV Au ions and 1.2 GeV Pb ions was discussed, highlighting that neither fluence nor dpa are good parameters to compare the effects on the superconducting properties of different types of irradiation induced defects (point defects or correlated ones). This is due to the fact that energetic heavy ions produce defects distributions that are spatially correlated and that electronic stopping power plays a very important role in the damaging mechanism.

The effects of moderate levels of disorder introduced by 250 MeV Au ions in K doped Ba-122 samples were analyzed experimentally and with an Eliashberg model focused on the best representation possible of the material itself and that treated disorder within the Born approximation. With this approach it was possible to achieve a remarkable quantitative reproduction of the experimental London penetration depth down to small features [72]. Moreover, the electrodynamic response of the material was studied experimentally showing a temperature and disorder dependent peak in the surface reactance caused by a competition between the temperature dependence of the screening currents and of the carrier population [71].

The anisotropy of the London penetration depth was studied experimentally for undoped and Ni doped CaK-1144 samples in the pristine state and after irradiation with 3.5 MeV protons. It emerged that substitutional and irradiation induced disorder act on the anisotropy of IBSs in different ways: both making the system more isotropic but with opposite temperature dependences, possibly providing a way to tune the anisotropy as desired for specific applications.

Finally, the effects of elevated levels of disorder were investigated, experimentally and with an Eliashberg model focused on the accurate description of scattering, in Rh doped Ba-122 single crystals exposed to high doses of 3.5 MeV protons. In this case it was possible to identify for the first time the theoretically predicted s_{\pm} to s_{++} order parameter symmetry transition in its signature in the low temperature superfluid density. Moreover, new hallmarks of this transition were discovered in the quasiparticle conductivity evolution with temperature and in a drop of the low temperature value of the surface reactance [126, 177].

In summary, this work shows that the combination of microwave characterization of several superconducting properties with the possibility to reproduce all these data within the same Eliashberg model with a limited number of free parameters and to follow their evolution with disorder allows to reach a deeper insight in the fundamental properties of IBSs.

List of published papers

During this PhD project the following papers have been published on the topics discussed in this thesis:

- G. Ghigo, G. A. Ummarino, L. Gozzelino, R. Gerbaldo, F. Laviano, **D. Torsello** and T. Tamegai “Effects of disorder induced by heavy-ion irradiation on $(\text{Ba}_{1-x}\text{K}_x)\text{Fe}_2\text{As}_2$ single crystals, within the three-band Eliashberg s_{\pm} wave model.”, *Sci. Rep.* 7, 13029 (2017)
- G. Ghigo, **D. Torsello**, R. Gerbaldo, L. Gozzelino, F. Laviano, T. Tamegai “Effects of heavy-ion irradiation on the microwave surface impedance of $(\text{Ba}_{1-x}\text{K}_x)\text{Fe}_2\text{As}_2$ single crystals.” *Supercond. Sci. Technol.* 31, 034006 (2018)
- G. Sylva, E. Bellingeri, C. Ferdeghini, A. Martinelli, I. Pallecchi, L. Pellegrino, M. Putti, G. Ghigo, L. Gozzelino, **D. Torsello**, G. Grimaldi, A. Leo, A. Nigro and V. Braccini “Effects of high-energy proton irradiation on the superconducting properties of $\text{Fe}(\text{Se},\text{Te})$ thin films.” *Supercond. Sci. Technol.* 31 054001 (2018)
- G. Ghigo, **D. Torsello**, G. A. Ummarino, L. Gozzelino, M. A. Tanatar, R. Prozorov, and P. C. Canfield “Disorder-Driven Transition from s_{\pm} to s_{++} Superconducting Order Parameter in Proton Irradiated $\text{Ba}(\text{Fe}_{1-x}\text{Rh}_x)_2\text{As}_2$ Single Crystals.” *Phys. Rev. Lett.* 121, 107001 (2018)
- A. Leo, G. Sylva, V. Braccini, E. Bellingeri, A. Martinelli, I. Pallecchi, C. Ferdeghini, L. Pellegrino, M. Putti, G. Ghigo, L. Gozzelino, **D. Torsello**, S. Pace, A. Nigro, G. Grimaldi “Anisotropic Effect of Proton Irradiation on Pinning Properties of $\text{Fe}(\text{Se},\text{Te})$ Thin Films.” *IEEE Trans. Appl. Supercond.* 29, 8616884 (2019)
- **D. Torsello**, G. A. Ummarino, L. Gozzelino, T. Tamegai, G. Ghigo “Comprehensive Eliashberg analysis of microwave conductivity and penetration depth of K-, Co-, and P-substituted BaFe_2As_2 .” *Phys. Rev. B* 99, 134518 (2019)
- **D. Torsello**, R. Gerbaldo, L. Gozzelino, M. A. Tanatar, R. Prozorov, P. C. Canfield and G. Ghigo “Electrodynamical response of $\text{Ba}(\text{Fe}_{1-x}\text{Rh}_x)_2\text{As}_2$ across the s_{\pm} to s_{++} order parameter transition.” *Eur. Phys. J. Spec. Top.* 3, 228, 719 (2019)
- **D. Torsello**, K. Cho, K. R. Joshi, S. Ghimire, G. A. Ummarino, N. M. Nusran, M. A. Tanatar, W. R. Meier, M. Xu, S. L. Bud’ko, P. C. Canfield, G. Ghigo, and R. Prozorov

“Analysis of the London penetration depth in Ni-doped $\text{CaKFe}_4\text{As}_4$.” *Phys. Rev. B* 100, 094513 (2019)

- **D. Torsello**, G. Ummarino, R. Gerbaldo, L. Gozzelino and G. Ghigo “Eliashberg Analysis of the Electrodynamical Response of $\text{Ba}(\text{Fe}_{1-x}\text{Rh}_x)_2\text{As}_2$ Across the s_{\pm} to s_{++} Order Parameter Transition.” *J. Supercond. Nov. Magn.* (2019)

Furthermore, the following papers have been published on related topics out of the scope of the present discussion:

- **D. Torsello**, L. Mino, V. Bonino, A. Agostino, L. Operti, E. Borfecchia, E. Vittone, C. Lamberti, and M. Truccato “Monte Carlo analysis of the oxygen knock-on effects induced by synchrotron x-ray radiation in the $\text{Bi}_2\text{Sr}_2\text{CaCu}_2\text{O}_{8+\delta}$ superconductor.” *Phys. Rev. Materials* 2, 014801 (2018)
- L. Gozzelino, R. Gerbaldo, G. Ghigo, F. Laviano, **D. Torsello**, V. Bonino, M. Truccato, D. Batalu, M. A. Grigoroscuta, M. Burdusel, G. V. Aldica and P. Badica “Passive magnetic shielding by machinable MgB_2 bulks: measurements and numerical simulations” *Supercond. Sci. Technol.* 32, 034004 (2019)
- G. Ghigo, **D. Torsello**, L. Gozzelino, T. Tamegai, I. S. Veshchunov, S. Pyon, W. Jiao, G. H. Cao, S. Y. Grebenchuk, I. A. Golovchanskiy, V. S. Stolyarov, and D. Roditchev “Microwave analysis of the interplay between magnetism and superconductivity in $\text{EuFe}_2(\text{As}_{1-x}\text{P}_x)_2$ single crystals” *Phys. Rev. Research* 1, 033110 (2019)

Appendix A

Thin films

The effects induced by ion irradiation on thin films have a twofold origin: first there is the straightforward contribution from defects produced in the film by the passing ions, and second there is the contribution from the damage in the substrate that acts on the film through strain. To investigate the relative importance of these two contributions, a study on Fe(Se,Te) thin films grown on CaF₂ irradiated with 3.5 MeV protons was carried out in collaboration with CNR-SPIN and the universities of Genova and Salerno. In particular, different irradiation fluences up to $7.3 \times 10^{16} \text{ cm}^{-2}$ were used and the proton implantation depth in the substrate was modulated in some samples by the interposition of an Al foil that was 80 μm thick. The modifications on critical temperature, normal state resistivity, critical current and strain level were investigated.

FeSe_{0.5}Te_{0.5} thin films were deposited epitaxially on oriented 001 CaF₂ by pulsed laser deposition by the group of Prof. Putti in Genova [211]. Five films 100 nm thick were studied: three of them (samples A, B, and C) were patterned, through standard optical photolithography and Ar ion milling etching, in the shape of nine Hall bar microbridges each, for transport measurements; whereas the other two (samples D and E) were analysed with X-ray diffraction to study the strain level.

The irradiation experiment was guided by Monte Carlo simulations with the PHITS [143] and SRIM [142] codes that allowed to determine the deceleration of the ions caused by the interposition of the Al foil, the damage level (dpa) induced in the Fe(Se,Te) film and the implantation depth of the protons in the substrate (see Fig. A.1

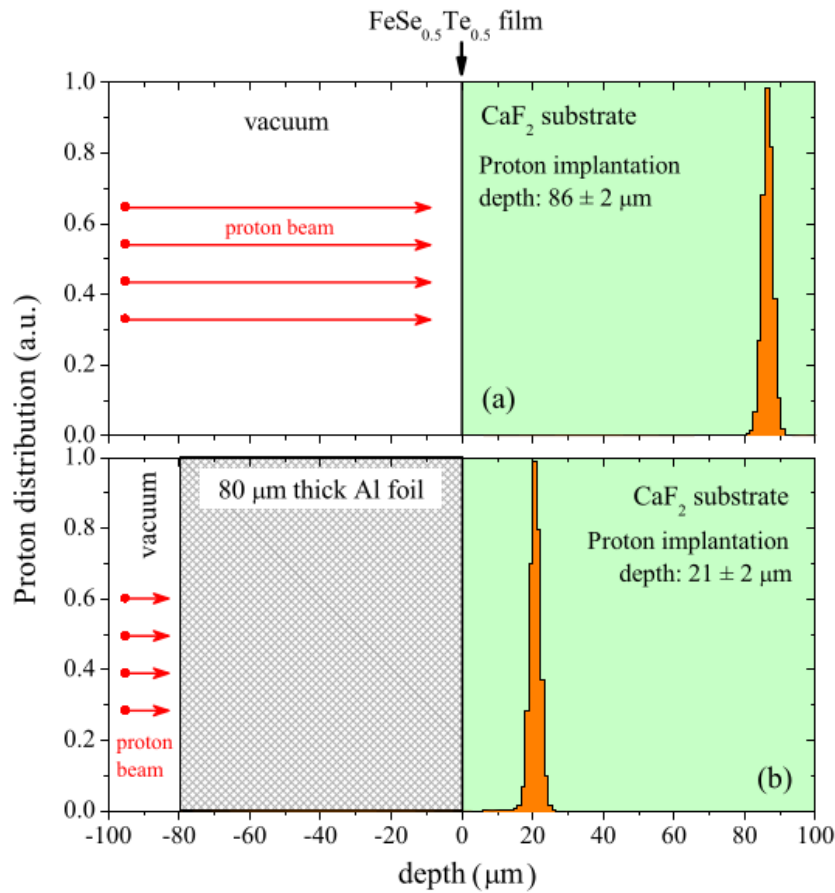


Figure A.1: Implantation depth of protons (histograms) in the substrate (right regions) for the case without (a) and with (b) the Al foil interposed. On the left side of the picture a scheme of the irradiation experiment is shown. Adapted from [210]. ©2018 IOP Publishing.

for the scheme and estimate of the implantation depth and Table A.1 for a summary of the irradiation parameters.).

Samples D and E were analysed at the University of Genova by means of the X-ray diffraction Williamson–Hall plot method [212] to determine the level of lattice microstrain in the film along the $[00l]$ crystallographic planes. This method consists in the analysis of the breadth of the diffraction line as a function of the reciprocal interplanar spacing: they have a linear dependence and the slope of the plot is proportional to the microstrain. It resulted that the the two pristine samples, as expected, have similar

Table A.1: Summary of the studied samples and the details of irradiation: presence of the interposed Al screen, irradiation fluence, average dpa introduced in the superconducting film. Samples A, B, and C were patterned for transport measurements whereas samples D and E were used for X-ray diffraction analysis.

Sample	Hall bar identifier	Al screen	Irradiation fluence (cm^{-2})	dpa $\times 10^{-3}$
A	A_0	-	0	0
A	A_0.25	NO	0.7×10^{16}	0.25
A	A_0.99	NO	2.8×10^{16}	9.9
B	B_0	-	0	0
B	B_0.69	NO	1.95×10^{16}	0.69
B	B_2.27	NO	6.40×10^{16}	2.27
B	B_2.59	NO	7.30×10^{16}	2.59
C	C_0	-	0	0
C	C_2.30	YES	2.68×10^{16}	2.30
C	C_4.59	YES	5.35×10^{16}	4.59
D	-	-	0	0
D	-	YES	2.68	2.30
D	-	YES	5.35	4.59
E	-	-	0	0
E	-	NO	5.35	1.90

amount of lattice strain, but as a consequence of the two irradiation processes they display opposite behaviours. Sample E, for which the ions implanted deeper into the substrate, exhibits a decrease in strain levels, conversely the strain in sample D (implantation near the interface between substrate and sample) increases progressively with the irradiation dose.

With these results in mind one can look at the behavior of the transport properties of

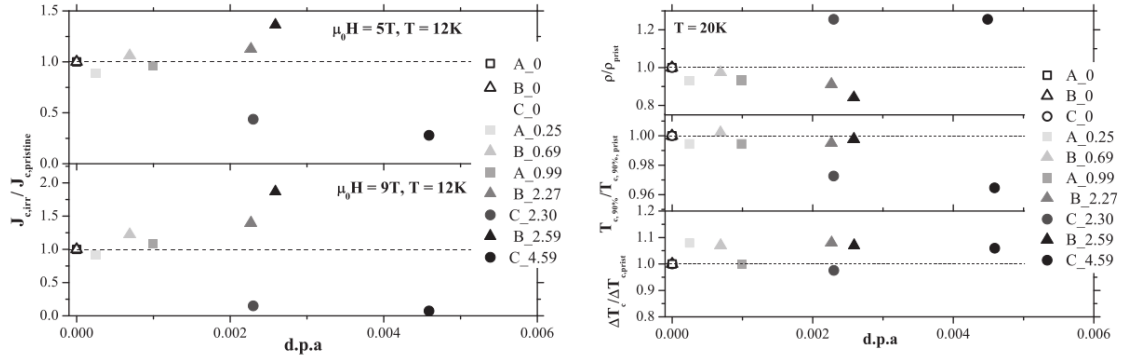


Figure A.2: Left panel: critical current of the irradiated bars normalised to their pristine values at 12 K and 9 T (lower panel) and 5 T (upper panel). Right panel: resistivity at 20 K (in the normal state) (top panel), critical temperature (intermediate panel), and transition width (bottom panel) as functions of d.p.a all normalised to their pristine value. Adapted from [210]. ©2018 IOP Publishing.

samples A (squares), B (triangles) and C (circles) shown in Fig. A.2. Transport measurements were carried out at the Universities of Salerno and Genova with a standard four probe, current biased technique, and critical current values were extracted from voltage versus current characteristics. As shown in Table A.1, samples A and B were irradiated directly by 3.5 MeV protons whereas sample C with the interposed Al foil. Therefore the implanted region in sample C is closer to the the interface between the superconducting film and the substrate, corresponding to higher microstrain levels in the film as emerged from X-ray analysis. It is evident that sample C has a completely different response to irradiation from samples A and B, even if the same dpa is introduced in the film. Its critical current J_c decreases with irradiation whereas it increases for samples A and B, its critical temperature has a stronger degradation than the other samples while the T_c broadenings are consistent, and also the resistivity above T_c has a strong increase. From these observations it is possible to conclude that, although Fe(Se,Te) by itself is more robust against irradiation than other superconductors such as the cuprates (making it interesting for applications in radiation harsh environments, *e. g.* accelerators), the delicate interplay between the film itself and the substrate needs to be carefully addressed for each application. A possibility to suppress these unwanted effects could be the use of more elastic substrates such as metallic ones.

Nomenclature

μ SR Muon Spin Rotation

AFM AntiFerroMagnetic

ARPES Angle Resolved PhotoEmission Spectroscopy

BCS Bardeen-Cooper-Schrieffer

CPWR CoPlanar Waveguide Resonator

DFT Density Functional Theory

dpa displacement per atom

FS Fermi Surface

IBS Iron Based Superconductor

INFN Istituto Nazionale di Fisica Nucleare

LNL Laboratori Nazionali di Legnaro

NMR Nuclear Magnetic Resonance

NV Nitrogen-Vacancy

ODMR Optically Detected Magnetic Resonance

PM ParaMagnetic

QCP Quantum Critical Point

SDW Spin Density Wave

Nomenclature

SF Spin Fluctuations

TDR Tunnel Diode Resonator

TEM Transmission Electron Microscopy

Bibliography

1. Bardeen, J., Cooper, L. N. & Schrieffer, J. R. Theory of Superconductivity. *Phys. Rev.* **108**, 1175–1204 (5 Dec. 1957).
2. Stewart, G. R. Heavy-fermion systems. *Rev. Mod. Phys.* **56**, 755–787 (4 Oct. 1984).
3. Bednorz, J. G. & Müller, K. A. Possible highTc superconductivity in the Ba–La–Cu–O system. *Zeitschrift für Physik B Condensed Matter* **64**, 189–193. ISSN: 1431-584X (June 1986).
4. Tsuei, C. C. & Kirtley, J. R. Pairing symmetry in cuprate superconductors. *Rev. Mod. Phys.* **72**, 969–1016 (4 Oct. 2000).
5. Monthoux, P. & Scalapino, D. J. Self-consistent $d_x^2-y^2$ pairing in a two-dimensional Hubbard model. *Phys. Rev. Lett.* **72**, 1874–1877 (12 Mar. 1994).
6. Nagamatsu, J., Nakagawa, N., Muranaka, T., Zenitani, Y. & Akimitsu, J. Superconductivity at 39 K in magnesium diboride. *nature* **410**, 63 (2001).
7. Liu, A. Y., Mazin, I. I. & Kortus, J. Beyond Eliashberg Superconductivity in MgB_2 : Anharmonicity, Two-Phonon Scattering, and Multiple Gaps. *Phys. Rev. Lett.* **87**, 087005 (8 Aug. 2001).
8. Szabó, P. *et al.* Evidence for Two Superconducting Energy Gaps in MgB_2 by Point-Contact Spectroscopy. *Phys. Rev. Lett.* **87**, 137005 (13 Sept. 2001).
9. Yoichi, K., Takumi, W., Masahiro, H. & Hidei, H. Iron-based layered superconductor $\text{La}[\text{O}_{1-x}\text{Fx}]\text{FeAs}$ ($x = 0.05\text{--}0.12$) with $T_c = 26$ K. *J. Am. Chem. Soc.* **130**, 3296–3297 (2008).
10. Kamihara, Y. *et al.* Iron-Based Layered Superconductor: LaOFeP . *Journal of the American Chemical Society* **128**. PMID: 16881620, 10012–10013 (2006).

11. Putti, M. *et al.* New Fe-based superconductors: properties relevant for applications. *Superconductor Science and Technology* **23**, 034003 (Feb. 2010).
12. Mazin, I. I., Singh, D. J., Johannes, M. D. & Du, M. H. Unconventional Superconductivity with a Sign Reversal in the Order Parameter of $\text{LaFeAsO}_{1-x}\text{F}_x$. *Phys. Rev. Lett.* **101**, 057003 (5 July 2008).
13. Chubukov, A. V., Efremov, D. V. & Eremin, I. Magnetism, superconductivity, and pairing symmetry in iron-based superconductors. *Phys. Rev. B* **78**, 134512 (13 Oct. 2008).
14. Stanev, V., Kang, J. & Tesanovic, Z. Spin fluctuation dynamics and multiband superconductivity in iron pnictides. *Phys. Rev. B* **78**, 184509 (18 Nov. 2008).
15. Hirschfeld, P. J., Korshunov, M. M. & Mazin, I. I. Gap symmetry and structure of Fe-based superconductors. *Reports on Progress in Physics* **74**, 124508 (Oct. 2011).
16. Ren, Z. *et al.* Superconductivity Induced by Phosphorus Doping and Its Coexistence with Ferromagnetism in $\text{EuFe}_2(\text{As}_{0.7}\text{P}_{0.3})_2$. *Phys. Rev. Lett.* **102**, 137002 (13 Apr. 2009).
17. Bang, Y. & Stewart, G. R. Superconducting properties of the \pm -wave state: Fe-based superconductors. *Journal of Physics: Condensed Matter* **29**, 123003 (Feb. 2017).
18. Ding, H. *et al.* Electronic structure of optimally doped pnictide $\text{Ba}_{0.6}\text{K}_{0.4}\text{Fe}_2\text{As}_2$: a comprehensive angle-resolved photoemission spectroscopy investigation. *Journal of Physics: Condensed Matter* **23**, 135701 (Mar. 2011).
19. Allan, M. P. *et al.* Anisotropic Energy Gaps of Iron-Based Superconductivity from Intraband Quasiparticle Interference in LiFeAs . *Science* **336**, 563–567. ISSN: 0036-8075 (2012).
20. Parker, D., Vavilov, M. G., Chubukov, A. V. & Mazin, I. I. Coexistence of superconductivity and a spin-density wave in pnictide superconductors: Gap symmetry and nodal lines. *Phys. Rev. B* **80**, 100508 (10 Sept. 2009).
21. Yamakawa, Y. & Kontani, H. Quasiparticle interference in Fe-based superconductors based on a five-orbital tight-binding model. *Phys. Rev. B* **92**, 045124 (4 July 2015).

22. Zhang, C. *et al.* Distinguishing s^\pm and s^{++} electron pairing symmetries by neutron spin resonance in superconducting $\text{NaFe}_{0.935}\text{Co}_{0.045}\text{As}$. *Phys. Rev. B* **88**, 064504 (6 Aug. 2013).
23. Wang, Y., Kreisel, A., Hirschfeld, P. J. & Mishra, V. Using controlled disorder to distinguish s_\pm and s_{++} gap structure in Fe-based superconductors. *Phys. Rev. B* **87**, 094504 (9 Mar. 2013).
24. Efremov, D. V., Korshunov, M. M., Dolgov, O. V., Golubov, A. A. & Hirschfeld, P. J. Disorder-induced transition between s_\pm and s_{++} states in two-band superconductors. *Phys. Rev. B* **84**, 180512 (18 Nov. 2011).
25. Paglione, J. & Greene, R. L. High-temperature superconductivity in iron-based materials. *Nature physics* **6**, 645 (2010).
26. Mazin, I. & Schmalian, J. Pairing symmetry and pairing state in ferropnictides: Theoretical overview. *Physica C: Superconductivity* **469**. Superconductivity in Iron-Pnictides, 614–627. ISSN: 0921-4534 (2009).
27. Canfield, P. C. & Bud'ko, S. L. FeAs-Based Superconductivity: A Case Study of the Effects of Transition Metal Doping on BaFe_2As_2 . *Annual Review of Condensed Matter Physics* **1**, 27–50 (2010).
28. Rotter, M., Tegel, M. & Johrendt, D. Superconductivity at 38 K in the Iron Arsenide $(\text{Ba}_{1-x}\text{K}_x)\text{Fe}_2\text{As}_2$. *Phys. Rev. Lett.* **101**, 107006 (10 Sept. 2008).
29. Iyo, A. *et al.* New-Structure-Type Fe-Based Superconductors: $\text{CaAFe}_4\text{As}_4$ ($A = \text{K}, \text{Rb}, \text{Cs}$) and $\text{SrAFe}_4\text{As}_4$ ($A = \text{Rb}, \text{Cs}$). *Journal of the American Chemical Society* **138**. PMID: 26943024, 3410–3415 (2016).
30. Ding, Q.-P. *et al.* Hedgehog Spin-Vortex Crystal Antiferromagnetic Quantum Criticality in $\text{CaK}(\text{Fe}_{1-x}\text{Ni}_x)_4\text{As}_4$ Revealed by NMR. *Phys. Rev. Lett.* **121**, 137204 (13 Sept. 2018).
31. Kreyssig, A. *et al.* Antiferromagnetic order in $\text{CaK}(\text{Fe}_{1-x}\text{Ni}_x)_4\text{As}_4$ and its interplay with superconductivity. *Phys. Rev. B* **97**, 224521 (22 June 2018).
32. Meier, W. R. *et al.* Hedgehog spin-vortex crystal stabilized in a hole-doped iron-based superconductor. *npj Quantum Materials* **3**, 5 (2018).
33. Rotter, M. *et al.* Spin-density-wave anomaly at 140 K in the ternary iron arsenide BaFe_2As_2 . *Phys. Rev. B* **78**, 020503 (2 July 2008).

34. Sefat, A. S. *et al.* Superconductivity at 22 K in Co-Doped BaFe₂As₂ Crystals. *Phys. Rev. Lett.* **101**, 117004 (11 Sept. 2008).
35. Jiang, S. *et al.* Superconductivity up to 30 K in the vicinity of the quantum critical point in BaFe₂(As_{1-x}P_x)₂. *Journal of Physics: Condensed Matter* **21**, 382203 (Aug. 2009).
36. Mani, A., Ghosh, N., Paulraj, S., Bharathi, A. & Sundar, C. S. Pressure-induced superconductivity in BaFe₂As₂ single crystal. *EPL (Europhysics Letters)* **87**, 17004 (July 2009).
37. Lu, D. *et al.* Electronic structure of the iron-based superconductor LaOFeP. *Nature* **455**, 81 (2008).
38. Wang, X. *et al.* The superconductivity at 18 K in LiFeAs system. *Solid State Communications* **148**, 538–540. ISSN: 0038-1098 (2008).
39. Hashimoto, K. *et al.* A Sharp Peak of the Zero-Temperature Penetration Depth at Optimal Composition in BaFe₂(As_{1-x}P_x)₂. *Science* **336**, 1554–1557. ISSN: 0036-8075 (2012).
40. Ding, H. *et al.* Observation of Fermi-surface-dependent nodeless superconducting gaps in Ba_{0.6}K_{0.4}Fe₂As₂. *EPL (Europhysics Letters)* **83**, 47001 (July 2008).
41. Terashima, K. *et al.* Fermi surface nesting induced strong pairing in iron-based superconductors. *Proceedings of the National Academy of Sciences* **106**, 7330–7333. ISSN: 0027-8424 (2009).
42. Ye, Z. R. *et al.* Doping dependence of the electronic structure in phosphorus-doped ferropnictide superconductor BaFe₂(As_{1-x}P_x)₂ studied by angle-resolved photoemission spectroscopy. *Phys. Rev. B* **86**, 035136 (3 July 2012).
43. Yoshida, T. *et al.* Anisotropy of the superconducting gap in the iron-based superconductor BaFe₂(As_{1-x}P_x)₂. *Scientific reports* **4**, 7292 (2014).
44. Ouahab, A., Hassaine, I. & Boukraa, A. A Structural and Electronic Properties DFT Study of BaFe₂As₂ and Two Derived Substitution Compounds. *Journal of Superconductivity and Novel Magnetism* **26**, 2403–2409. ISSN: 1557-1947 (July 2013).
45. Sandoghchi, M., Khosroabadi, H. & Akhavan, M. Effects of K doping on electronic structure of Ba_{1-x}K_xFe₂As₂ superconductor by ab-initio density functional theory. *Physica C: Superconductivity and its Applications* **507**, 22–24. ISSN: 0921-4534 (2014).

46. Miyake, T., Nakamura, K., Arita, R. & Imada, M. Comparison of Ab initio Low-Energy Models for LaFePO, LaFeAsO, BaFe₂As₂, LiFeAs, FeSe, and FeTe: Electron Correlation and Covalency. *Journal of the Physical Society of Japan* **79**, 044705 (2010).
47. Tamai, A. *et al.* Strong Electron Correlations in the Normal State of the Iron-Based FeSe_{0.42}Te_{0.58} Superconductor Observed by Angle-Resolved Photoemission Spectroscopy. *Phys. Rev. Lett.* **104**, 097002 (9 Mar. 2010).
48. Aktürk, E. & Ciraci, S. First-principles study of the iron pnictide superconductor BaFe₂As₂. *Phys. Rev. B* **79**, 184523 (18 May 2009).
49. Shafiei, M., Khosroabadi, H. & Akhavan, M. First-Principle Electronic Structure Calculation of BaFe_{2-x}CoxAs₂(x = 0, 1, 2) Superconductor. *Journal of Superconductivity and Novel Magnetism* **28**, 2249–2254. ISSN: 1557-1947 (Aug. 2015).
50. Singh, D. Electronic structure of Fe-based superconductors. *Physica C: Superconductivity* **469**. Superconductivity in Iron-Pnictides, 418–424. ISSN: 0921-4534 (2009).
51. Garbarino, G. *et al.* Direct observation of the influence of the As-Fe-As angle on the T_c of superconducting SmFeAsO_{1-x}F_x. *Phys. Rev. B* **84**, 024510 (2 July 2011).
52. Kuroki, K. *et al.* Unconventional Pairing Originating from the Disconnected Fermi Surfaces of Superconducting LaFeAsO_{1-x}F_x. *Phys. Rev. Lett.* **101**, 087004 (8 Aug. 2008).
53. Shirage, P. M. *et al.* Absence of an Appreciable Iron Isotope Effect on the Transition Temperature of the Optimally Doped SmFeAsO_{1-y} Superconductor. *Phys. Rev. Lett.* **105**, 037004 (3 July 2010).
54. Shirage, P. M. *et al.* Inverse Iron Isotope Effect on the Transition Temperature of the (Ba, K)Fe₂As₂ Superconductor. *Phys. Rev. Lett.* **103**, 257003 (25 Dec. 2009).
55. Boeri, L., Calandra, M., Mazin, I. I., Dolgov, O. V. & Mauri, F. Effects of magnetism and doping on the electron-phonon coupling in BaFe₂As₂. *Phys. Rev. B* **82**, 020506 (2 July 2010).
56. Liu, R. *et al.* A large iron isotope effect in SmFeAsO_{1-x}F_x and Ba_{1-x}K_xFe₂As₂. *Nature* **459**, 64 (2009).

57. Carlo, J. P. *et al.* Static Magnetic Order and Superfluid Density of $R\text{FeAs}(\text{O}, \text{F})$ ($R = \text{La}, \text{Nd}, \text{Ce}$) and LaFePO Studied by Muon Spin Relaxation: Unusual Similarities with the Behavior of Cuprate Superconductors. *Phys. Rev. Lett.* **102**, 087001 (8 Feb. 2009).
58. Qazilbash, M. *et al.* Electronic correlations in the iron pnictides. *Nature Physics* **5**, 647 (2009).
59. Korshunov, M., Shestakov, V. & Togushova, Y. Comparison of experimental data on the spin resonance frequency and gap magnitudes in Fe-based superconductors. *Journal of Magnetism and Magnetic Materials* **440**, 133–135. ISSN: 0304-8853 (2017).
60. Fröhlich, H. Theory of the Superconducting State. I. The Ground State at the Absolute Zero of Temperature. *Phys. Rev.* **79**, 845–856 (5 Sept. 1950).
61. Wang, X. F. *et al.* Anisotropy in the Electrical Resistivity and Susceptibility of Superconducting BaFe_2As_2 Single Crystals. *Phys. Rev. Lett.* **102**, 117005 (11 Mar. 2009).
62. Bonville, P., Rullier-Albenque, F., Colson, D. & Forget, A. Incommensurate spin density wave in Co-doped BaFe_2As_2 . *EPL (Europhysics Letters)* **89**, 67008 (Mar. 2010).
63. Ning, F. L. *et al.* Contrasting Spin Dynamics between Underdoped and Overdoped $\text{Ba}(\text{Fe}_{1-x}\text{Co}_x)_2\text{As}_2$. *Phys. Rev. Lett.* **104**, 037001 (3 Jan. 2010).
64. Shishido, H. *et al.* Evolution of the Fermi Surface of $\text{BaFe}_2(\text{As}_{1-x}\text{P}_x)_2$ on Entering the Superconducting Dome. *Phys. Rev. Lett.* **104**, 057008 (5 Feb. 2010).
65. Kontani, H. & Onari, S. Orbital-Fluctuation-Mediated Superconductivity in Iron Pnictides: Analysis of the Five-Orbital Hubbard-Holstein Model. *Phys. Rev. Lett.* **104**, 157001 (15 Apr. 2010).
66. Onari, S., Kontani, H. & Sato, M. Structure of neutron-scattering peaks in both s_{++} -wave and s_{\pm} -wave states of an iron pnictide superconductor. *Phys. Rev. B* **81**, 060504 (6 Feb. 2010).
67. Saito, T., Onari, S. & Kontani, H. Orbital fluctuation theory in iron pnictides: Effects of As-Fe-As bond angle, isotope substitution, and Z^2 -orbital pocket on superconductivity. *Phys. Rev. B* **82**, 144510 (14 Oct. 2010).

68. Xu, C., Müller, M. & Sachdev, S. Ising and spin orders in the iron-based superconductors. *Phys. Rev. B* **78**, 020501 (2 July 2008).
69. Krüger, F., Kumar, S., Zaanen, J. & van den Brink, J. Spin-orbital frustrations and anomalous metallic state in iron-pnictide superconductors. *Phys. Rev. B* **79**, 054504 (5 Feb. 2009).
70. Lee, C.-C., Yin, W.-G. & Ku, W. Ferro-Orbital Order and Strong Magnetic Anisotropy in the Parent Compounds of Iron-Pnictide Superconductors. *Phys. Rev. Lett.* **103**, 267001 (26 Dec. 2009).
71. Ghigo, G. *et al.* Effects of heavy-ion irradiation on the microwave surface impedance of $(\text{Ba}_{1-x}\text{K}_x)\text{Fe}_2\text{As}_2$ single crystals. *Superconductor Science and Technology* **31**, 034006 (Feb. 2018).
72. Ghigo, G. *et al.* Effects of disorder induced by heavy-ion irradiation on $(\text{Ba}_{1-x}\text{K}_x)\text{Fe}_2\text{As}_2$ single crystals, within the three-band Eliashberg s_{\pm} wave model. *Scientific reports* **7**, 13029 (2017).
73. Torsello, D., Ummarino, G. A., Gozzelino, L., Tamegai, T. & Ghigo, G. Comprehensive Eliashberg analysis of microwave conductivity and penetration depth of K-, Co-, and P-substituted BaFe_2As_2 . *Phys. Rev. B* **99**, 134518 (13 Apr. 2019).
74. Torsello, D. *et al.* Analysis of the London penetration depth in Ni-doped $\text{CaKFe}_4\text{As}_4$. *Phys. Rev. B* **100**, 094513 (9 Sept. 2019).
75. Emery, V. & Kivelson, S. Importance of phase fluctuations in superconductors with small superfluid density. *Nature* **374**, 434 (1995).
76. Pronin, A. V., Pimenov, A., Loidl, A. & Krasnosvobodtsev, S. I. Optical Conductivity and Penetration Depth in MgB_2 . *Phys. Rev. Lett.* **87**, 097003 (9 Aug. 2001).
77. Sonier, J. E., Brewer, J. H. & Kiefl, R. F. μSR studies of the vortex state in type-II superconductors. *Rev. Mod. Phys.* **72**, 769–811 (3 July 2000).
78. Luan, L. *et al.* Local measurement of the penetration depth in the pnictide superconductor $\text{Ba}(\text{Fe}_{0.95}\text{Co}_{0.05})_2\text{As}_2$. *Phys. Rev. B* **81**, 100501 (10 Mar. 2010).
79. Joshi, K. *et al.* Measuring the Lower Critical Field of Superconductors Using Nitrogen-Vacancy Centers in Diamond Optical Magnetometry. *Phys. Rev. Applied* **11**, 014035 (1 Jan. 2019).

80. Sridhar, S. & Kennedy, W. L. Novel technique to measure the microwave response of high Tc superconductors between 4.2 and 200 K. *Review of Scientific Instruments* **59**, 531–536 (1988).
81. Bonn, D. A., Morgan, D. C. & Hardy, W. N. Split-ring resonators for measuring microwave surface resistance of oxide superconductors. *Review of Scientific Instruments* **62**, 1819–1823 (1991).
82. Ghigo, G., Ummarino, G. A., Gozzelino, L. & Tamegai, T. Penetration depth of $Ba_{1-x}K_xFe_2As_2$ single crystals explained within a multiband Eliashberg $s \pm$ approach. *Phys. Rev. B* **96**, 014501 (1 July 2017).
83. Ghigo, G., Gerbaldo, R., Gozzelino, L., Laviano, F. & Tamegai, T. Penetration Depth and Quasiparticle Conductivity of Co- and K-Doped BaFe₂As₂ Crystals, Investigated by a Microwave Coplanar Resonator Technique. *IEEE Transactions on Applied Superconductivity* **26**, 1–4. ISSN: 1051-8223 (Apr. 2016).
84. <https://www.theva.com>.
85. Ghigo, G., Laviano, F., Gerbaldo, R. & Gozzelino, L. Tuning the response of YBCO microwave resonators by heavy-ion patterned micro-channels. *Superconductor Science and Technology* **25**, 115007 (Sept. 2012).
86. Vendik, I. *High temperature superconductor devices for microwave signal processing - Part II* ISBN: 5-89028-002-3 (Skladen Co, St. Petersburg, 1997).
87. Chen, L.-F., Ong, C., Neo, C., Varadan, V. & Varadan, V. K. *Microwave electronics: measurement and materials characterization* (John Wiley & Sons, 2004).
88. Vendik, I. Phenomenological model of the microwave surface impedance of high-Tc superconducting films. *Superconductor Science and Technology* **13**, 974–982 (June 2000).
89. Prozorov, R. & Kogan, V. G. London penetration depth in iron-based superconductors. *Reports on Progress in Physics* **74**, 124505 (Sept. 2011).
90. Hirschfeld, P. J. & Goldenfeld, N. Effect of strong scattering on the low-temperature penetration depth of a d-wave superconductor. *Phys. Rev. B* **48**, 4219–4222 (6 Aug. 1993).
91. Kogan, V. G., Prozorov, R. & Mishra, V. London penetration depth and pair breaking. *Phys. Rev. B* **88**, 224508 (22 Dec. 2013).

-
92. Wang, C. G. *et al.* Electron Mass Enhancement near a Nematic Quantum Critical Point in $\text{NaFe}_{1-x}\text{Co}_x\text{As}$. *Phys. Rev. Lett.* **121**, 167004 (16 Oct. 2018).
 93. Almoalem, A. *et al.* Dependence of the absolute value of the penetration depth in $(\text{Ba}_{1-x}\text{K}_x)\text{Fe}_2\text{As}_2$ on doping. *Phys. Rev. B* **98**, 054516 (5 Aug. 2018).
 94. Lamhot, Y. *et al.* Local characterization of superconductivity in $\text{BaFe}_2(\text{As}_{1-x}\text{P}_x)_2$. *Phys. Rev. B* **91**, 060504 (6 Feb. 2015).
 95. Kim, H., Tanatar, M. A. & Prozorov, R. Tunnel diode resonator for precision magnetic susceptibility measurements in a mK temperature range and large DC magnetic fields. *Review of Scientific Instruments* **89**, 094704 (2018).
 96. Van Degrift, C. T. Tunnel diode oscillator for 0.001 ppm measurements at low temperatures. *Review of Scientific Instruments* **46**, 599–607 (1975).
 97. Cho, K. *et al.* Precision global measurements of London penetration depth in $\text{FeTe}_{0.58}\text{Se}_{0.42}$. *Phys. Rev. B* **84**, 174502 (17 Nov. 2011).
 98. Kim, H. *et al.* London penetration depth and superfluid density of single-crystalline $\text{Fe}_{1+y}(\text{Te}_{1-x}\text{Se}_x)$ and $\text{Fe}_{1+y}(\text{Te}_{1-x}\text{S}_x)$. *Phys. Rev. B* **81**, 180503 (18 May 2010).
 99. Prozorov, R. & Kogan, V. G. Effective Demagnetizing Factors of Diamagnetic Samples of Various Shapes. *Phys. Rev. Applied* **10**, 014030 (1 July 2018).
 100. Hu, C.-R. Numerical Constants for Isolated Vortices in Superconductors. *Phys. Rev. B* **6**, 1756–1760 (5 Sept. 1972).
 101. Casola, F., van der Sar, T. & Yacoby, A. Probing condensed matter physics with magnetometry based on nitrogen-vacancy centres in diamond. *Nature Reviews Materials* **3**, 17088 (2018).
 102. Fletcher, J. D., Carrington, A., Taylor, O. J., Kazakov, S. M. & Karpinski, J. Temperature-Dependent Anisotropy of the Penetration Depth and Coherence Length of MgB_2 . *Phys. Rev. Lett.* **95**, 097005 (9 Aug. 2005).
 103. Kogan, V. G. Macroscopic anisotropy in superconductors with anisotropic gaps. *Phys. Rev. B* **66**, 020509 (2 July 2002).
 104. Kogan, V. G. & Prozorov, R. Effect of equatorial line nodes on the upper critical field and London penetration depth. *Phys. Rev. B* **90**, 100507 (10 Sept. 2014).

105. Van der Beek, C. J., Konczykowski, M. & Prozorov, R. Anisotropy of strong pinning in multi-band superconductors. *Superconductor Science and Technology* **25**, 084010 (July 2012).
106. Korshunov, M. M., Togushova, Y. N. & Dolgov, O. V. Impurities in multiband superconductors. *Physics-Uspekhi* **59**, 1211–1240 (Dec. 2016).
107. Eisterer, M. Radiation effects on iron-based superconductors. *Superconductor Science and Technology* **31**, 013001 (Dec. 2017).
108. Tamegai, T. *et al.* Effects of particle irradiations on vortex states in iron-based superconductors. *Superconductor Science and Technology* **25**, 084008 (July 2012).
109. Putti, M., Vaglio, R. & Rowell, J. M. Radiation effects on MgB₂: a review and a comparison with A15 superconductors. *Superconductor Science and Technology* **21**, 043001 (Feb. 2008).
110. Rehn, L. Ion beams in high-temperature superconductivity research. *Nuclear Instruments and Methods in Physics Research Section B: Beam Interactions with Materials and Atoms* **64**, 161–168. ISSN: 0168-583X (1992).
111. Civale, L. *et al.* Vortex confinement by columnar defects in YBa₂Cu₃O₇ crystals: Enhanced pinning at high fields and temperatures. *Phys. Rev. Lett.* **67**, 648–651 (5 July 1991).
112. Kwok, W.-K. *et al.* Vortices in high-performance high-temperature superconductors. *Reports on Progress in Physics* **79**, 116501 (Sept. 2016).
113. Spina, T. *et al.* Correlation Between the Number of Displacements Per Atom and T_c After High-Energy Irradiations of Nb₃Sn Wires for the HL-LHC. *IEEE Transactions on Applied Superconductivity* **26**, 1–5. ISSN: 1051-8223 (Apr. 2016).
114. Prokopec, R., Fischer, D. X., Weber, H. W. & Eisterer, M. Suitability of coated conductors for fusion magnets in view of their radiation response. *Superconductor Science and Technology* **28**, 014005 (Dec. 2014).
115. Civale, L. Vortex pinning and creep in high-temperature superconductors with columnar defects. *Superconductor Science and Technology* **10**, A11–A28 (July 1997).
116. Mezzetti, E. *et al.* Control of the critical current density in YBa₂Cu₃O_{7-x} films by means of intergrain and intragrain correlated defects. *Phys. Rev. B* **60**, 7623–7630 (10 Sept. 1999).

117. Mezzetti, E., Gerbaldo, R., Ghigo, G., Gozzelino, L. & Gherardi, L. Confinement of fluxons by surface columnar defects in $\text{Bi}_{1.8}\text{Pb}_{0.33}\text{Sr}_{1.87}\text{Ca}_2\text{Cu}_3\text{O}_y$ tapes. *Phys. Rev. B* **59**, 3890–3895 (5 Feb. 1999).
118. Maiorov, B. *et al.* Competition and cooperation of pinning by extrinsic point-like defects and intrinsic strong columnar defects in BaFe_2As_2 thin films. *Phys. Rev. B* **86**, 094513 (9 Sept. 2012).
119. Bernas, H. *et al.* Ion beam irradiation studies of high temperature superconductors. *Nuclear Instruments and Methods in Physics Research Section B: Beam Interactions with Materials and Atoms* **46**, 269–275. ISSN: 0168-583X (1990).
120. Bang, Y., Choi, H.-Y. & Won, H. Impurity effects on the $\pm s$ -wave state of the iron-based superconductors. *Phys. Rev. B* **79**, 054529 (5 Feb. 2009).
121. Dolgov, O. V. & Golubov, A. A. Strong electron-phonon interaction in multiband superconductors. *Phys. Rev. B* **77**, 214526 (21 June 2008).
122. Golubov, A. A. & Mazin, I. I. Effect of magnetic and nonmagnetic impurities on highly anisotropic superconductivity. *Phys. Rev. B* **55**, 15146–15152 (22 June 1997).
123. Mishra, V. *et al.* Lifting of nodes by disorder in extended- s -state superconductors: Application to ferropnictides. *Phys. Rev. B* **79**, 094512 (9 Mar. 2009).
124. Mizukami, Y. *et al.* Disorder-induced topological change of the superconducting gap structure in iron pnictides. *Nature communications* **5**, 5657 (2014).
125. Schilling, M. B. *et al.* Tracing the s_{\pm} symmetry in iron pnictides by controlled disorder. *Phys. Rev. B* **93**, 174515 (17 May 2016).
126. Ghigo, G. *et al.* Disorder-Driven Transition from s_{\pm} to s_{++} Superconducting Order Parameter in Proton Irradiated $\text{Ba}(\text{Fe}_{1-x}\text{Rh}_x)_2\text{As}_2$ Single Crystals. *Phys. Rev. Lett.* **121**, 107001 (10 Sept. 2018).
127. Gittus, J. *Irradiation effects in crystalline solids* (1978).
128. Knoll, G. F. *Radiation detection and measurement* (John Wiley & Sons, 2010).
129. Torsello, D. *et al.* Monte Carlo analysis of the oxygen knock-on effects induced by synchrotron x-ray radiation in the $\text{Bi}_2\text{Sr}_2\text{CaCu}_2\text{O}_{8+\delta}$ superconductor. *Phys. Rev. Materials* **2**, 014801 (1 Jan. 2018).
130. Ziegler, J. F., Biersack, J. P. & D, Z. M. *SRIM-2008, Stopping power and range of ions in matter* (2008).

131. Laviano, F. *et al.* Evidence of vortex curvature and anisotropic pinning in superconducting films by quantitative magneto-optics. *Phys. Rev. B* **68**, 014507 (1 July 2003).
132. Masee, F. *et al.* Imaging atomic-scale effects of high-energy ion irradiation on superconductivity and vortex pinning in Fe(Se,Te). *Science Advances* **1**, e1500033 (4 2015).
133. Prozorov, R. *et al.* Effect of Electron Irradiation on Superconductivity in Single Crystals of Ba(Fe_{1-x}Ru_x)₂As₂ ($x = 0.24$). *Phys. Rev. X* **4**, 041032 (4 Nov. 2014).
134. Smylie, M. P. *et al.* Effect of proton irradiation on superconductivity in optimally doped BaFe₂(As_{1-x}P_x)₂ single crystals. *Phys. Rev. B* **93**, 115119 (11 Mar. 2016).
135. Stefanini, A. M., Fortuna, G., Lunardi, S. & Ricci, R. A. The laboratori nazionali di legnaro. *Nuclear Physics News* **5**, 9–22 (1995).
136. Van de Graaff, R. J., Compton, K. T. & Van Atta, L. C. The Electrostatic Production of High Voltage for Nuclear Investigations. *Phys. Rev.* **43**, 149–157 (3 Feb. 1933).
137. Yntema, J. Heavy ion stripping in tandem accelerator terminals. *Nuclear Instruments and Methods* **122**, 45–52. ISSN: 0029-554X (1974).
138. Geller, R. *Electron cyclotron resonance ion sources and ECR plasmas* (Routledge, 2018).
139. Ben-Zvi, I., Paul, P. & Lombardi, A. Design of a Superconducting RFQ resonator. *Part. Accel.* **35**, 177–192 (1991).
140. Lombardi, A. *et al.* The new positive ion injector PLAVE at LNL in *Proceedings of the 1997 Particle Accelerator Conference (Cat. No.97CH36167)* **1** (May 1997), 1129–1131 vol.1.
141. Ben-Zvi, I. & Brennan, J. The quarter wave resonator as a superconducting linac element. *Nuclear Instruments and Methods in Physics Research* **212**, 73–79. ISSN: 0167-5087 (1983).
142. Ziegler, J. F., Ziegler, M. D. & Biersack, J. P. SRIM—The stopping and range of ions in matter (2010). *Nuclear Instruments and Methods in Physics Research Section B: Beam Interactions with Materials and Atoms* **268**, 1818–1823 (2010).
143. Sato, T. *et al.* Particle and Heavy Ion Transport code System, PHITS, version 2.52. *Journal of Nuclear Science and Technology* **50**, 913–923 (2013).

144. Feldman, L. C., Mayer, J. W. & Picraux, S. T. *Materials analysis by ion channeling: submicron crystallography* (Academic Press, 2012).
145. Kinchin, G. H. & Pease, R. S. The Displacement of Atoms in Solids by Radiation. *Reports on Progress in Physics* **18**, 1–51 (Jan. 1955).
146. Was, G. S. *Fundamentals of radiation materials science: metals and alloys* (Springer, 2016).
147. Anderson, P. Theory of dirty superconductors. *Journal of Physics and Chemistry of Solids* **11**, 26–30. ISSN: 0022-3697 (1959).
148. Abrikosov, A. & Gor'kov, L. Zh. É ksp. Teor. Fiz. 39, 1781 1960 Sov. Phys. *JETP* **12**, 1243 (1961).
149. Strehlow, C. P. *et al.* Comparative study of the effects of electron irradiation and natural disorder in single crystals of $\text{SrFe}_2(\text{As}_{1-x}\text{P}_x)_2$ superconductor ($x = 0.35$). *Phys. Rev. B* **90**, 020508 (2 July 2014).
150. Dolgov, O. V., Mazin, I. I., Parker, D. & Golubov, A. A. Interband superconductivity: Contrasts between Bardeen-Cooper-Schrieffer and Eliashberg theories. *Phys. Rev. B* **79**, 060502 (6 Feb. 2009).
151. Migdal, A. Interaction between electrons and lattice vibrations in a normal metal. *Sov. Phys. JETP* **7**, 996–1001 (1958).
152. Allen, P. B. & Mitrović, B. in (eds Ehrenreich, H., Seitz, F. & Turnbull, D.) 1–92 (Academic Press, 1983).
153. Eliashberg, G. Interactions between electrons and lattice vibrations in a superconductor. *Sov. Phys. JETP* **11**, 696–702 (1960).
154. Pietronero, L., Strässler, S. & Grimaldi, C. Nonadiabatic superconductivity. I. Vertex corrections for the electron-phonon interactions. *Phys. Rev. B* **52**, 10516–10529 (14 Oct. 1995).
155. Grimaldi, C., Pietronero, L. & Strässler, S. Nonadiabatic superconductivity. II. Generalized Eliashberg equations beyond Migdal's theorem. *Phys. Rev. B* **52**, 10530–10546 (14 Oct. 1995).
156. Inosov, D. *et al.* Normal-state spin dynamics and temperature-dependent spin-resonance energy in optimally doped $\text{BaFe}_{1.85}\text{Co}_{0.15}\text{As}_2$. *Nature Physics* **6**, 178 (2010).

157. Ortenzi, L., Cappelluti, E., Benfatto, L. & Pietronero, L. Fermi-Surface Shrinking and Interband Coupling in Iron-Based Pnictides. *Phys. Rev. Lett.* **103**, 046404 (4 July 2009).
158. Yi, M. *et al.* Electronic structure of the BaFe₂As₂ family of iron-pnictide superconductors. *Phys. Rev. B* **80**, 024515 (2 July 2009).
159. Shim, J. H., Haule, K. & Kotliar, G. Density-functional calculations of the electronic structures and magnetism of the pnictide superconductors BaFeAs₂ and BaFeSb₂. *Phys. Rev. B* **79**, 060501 (6 Feb. 2009).
160. Bennemann, K.-H. & Ketterson, J. B. *Superconductivity: Volume 1: Conventional and Unconventional Superconductors Volume 2: Novel Superconductors* (Springer Science Business Media, 2008).
161. Pavarini, E., Koch, E. & Schollwöck, U. *Emergent Phenomena in Correlated Matter: Autumn School Organized by the Forschungszentrum Jülich and the German Research School for Simulation Sciences at Forschungszentrum Jülich 23-27 September 2013; Lecture Notes of the Autumn School Correlated Electrons 2013* (Forschungszentrum Jülich, 2013).
162. Evtushinsky, D. V. *et al.* Momentum dependence of the superconducting gap in Ba_{1-x}K_xFe₂As₂. *Phys. Rev. B* **79**, 054517 (5 Feb. 2009).
163. Shimojima, T. *et al.* Orbital-Independent Superconducting Gaps in Iron Pnictides. *Science* **332**, 564–567. ISSN: 0036-8075 (2011).
164. Ummarino, G. A. Multiband $s \pm$ Eliashberg theory and temperature-dependent spin-resonance energy in iron pnictide superconductors. *Phys. Rev. B* **83**, 092508 (9 Mar. 2011).
165. Ummarino, G. A., Daghero, D., Tortello, M. & Gonnelli, R. S. Predictions of Multiband $s \pm$ Strong-Coupling Eliashberg Theory Compared to Experimental Data in Iron Pnictides. *Journal of Superconductivity and Novel Magnetism* **24**, 247–253. ISSN: 1557-1947 (Jan. 2011).
166. Ummarino, G. A., Tortello, M., Daghero, D. & Gonnelli, R. S. Three-band $s \pm$ Eliashberg theory and the superconducting gaps of iron pnictides. *Phys. Rev. B* **80**, 172503 (17 Nov. 2009).

167. Bose, S. K., Dolgov, O. V., Kortus, J., Jepsen, O. & Andersen, O. K. Pressure dependence of electron-phonon coupling and superconductivity in hcp Fe: A linear response study. *Phys. Rev. B* **67**, 214518 (21 June 2003).
168. Carbotte, J. P. Properties of boson-exchange superconductors. *Rev. Mod. Phys.* **62**, 1027–1157 (4 Oct. 1990).
169. Golubov, A. A., Brinkman, A., Dolgov, O. V., Kortus, J. & Jepsen, O. Multiband model for penetration depth in MgB₂. *Phys. Rev. B* **66**, 054524 (5 Aug. 2002).
170. Dolgov, O. V., Golubov, A. A. & Parker, D. Microwave response of superconducting pnictides: extended s_± scenario. *New Journal of Physics* **11**, 075012 (July 2009).
171. Tortello, M. *et al.* Multigap Superconductivity and Strong Electron-Boson Coupling in Fe-Based Superconductors: A Point-Contact Andreev-Reflection Study of Ba(Fe_{1-x}Co_x)₂As₂ Single Crystals. *Phys. Rev. Lett.* **105**, 237002 (23 Dec. 2010).
172. Efremov, D. V., Golubov, A. A. & Dolgov, O. V. Manifestations of impurity-induced s_± ⇒ s₊₊ transition: multiband model for dynamical response functions. *New Journal of Physics* **15**, 013002 (Jan. 2013).
173. Here $N_j^A(i\omega_m) = \Delta_j(i\omega_m) / \sqrt{\omega_m^2 + \Delta_j^2(i\omega_m)}$ and $N_j^Z(i\omega_m) = \omega_m / \sqrt{\omega_m^2 + \Delta_j^2(i\omega_m)}$
174. Ormeno, R. J. *et al.* Electrodynamic response of Sr₂RuO₄. *Phys. Rev. B* **74**, 092504 (9 Sept. 2006).
175. Hashimoto, K. *et al.* Microwave Surface-Impedance Measurements of the Magnetic Penetration Depth in Single Crystal Ba_{1-x}K_xFe₂As₂ Superconductors: Evidence for a Disorder-Dependent Superfluid Density. *Phys. Rev. Lett.* **102**, 207001 (20 May 2009).
176. Takahashi, H., Imai, Y., Komiya, S., Tsukada, I. & Maeda, A. Anomalous temperature dependence of the superfluid density caused by a dirty-to-clean crossover in superconducting FeSe_{0.4}Te_{0.6} single crystals. *Phys. Rev. B* **84**, 132503 (13 Oct. 2011).
177. Torsello, D. *et al.* Electrodynamic response of Ba (Fe 1- x Rh x) 2 As 2 across the s_± to s₊₊ order parameter transition. *The European Physical Journal Special Topics* **228**, 719–723 (2019).
178. Inosov, D. S. *et al.* Crossover from weak to strong pairing in unconventional superconductors. *Phys. Rev. B* **83**, 214520 (21 June 2011).

179. Mansart, B. *et al.* Opening of the superconducting gap in the hole pockets of $\text{Ba}(\text{Fe}_{1-x}\text{Co}_x)_2\text{As}_2$ as seen via angle-resolved photoelectron spectroscopy. *Phys. Rev. B* **85**, 144508 (14 Apr. 2012).
180. Gordon, R. T. *et al.* Unconventional London Penetration Depth in Single-Crystal $\text{Ba}(\text{Fe}_{0.93}\text{Co}_{0.07})_2\text{As}_2$ Superconductors. *Phys. Rev. Lett.* **102**, 127004 (12 Mar. 2009).
181. Gordon, R. T. *et al.* Doping evolution of the absolute value of the London penetration depth and superfluid density in single crystals of $\text{Ba}(\text{Fe}_{1-x}\text{Co}_x)_2\text{As}_2$. *Phys. Rev. B* **82**, 054507 (5 Aug. 2010).
182. Vorontsov, A. B., Vavilov, M. G. & Chubukov, A. V. Superfluid density and penetration depth in the iron pnictides. *Phys. Rev. B* **79**, 140507 (14 Apr. 2009).
183. Kasahara, S. *et al.* Evolution from non-Fermi- to Fermi-liquid transport via isovalent doping in $\text{BaFe}_2(\text{As}_{1-x}\text{P}_x)_2$ superconductors. *Phys. Rev. B* **81**, 184519 (18 May 2010).
184. Hashimoto, K. *et al.* Line nodes in the energy gap of superconducting $\text{BaFe}_2(\text{As}_{1-x}\text{P}_x)_2$ single crystals as seen via penetration depth and thermal conductivity. *Phys. Rev. B* **81**, 220501 (22 June 2010).
185. Klein, O., Nicol, E. J., Holczer, K. & Grüner, G. Conductivity coherence factors in the conventional superconductors Nb and Pb. *Phys. Rev. B* **50**, 6307–6316 (9 Sept. 1994).
186. Valdés Aguilar, R. *et al.* Pair-breaking effects and coherence peak in the terahertz conductivity of superconducting $\text{BaFe}_{2-2x}\text{Co}_{2x}\text{As}_2$ thin films. *Phys. Rev. B* **82**, 180514 (18 Nov. 2010).
187. Deepwell, D. *et al.* Microwave conductivity and superfluid density in strongly overdoped $\text{Tl}_2\text{Ba}_2\text{CuO}_{6+\delta}$. *Phys. Rev. B* **88**, 214509 (21 Dec. 2013).
188. Yu, W. *et al.* ^{77}Se NMR Study of the Pairing Symmetry and the Spin Dynamics in $\text{K}_y\text{Fe}_{2-x}\text{Se}_2$. *Phys. Rev. Lett.* **106**, 197001 (19 May 2011).
189. Yashima, M. *et al.* Strong-Coupling Spin-Singlet Superconductivity with Multiple Full Gaps in Hole-Doped $\text{Ba}_{0.6}\text{K}_{0.4}\text{Fe}_2\text{As}_2$ Probed by ^{57}Fe -NMR. *Journal of the Physical Society of Japan* **78**, 103702–103702 (2009).
190. Fischer, T. *et al.* Highly anisotropic energy gap in superconducting $\text{Ba}(\text{Fe}_{0.9}\text{Co}_{0.1})_2\text{As}_2$ from optical conductivity measurements. *Phys. Rev. B* **82**, 224507 (22 Dec. 2010).

-
191. Bonn, D. A. *et al.* Comparison of the influence of Ni and Zn impurities on the electromagnetic properties of $\text{YBa}_2\text{Cu}_3\text{O}_{6.95}$. *Phys. Rev. B* **50**, 4051–4063 (6 Aug. 1994).
 192. Nakai, Y. *et al.* ^{31}P and ^{75}As NMR evidence for a residual density of states at zero energy in superconducting $\text{BaFe}_2(\text{As}_{0.67}\text{P}_{0.33})_2$. *Phys. Rev. B* **81**, 020503 (2 Jan. 2010).
 193. Yamashita, M. *et al.* Nodal gap structure of superconducting $\text{BaFe}_2(\text{As}_{1-x}\text{P}_x)_2$ from angle-resolved thermal conductivity in a magnetic field. *Phys. Rev. B* **84**, 060507 (6 Aug. 2011).
 194. Diao, Z. *et al.* Microscopic parameters from high-resolution specific heat measurements on superoptimally substituted $\text{BaFe}_2(\text{As}_{1-x}\text{P}_x)_2$ single crystals. *Phys. Rev. B* **93**, 014509 (1 Jan. 2016).
 195. Saito, T., Onari, S. & Kontani, H. Nodal gap structure in Fe-based superconductors due to the competition between orbital and spin fluctuations. *Phys. Rev. B* **88**, 045115 (4 July 2013).
 196. Zhang, Y. *et al.* Nodal superconducting-gap structure in ferropnictide superconductor $\text{BaFe}_2(\text{As}_{0.7}\text{P}_{0.3})_2$. *Nature Physics* **8**, 371 (2012).
 197. Meier, W. R. *et al.* Anisotropic thermodynamic and transport properties of single-crystalline $\text{CaKFe}_4\text{As}_4$. *Phys. Rev. B* **94**, 064501 (6 Aug. 2016).
 198. Khasanov, R. *et al.* Anisotropy induced vortex lattice rearrangement in $\text{CaKFe}_4\text{As}_4$. *Phys. Rev. B* **99**, 140507 (14 Apr. 2019).
 199. Park, A. *et al.* Quasiparticle scattering in 3 MeV proton irradiated $\text{BaFe}_2(\text{As}_{0.67}\text{P}_{0.33})_2$. *Phys. Rev. B* **98**, 054512 (5 Aug. 2018).
 200. Nakajima, Y. *et al.* Enhancement of critical current density in Co-doped BaFe_2As_2 with columnar defects introduced by heavy-ion irradiation. *Physical Review B* **80**, 012510 (July 2009).
 201. Shestakov, V. A., Korshunov, M. M., Togushova, Y. N., Efremov, D. V. & Dolgov, O. V. Details of the disorder-induced transition between s_{\pm} and s_{++} states in the two-band model for Fe-based superconductors. *Superconductor Science and Technology* **31**, 034001 (Jan. 2018).

-
202. Ni, N. *et al.* Effects of Co substitution on thermodynamic and transport properties and anisotropic H_{c2} in $\text{Ba}(\text{Fe}_{1-x}\text{Co}_x)_2\text{As}_2$ single crystals. *Phys. Rev. B* **78**, 214515 (21 Dec. 2008).
203. Ni, N. *et al.* Phase diagrams of $\text{Ba}(\text{Fe}_{1-x}\text{M}_x)_2\text{As}_2$ single crystals ($M = \text{Rh}$ and Pd). *Phys. Rev. B* **80**, 024511 (2 July 2009).
204. Moroni, M. *et al.* Effect of proton irradiation on the normal-state low-energy excitations of $\text{Ba}(\text{Fe}_{1-x}\text{Rh}_x)_2\text{As}_2$ superconductors. *Phys. Rev. B* **96**, 094523 (9 Sept. 2017).
205. Tanatar, M. A. *et al.* Systematics of the temperature-dependent interplane resistivity in $\text{Ba}(\text{Fe}_{1-x}\text{M}_x)_2\text{As}_2$ ($M = \text{Co}, \text{Rh}, \text{Ni},$ and Pd). *Phys. Rev. B* **84**, 014519 (1 July 2011).
206. Kim, H. *et al.* Universal doping evolution of the superconducting gap anisotropy in single crystals of electron-doped $\text{Ba}(\text{Fe}_{1-x}\text{Rh}_x)_2\text{As}_2$ from London penetration depth measurements. *J. Phys.: Condensed Matter* **30**, 225602 (2018).
207. Teknowijoyo, S. *et al.* Enhancement of superconducting transition temperature by pointlike disorder and anisotropic energy gap in FeSe single crystals. *Phys. Rev. B* **94**, 064521 (6 Aug. 2016).
208. Gastiasoro, M. N., Bernardini, F. & Andersen, B. M. Unconventional Disorder Effects in Correlated Superconductors. *Phys. Rev. Lett.* **117**, 257002 (25 Dec. 2016).
209. Barannik, A. *et al.* Millimeter-wave surface impedance of optimally-doped $\text{Ba}(\text{Fe}_{1-x}\text{Co}_x)_2\text{As}_2$ single crystals. *Phys. Rev. B* **87**, 014506 (1 Jan. 2013).
210. Sylva, G. *et al.* Effects of high-energy proton irradiation on the superconducting properties of $\text{Fe}(\text{Se},\text{Te})$ thin films. *Superconductor Science and Technology* **31**, 054001 (Mar. 2018).
211. Palenzona, A. *et al.* A new approach for improving global critical current density in $\text{Fe}(\text{Se}_{0.5}\text{Te}_{0.5})$ polycrystalline materials. *Superconductor Science and Technology* **25**, 115018 (Oct. 2012).
212. Langford, J. I., Louër, D., Sonneveld, E. J. & Visser, J. W. Applications of Total Pattern Fitting to a Study of Crystallite Size and Strain in Zinc Oxide Powder. *Powder Diffraction* **1**, 211–221 (1986).
213. Johnson, R. & Orlov, A. N. *Physics of radiation effects in crystals* (Elsevier, 2012).

214. Pisent, A. & Comunian, M. *Complete simulation of the heavy ion linac PLAVE in Proceedings of the 1997 Particle Accelerator Conference (Cat. No.97CH36167) 1* (May 1997), 1132–1134 vol.1.
215. Mishev, V., Nakajima, M., Eisaki, H. & Eisterer, M. Effects of introducing isotropic artificial defects on the superconducting properties of differently doped Ba-122 based single crystals. *Scientific reports* **6**, 27783 (2016).

This Ph.D. thesis has been typeset by means of the \TeX -system facilities. The typesetting engine was $\text{Lua}\mathcal{E}\mathcal{T}\mathcal{X}$. The document class was `toptesi`, by Claudio Beccari, with option `tipotesi=scudo`. This class is available in every up-to-date and complete \TeX -system installation.